Color imaging and characterization of aerosol particles with digital holography

by

Ramesh Giri

M.Sc., Tribhuvan University, Kathmandu, Nepal, 2015

AN ABSTRACT OF A DISSERTATION

submitted in partial fulfillment of the
requirements for the degree

DOCTOR OF PHILOSOPHY

Department of Physics
College of Arts and Sciences

KANSAS STATE UNIVERSITY
Manhattan, Kansas

2022

Abstract

Aerosols are everywhere in the atmosphere. Therefore, it is critical to investigate their morphology *in situ* to understand how aerosols influence the environment and human health. In addition, the characterization of aerosols requires a fundamental understanding of properties such as shape, size, and color. One of the promising methods for characterizing aerosol particles is light scattering. Digital holography, also based on particle light scattering phenomena, works best for studying particle morphology *in situ*, which often addresses the inverse problem. This work describes an experimental approach to imaging freely flowing aerosol particles using multiple wave-length digital holography (MWDH). In contrast to conventional methods in DH, this work uses three different wavelength lasers (Red, Green, and Blue) combine to produce an almost white beam. In addition, the method involves a Michelson interferometer to produce holograms. When the backscattered light from the particles coherently mixes with the reference beam, interference patterns (holograms) are created. Using a three-CMOS prism sensor, we record three separate backscattered holograms, one for each wavelength, simultaneously and resolve them without spectral cross-talk. Fresnel diffraction theory is used to reconstruct holograms, which renders a monochrome image for each wavelength. The individual images are combined using the additive color mixing method, with red, green, and blue as primary colors. For size and color balance calibration, various colored micro-spheres (white, red, green, and cyan) are aerosolized, and the holograms are recorded. In addition, various mineral powders of different colors are used to demonstrate the viability of the experiment and the effect of basic speckle noise reduction and white balance approaches. Finally, chromaticity analysis is performed on the color image to illustrate the ability of the MWDH approach to objectively characterize aerosol particles of various shapes, sizes, and colors. Although MWDH has been used in several scientific fields, our study is the first to apply it to objects of micrometer-size scale to study

freely flowing coarse-mode particles. This research is also the first to create an MWDH image analysis that allows quantitative characterization of colored particles. The analysis quantifies the color content in the image regardless of the apparent brightness of the color in the image.

Color imaging and characterization of aerosol particles with digital holography

by

Ramesh Giri

M.Sc., Tribhuvan University, Kathmandu, Nepal, 2015

A DISSERTATION

submitted in partial fulfillment of the
requirements for the degree

DOCTOR OF PHILOSOPHY

Department of Physics
College of Arts and Sciences

KANSAS STATE UNIVERSITY
Manhattan, Kansas

2022

Approved by:

Major Professor
Matthew James Berg, Ph.D.

Copyright

© Ramesh Giri 2022.

Abstract

Aerosols are everywhere in the atmosphere. Therefore, it is critical to investigate their morphology *in situ* to understand how aerosols influence the environment and human health. In addition, the characterization of aerosols requires a fundamental understanding of properties such as shape, size, and color. One of the promising methods for characterizing aerosol particles is light scattering. Digital holography, also based on particle light scattering phenomena, works best for studying particle morphology *in situ*, which often addresses the inverse problem. This work describes an experimental approach to imaging freely flowing aerosol particles using multiple wave-length digital holography (MWDH). In contrast to conventional methods in DH, this work uses three different wavelength lasers (Red, Green, and Blue) combine to produce an almost white beam. In addition, the method involves a Michelson interferometer to produce holograms. When the backscattered light from the particles coherently mixes with the reference beam, interference patterns (holograms) are created. Using a three-CMOS prism sensor, we record three separate backscattered holograms, one for each wavelength, simultaneously and resolve them without spectral cross-talk. Fresnel diffraction theory is used to reconstruct holograms, which renders a monochrome image for each wavelength. The individual images are combined using the additive color mixing method, with red, green, and blue as primary colors. For size and color balance calibration, various colored micro-spheres (white, red, green, and cyan) are aerosolized, and the holograms are recorded. In addition, various mineral powders of different colors are used to demonstrate the viability of the experiment and the effect of basic speckle noise reduction and white balance approaches. Finally, chromaticity analysis is performed on the color image to illustrate the ability of the MWDH approach to objectively characterize aerosol particles of various shapes, sizes, and colors. Although MWDH has been used in several scientific fields, our study is the first to apply it to objects of micrometer-size scale to study

freely flowing coarse-mode particles. This research is also the first to create an MWDH image analysis that allows quantitative characterization of colored particles. The analysis quantifies the color content in the image regardless of the apparent brightness of the color in the image.

Table of Contents

List of Figures xi

Acknowledgements xiii

Dedication xv

1 Introduction 1

1.1 Aerosol particles 1

1.2 Aerosol particle characterization 2

1.3 Holography 4

1.4 Digital Holography 6

1.5 Important components in digital holography 8

1.5.1 Laser 8

1.5.2 Coherence of laser 9

1.5.3 Optical components 11

1.5.4 Sensor 12

1.5.5 Color sensor 14

1.6 Multiple wavelength digital holography 17

2 Theory 19

2.1 Light scattering 19

2.2 Interference of light in holography 21

2.3 Reconstruction of a hologram 25

2.3.1 Optical Reconstruction 26

2.3.2 Numerical Reconstruction 27

3 Forward Scattering Multiple Wavelength Digital Holography 35

3.1 Introduction 35

3.2 Experimental arrangement 36

3.3 Result 41

3.4 Discussion 45

4 Backscatter Multiple Wavelength Digital Holography 46

4.1 Introduction 46

4.2 Optical arrangement 48

4.3 Image rendering 51

4.3.1 Speckle suppression 53

4.3.2 White balance 56

4.4 Chromaticity analysis 59

4.5 Particle discrimination 61

4.6 Volume imaging with discrimination 65

4.7 Discussion 67

5 The Color of Aerosols 69

5.1 Introduction 69

5.1.1 Optical arrangement 71

5.1.2 Trigger and electronics system 74

5.1.3 Sample collection and preparation 76

5.1.4 Aerosol generation 77

5.1.5 Speckle reduction 78

5.1.6 Chromaticity analysis 80

5.1.7 White balance 83

5.2 Results 85

Bibliography 91

A Image Reconstruction Algorithm : Mathematica 112

List of Figures

1.1 Gabor inline holography. 5

1.2 Optical arrangement for the in-line digital holography 7

1.3 Michelson interferometer 9

1.4 Metal–oxide–semiconductor (MOS) capacitor 12

1.5 Spectral Response Curve of Blackfly S BFS-U3-32S4C-BD 13

1.6 Bayer filter mosaic 15

1.7 Design of a prism-based multisensor camera. 16

1.8 Spectral response curves of a multisensor camera (JAI-AP3200T). 17

2.1 Young's double-slit experiment 22

2.2 Principle of holography 23

2.3 Geometry for the Fresnel approximation 29

2.4 Sketch of the image formation and reconstruction process 32

3.1 Optical setup for forwarding digital holography with multiple wavelengths . . 37

3.2 Sketch of the aerosol-generating system. 39

3.3 The circuit and timing diagram 40

3.4 A contrast hologram and reconstructed image of an aerosolized clear glass micro-sphere of size $40\mu m$ recorded in MWDH. 42

3.5 The resolution test of the experiment 43

3.6 Images obtained from aerosolized dust particles of various shapes and sizes using MWDH 44

4.1 Optical arrangement for backscatter multiple wavelength digital holography. 49

4.2 Image rendering process from a contrast hologram. 52
4.3 Examples of speckle and its reduction in backscatter MWDH. 54
4.4 Demonstration of the simple white balance (WB) method. 55
4.5 Synthesis of color particle-images via additive color mixing 58
4.6 Chromaticity analysis of backscatter MWDH images 60
4.7 Color resolution in backscatter MWDH images 62
4.8 Particle discrimination based on color with chromaticity analysis 63
4.9 Volumetric discrimination of particles by color with backscatter MWDH . . . 66

5.1 The optical arrangement of MWDH for free-flowing aerosol particles. 72
5.2 MWDH laboratory arrangement for free-flowing aerosol particles on an optical table. 73
5.3 The trigger system. 75
5.4 Electronic circuit diagram to rectify PMT signals. 76
5.5 Picture of prepared mineral samples. The bulk of the minerals are pulverized using mortar and pestle and cascaded through series of sieves of different opening sizes. 77
5.6 Sketch of an aerosol particle generation system. 78
5.7 Chromaticity analysis of the image of white spheres obtained from MWDH before and after white balance 81
5.8 Chromaticity analysis of aerosolized color micro-spheres and non-spherical malachite mineral dust image from MWDH 84
5.9 Chromaticity analysis of a variety of free-flowing mineral dust aerosol particles 87
5.10 The sensitivity to the inclusion analysis of the material and the differentiation of various minerals in chromaticity diagram 88

Acknowledgments

I would like to start by expressing my gratitude to Dr. Matthew J. Berg, my Ph.D. advisor, for his consistent support and wise professional advice during this journey. Dr. Berg has always been available to help me at any time. He has helped me in many ways with his brilliant thoughts and original ideas. Even when I was down, his positive attitude always made me feel better. I was ready to work in the lab with new confidence after talking to him about my problems and fixing them. He taught me many experimental methods and theoretical groundwork in digital holography and electromagnetism. When he teaches anything, his excellent teaching abilities and thorough understanding of electromagnetism make it clear and simple to understand. I would not be able to establish myself as an independent researcher and a good collaborator without him.

I would like to thank my committee members, Dr. Christopher Sorensen, Dr. Gary Wysin, and Dr. Scott Thompson for being part of my Ph.D. It is a great honor for me to defend my doctoral dissertation under your supervision. Also, I would like to thank Dr. Matthew E. Brueseke, from Kansas State University (KSU), Department of Geology for providing the mineral samples.

I'm grateful to all of my colleagues. I really appreciate Dr. Osku Kemppinen's advice during my early days at work. He has created a nice atmosphere in the office for me. He was more than willing to answer all my questions. I am also thankful to my colleagues Peter Anderson, Dr. Peyman Feizollah, and Claudia Morello. It was always a pleasure to speak with them about academic, research, or random topics.

I would like to express my gratitude to my entire family for supporting me during all the highs and lows of this great journey and for having faith in me. I am grateful to my parents, Ramchandra Giri and Maya Giri, as well as to my brothers, Sagar Giri and Pawan Giri. Thank you very much to my wife, Yashoda Subedi, for her everlasting love, support, and inspiration. I am also grateful to my relatives and friends who have always pushed me to

work hard during my Ph.D. studies. Not to mention how grateful I am for my son, Divyan Giri, for his love and smiles.

Dedication

To my teachers, family, and friends

Chapter 1

Introduction

1.1 Aerosol particles

Aerosol particles are tiny atmospheric particles that can be found in the form of liquid droplets or solid particles. Due to their minuscule size and light weight, they can fly freely in the air. The size of such particles ranges from 10^{-4} μm to tens of μm [1–4]. Size affects their settlement time, since heavier particles settle faster than lighter particles. For example, nanometer aerosols remain in the air indefinitely, whereas 100 μm sized aerosols settle in a few seconds [5]. Although different in size, both types of aerosol are responsible for environmental changes and affect human health [6]. Aerosols, particularly mineral dust, settle on the surface of the soil and impact its biological cycle [7, 8]. They can be beneficial or harmful depending on their chemical composition and amount of deposition [9, 10]. On the other hand, unsettled aerosols are primarily responsible for the formation of clouds, and one cause of climate change on Earth [11]. Aerosols are created from natural phenomena or human activity. Sea spray aerosols (SSA), mineral dusts (MD), biological aerosols (BA), smoke aerosols (SA) and volcanic aerosols (VA) are some examples of natural aerosols [12–16]. However, human-made aerosols include particulates of nitrate and sulfuric acid emitted mainly from industry and transport, agriculture and land exploitation, waste, biomass combustion emissions, etc. [17, 18]. The tiny particles are small enough that the naked eye cannot see them. Still, they

greatly impact everyday human life, directly affecting health or indirectly causing climate change.

1.2 Aerosol particle characterization

Coarse-mode aerosol (CMA) of sizes greater than 1 μm are classified as complex aerosol particles in terms of morphology [19, 20]. CMA is abundant in the atmosphere and has an influence on agriculture, human health, and the environment [21–24]. These particles have an impact on climate change by forming cloud condensation nuclei (CCN) and ice nuclei [25–27]. They also influence the Earth's hydrological cycle [28]. For example, MD from the Sahara desert is considered the largest contributor to global aerosol production and plays a direct role in the meteorological phenomena of the Earth that greatly contribute to climate change. Since MDs can travel thousands of miles from where they form, they can affect local and global radiation budgets and affect the cloud formation process [29, 30]. Many studies have shown that windblown MDs account for at least one-third of the total aerosol concentration in the atmosphere. A large number of MDs can change Earth's temperature and sometimes cause cyclones to form [31, 32]. Identifying CMA requires characterization on a microscopic scale to understand the impact of aerosol particles on the environment. The morphology (shape, size, and orientation) and material composition must be known to characterize aerosol particles. However, information on the composition, concentration, and physical properties of CMA particles is inadequate. This information gap limits our ability to better understand the impact of CMA on radiative forcing and changes in Earth's climate [33–35]. A single aerosol particle characterization method can benefit environmental studies and many other scientific studies. Aerosol characterization is widely used in forensics, indoor and outdoor air pollution measurements, pollen particle detection and measurement, microbiological contamination, microplastic and microfiber detection in air, etc. [36–39].

Thanks to improvements in light microscopy, microsensors, and spectroscopy, many aspects of CMA particles can now be investigated in the laboratory. In recent years, many scientific devices have been discovered based on the principles of microscopy and spectroscopy.

These instruments are widely used to determine the composition of micrometer-sized particles and to monitor their shape and size. In particular, compound microscopes, transmission electron microscopes (TEM), scanning electron microscopes (SEM), ultraviolet, infrared, and laser microscopes are some examples of equipment used to determine the morphology of particles [40–42]. These tools are used for different purposes, each with its functional limitations. For example, an SEM can image at a micrometer resolution, while a TEM can look at a nanoscale resolution. Some other equipment is devoted to measuring the particle size distribution in a volume. Some of these names include Aerodynamic Particle Sizer (APS), Aerodynamic Aerosol Classifier (AAC), and Aerosol Particle Mass Analyzer (APM) [43–45]. Microscopy alone is insufficient if the purpose is to determine the material composition of the particle along with its morphology. For this purpose, the entire system should include a microscope in combination with a spectroscope. The concept of spectroscopy has motivated scientists to develop a variety of instruments. Different types of spectroscopy are available, including Raman spectroscopy (RS), Energy Dispersion X-Ray Spectroscopy (EDX), Fourier transform infrared spectroscopy (FTIR), mass spectroscopy (MS), nuclear magnetic resonance (NMR) spectroscopy, total reflection X-ray fluorescence (TXRF), electron probe microanalysis (EPMA) [46–49], and so on. Spectrometers are usually used in conjunction with microscopes to study particle morphology and material composition at the same time. All available instruments are very advanced and reliable for the characterization of aerosol particles, but unfortunately, they cannot be used outside the laboratory environment. They are bulky and also require unique configurations to work. Due to complex electrical wiring, cooling, vacuuming systems, etc., this machine is limited to laboratory use only. In addition, to use these instruments for particle characterization, a particle sample or gas containing aerosol particles must be taken from the environment in which they reside. The sample must be taken to a laboratory for analysis. Proper measurement of this sample requires proper handling and transportation, which in turn must not produce any distortion to the properties that one would like to assess. Many airborne aerosol particles are fragile, and the state of the sample, when obtained, can be affected by various physical factors. Cross-contamination can occur due to poor management or other circumstances [50, 51]. The actual morphology of the

aerosol particles is critical for identifying the aerosol, as particles of different shapes and sizes scatter light differently. The scattering of light from the spherical particle differs from the scattering of light from the non-spherical particle. Thus, it is essential to characterize them in their natural state or *in situ* to obtain their underlying morphology and components. In an approach to these limitations, technology must be developed to measure aerosols in their natural state without touching them. However, there has not yet been sufficient development of a measurement device capable of identifying aerosol particles in their original form. The light scattering method is one of the prospective methods for characterizing aerosol particles [52–55]. However, the inverse problem is a fundamental issue with the traditional light scattering method. Without any additional assumptions, the light-scattering measurement can not *uniquely* links the particle properties such as shape and size [56]. Digital holography is a potential approach based on a particle light scattering phenomenon that, in most cases, solves the inverse problem. It can be used to assess the properties of aerosol particles in real-time and in their original state. Digital holography has several advantages over conventional microscopes. One of the most important applications of digital holography is 3D image reconstruction. In contrast to the microscope, digital holograms store not only the intensity but also the wave-field phase, helping to reconstruct objects at an extensive depth of field.

1.3 Holography

Dennis Gabor, who won the Nobel Prize in physics in 1971 for the invention of holography in 1947, is considered the father of holography [57] and Leith, Upatnieks and P. Goss further developed the concept [58–60]. Gabor devised the term holography from the Greek words *holos* which means whole and *graphein* which means to write. In summary, holography means recording and reconstructing the entire information of a three-dimensional wave field. Gabor first introduced the holography technique intending to improve the spherical aberration of electron microscopy. As such, this idea was developed while solving an issue with the spherical aberration of the magnetic lens of the microscope. He tried to fix the problem

in two steps. In the first step, he recorded interference patterns between the electron beam scattered from an object and the reference beam propagated parallel on a photographic plate. In the second step, he again illuminated the recorded hologram with the same reference beam used before during the hologram recording. By these optical methods, the spherical aberrations of the electron microscope were corrected [61]. However, the image quality of the reconstructed wavefront was poor because of the lack of a coherent source with sufficient intensity. Due to the image's low resolution, holography was not widespread until the laser was discovered in 1960. Later, it was proven that the laser is an essential factor in optical holography. Along with the image of an object, it was also shown that a single hologram could store information on the optical field's phase, amplitude, and even polarization.

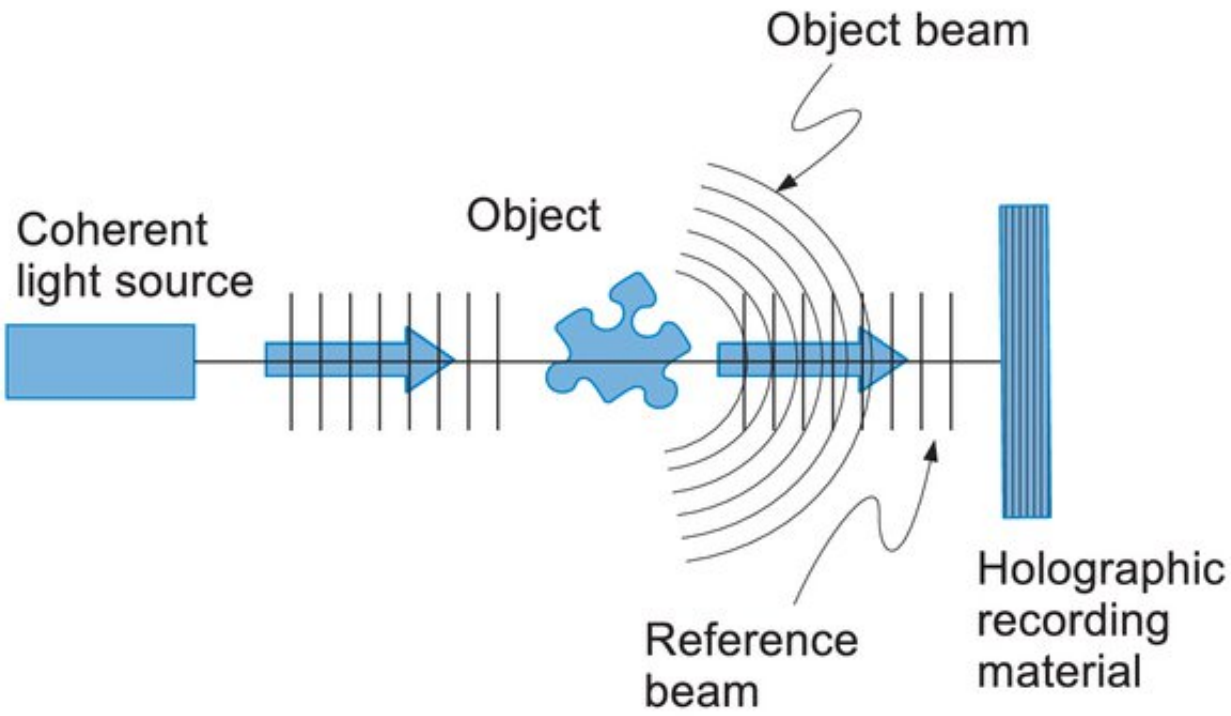


Figure 1.1: Gabor inline holography. An oblect is illuminated by a plane wave. The scattered light from the object interferes with the unscattered wave, produces interference and recorded on a photogrpahic plate.[62].

Gabor used the inline holographic method in his experiment, and the basic concept he introduced in his paper is shown in Figure 1.1. In his work, when a beam of light is illuminated on an object, a part of it is scattered. When the incident beam is considered much

wider than the object's size, most of the light has been passed unscattered. The unscattered light is used as a reference beam, interfered with the light scattered by the object, and formed interference patterns. These interference patterns are recorded on a transparent plate coated with the photosensitive material. The interference patterns recorded on the photographic plate are commonly called the hologram. The next step in the process of holography is to reconstruct the hologram recorded on the photosensitive plate. For the reconstruction, he again illuminated the hologram with the same light beam, but this time the object on the path of the light beam is removed.

The holography is based on two phenomena of light waves. The first phenomenon is when light is scattered during incident on an object. This phenomenon of light waves produced interference patterns while interfering with the reference beam, as discussed above. The reconstruction of the object beam that is encoded in the hologram can be performed based on the principle of diffraction of light. During reconstruction, when the hologram is illuminated by the light beam, the light wave is diffracted in three orders of diffraction, namely -1^{th} order, 0^{th} order, and $+1^{th}$ order. The -1^{th} order is proportional to the complex conjugate of the object beam, thus associated with the real image. The real image can be seen if a screen is placed at a distance equal to the object's distance from the photographic plate. The 0^{th} order is the sum of the squares of the modulus of the object and the reference beam, generally called a DC term. The $+1^{th}$ order is associated with the virtual image lying in the position where the object is placed during the hologram recording. In inline holography, all orders of diffraction fall on top of each other, which turns the blurred background onto the real image [63].

1.4 Digital Holography

In Conventional method of holography, a photographic plate is used to record holograms. A photographic plate is optically sensitive, thus when exposed to visible light, it exhibits chemical changes. Despite the low efficiency of photon reactions on the photographic plate, the photographic plate helps scientists to record and archive information for future use [64].

However, using a photographic plate in holography is time-consuming and tiresome. Furthermore, one can use a photographic plate only once, which is not cost-effective. In 1969, Willard S. Boyle and George E. Smith invented the charge-coupled device (CCD), the first viable digital picture technology [65, 66]. CCD technology takes advantage of Albert Einstein's prediction of the photoelectric effect, for which they are awarded the Nobel Prize in 2009. Light strikes a metallic surface and emits electrons, also known as photoelectrons, which are converted into an electrical signal in this effect. After the discovery of CCD, the recording media of holography changed from the classic photographic plate to digital recording media. High-resolution images from digital holography (DH) have been possible in recent years because of the progress of high-performance computers and large-pixel-density CCDs or complementary metal oxide semiconductors (CMOS) [67]. Because of the availability of larger arrays and smaller sensor pixel sizes, fast and efficient computing systems, and larger storage capability, digital holography is more feasible and efficient to use in various scientific disciplines such as medicine, biology, mineralogy, and manufacturing companies, among others. Digital holography works on the same principles as traditional analog holography, except for the recording medium and reconstruction process. In DH, the interference

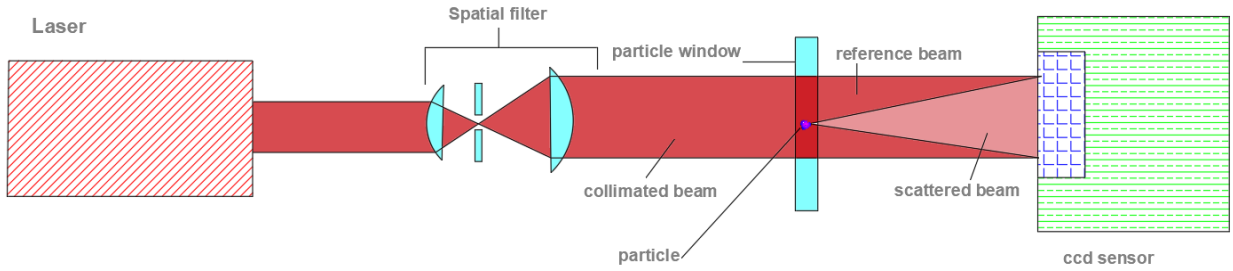


Figure 1.2: Optical arrangement for inline digital holography. A laser beam is cleaned, expand, and collimated by a spatial filter. The collimated beam illuminates the particle, a part of it is scattered by the particle and the rest of it is passed unscattered. The unscattered beam acts as a reference beam that intereferes with the scattered beam produce a hologram. An image sensor records the hologram.

between the object and the reference waves is captured on optoelectronic sensors such as CCDs and CMOS, similar to analog holography. The sensor records the interference as an image. Then the image (digital hologram) is reconstructed numerically. In many aspects,

DH is comparable to conventional microscopy. For example, reconstruction of an image in DH is analogous to focusing the image at various focal points in microscopy. In microscopy, different parts of a thicker object can be brought into focus by altering the height of the microscope objective at different times. In contrast, in DH, different parts of the object can be brought into focus by numerical calculation of the interference wave field using only a single pre-recorded hologram. During computational reconstruction, the focus distance d can be numerically changed to obtain various focus sites of the object, which is described in more detail in Chapter 2.

1.5 Important components in digital holography

1.5.1 Laser

As previously stated, optical holography in the visible spectrum is achievable by discovering a powerful and coherent light source, i.e., the laser. Furthermore, due to the coherent nature of laser light, a high-quality interference contrast can be formed, which improves image clarity and resolution in holography [68]. Gas and solid-state lasers are the two most common types of laser used in DH, and they are further classified as continuous-wave (CW) lasers and pulsed lasers. The helium-neon laser, for example, is a CW laser with a wavelength of 633 nm widely used in various applications because of its extended coherence length and longer life. A few other CW lasers used in optical holography are the argon-ion laser (458 nm, 488 nm, 514 nm), the helium-cadmium laser (325 nm, 442 nm), and the krypton-ion laser (647 nm), among others. The ruby laser, with a wavelength of 694 nm, is a commonly used pulsed laser in optical holography; however, it requires water cooling. In contrast, Nd-YAG lasers with a wavelength of 1064 nm that, when doubled in frequency, produce green light with a wavelength of 527 nm are the most compatible lasers, requiring only air cooling and being able to operate in both CW and pulsed modes, making them the laser of choice to replace ruby lasers these days.

1.5.2 Coherence of laser

The interference between the object wave and the reference wave makes holography possible. The quality of the hologram depends upon the coherent properties of the laser. In simple words, coherence refers to the ability of light waves to interfere. The contrast in the interference patterns stay consistent even if the paths of the two interfering beams are somewhat varied if the laser has better coherence. Temporal and spatial coherence are two types of coherence in a laser.

Temporal coherence is the degree of correlation of a wave phase at an instant for a specific location. As in-line holography the object and reference waves propagate in the same direction, thus it is important to calculate temporal coherence in a systematic manner. One of the simplest method to compute the temporal coherence of a laser is a Michelson interferometer.

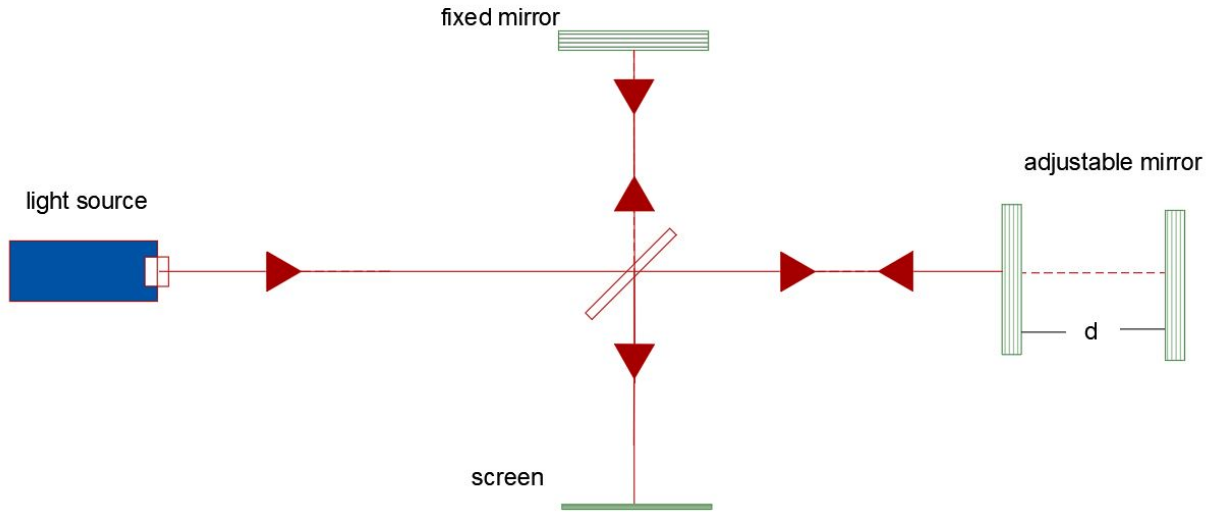


Figure 1.3: Michelson interferometer. A collimated light beam is divided perpendicularly by a 50 : 50 beam splitter. The beams are then retro-reflected from the mirrors and interferes on the screen. The adjustable mirror adjust the path difference between the two beam, which alters the contrast in interference patterns.

A beam splitter splits a light beam in a Michelson interferometer. A portion is reflected perpendicular to the propagation direction, and the rest is transmitted through the beam splitter. Two mirrors, one placed at a constant distance from the beam splitter and the other

set as a movable mirror, are used to retro-reflect the split beam, as illustrated in Figure 1.3. The reflected beams from the fixed mirror pass through the beam splitter and reach the detector, whereas the beam splitter reflects the beam from the movable mirror towards the detector. At the detector, the two beams interfere. If d is the difference between the distance of a movable mirror and the distance of a stationary mirror from the beam splitter and τ_c is the extra time it takes for the movable mirror beam to reach the detector compared to the beam of the fixed mirror.

Then,

$$\tau_c = \frac{2d}{c} \tag{1.1}$$

where c is the speed of light in a vacuum. If τ_c is defined as the coherence time at which the contrast of the interference patterns is reduced to e^{-1} of the contrast value when the beam interference is maximum. The coherence length can be defined as

$$l_c = c\tau_c \tag{1.2}$$

For the Gaussian laser beam, the coherence length can be written as

$$l_c = \sqrt{\frac{2\ln 2}{\pi n}} \frac{\lambda^2}{\Delta\lambda} \tag{1.3}$$

where n is the refractive index of the medium, λ is the central wavelength of the laser light, and $\Delta\lambda$ is the FWHM of the emission peak.

On the other hand, spatial coherence describes the phase correlation between different location of the same wavefront at an arbitrary time, which is also called interference of the division of the wavefront. Young's double-slit experiment, in which geometrically distinct parts of the same wavefront interact, helps explain the spatial coherence. The lasers used in holographic interferometry resonate in the TEM_{00} mode most of the time, which means that all points on the wavefront have the same phase and good spatial coherence [69–71].

1.5.3 Optical components

In digital holography, one most choose optical components carefully. The choice of optical elements determines the overall results of the experiment. First thing to understand is that optical elements are made of various materials design to work with certain wavelength ranges. In an optical experiment, mirrors are the most common optical element. For a better result in the experiment, the quality of the mirror is always fundamental. Mirrors with metallic coatings can be used for general purposes for spectral ranges from 450 nm to 12 μm and especially for space applications [72]. However, for a high-power laser-like Nd:YAG, broadband dielectric coating mirrors and diamond mirrors are recommended [73]. Mirrors with ultra-fast coatings should be used for lasers like Ti:Sapphire, which produces ultra-short pulses. Similarly, when choosing lenses, some factors to consider are lens shape, f-number, lens material, transmission percentage, wavefront distortion, antireflection coating, etc. [74]. Spherical lenses cause spherical aberration, and the proper lens shape can help to minimize this. For example, a planoconvex is one of the best lens for focusing the collimated beam on a point with a narrow waist. It reduces the aberration due to its asymmetric structure. To reduce the spherical aberration, the planoconvex lens should be faced in such a way that distance from the object to the curve surface becomes maximum [75, 76]. Also, the planoconvex lens can be used to compensate spherical aberration cause by positive lenses in the system. In addition, optical polarizers are another important optical components are commonly used to control the laser's polarization state. The extinction ratio, transmission, acceptance angle, and damage threshold are a few significant characteristics to consider when choosing polarizers. Many holographic interferometry methods require the modulation of laser beams. When phase alteration is required, phase-shifting optical components, such as half-wave plates that change the phase of incident light by $\pi/2$ and quarter-wave plates that shift the phase by $\pi/4$ are beneficial. The half-wave plate can rotate the linear polarization of incident light, whereas the quarter-wave plate can convert linearly polarized light to circularly polarized light.

1.5.4 Sensor

As previously stated, the primary difference between digital and analog holography is the replacement of the photographic plate with a digital recording device such as a charged coupled device (CCD) or a complementary metal oxide semiconductor (CMOS). Since the 1980s, CCD has been the most used imaging detector in practically all scientific and industrial applications because of their excellent performance capability. The metal oxide semiconductor (MOS) capacitor is the foundation of the CCD. Since silicon (Si) is sensitive to photons, while light shines on Si with photon energy greater than the band gap of silicon (i.e., 1.1 eV), electrons are generated;

$$E_{bandgap} > \frac{hc}{\lambda} \tag{1.4}$$

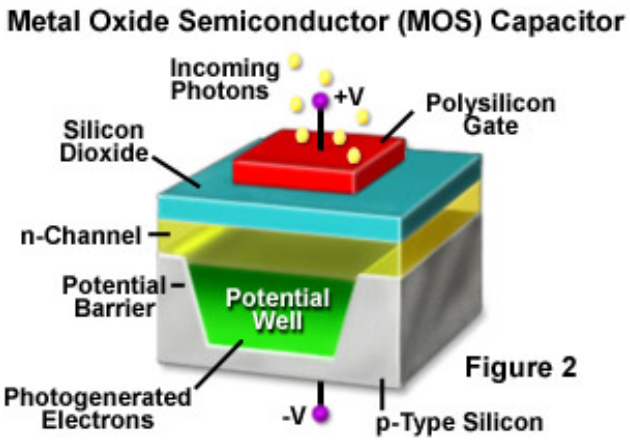


Figure 1.4: Metal–oxide–semiconductor (MOS) capacitor. An MOS capacitor consists of a semiconductor substrate (SiO_2) sandwiches in between a metal electrode and a semiconductor (Si).

Where h is the Planck constant and c is the speed of light in a vacuum. Silicon can detect practically all visible wavelengths and can also goes up to the near-infrared wavelength since its cutoff wavelength is nearly 1 μm. The detector plane of the CCD consists of a two-dimensional array of MOS capacitors, each capacitor representing a pixel. The photoelectrons are collected from each pixel by adding voltage to the capacitors. The total amount of electrons that may be stored per pixel before it becomes saturated is called the

CCD's well capacity. CCD arrays are classified into three types according to how the charge is transferred from capacitors to storage media: three-phase, interline, and frame transfer CCD arrays [77, 78]. For the specific applications of CCD, such as in digital holography, one must be careful when choosing the different types of CCD arrays. Before choosing CCD arrays, there are a few specifications to consider. To begin with, it is critical to understand the spectral range of interest where the CCD is more sensitive because the CCD responds differently to different wavelengths of light [79]. Figure 1.5 shows the spectral response curve or quantum efficiency of the Blackfly S BFS-U3-32S4C-BD camera. The quantum efficiency (QE) for blue (at 470 nm) is 50.41 %, the QE for green (at 525 nm) is 60.62 %, and the QE for red (at 630 nm) is 46.86 % [80]. Similarly, it is best to select a CCD with a low dark current if the CCD is used under low light conditions. Another important consideration is quantum efficiency (QE). QE refers to the rate at which photons are converted into electrons. The sensor with the highest QE for the wavelength of interest should be chosen. Other significant factors before selecting a CCD include the pixel size, total number of pixels (active area), dynamic range, etc.

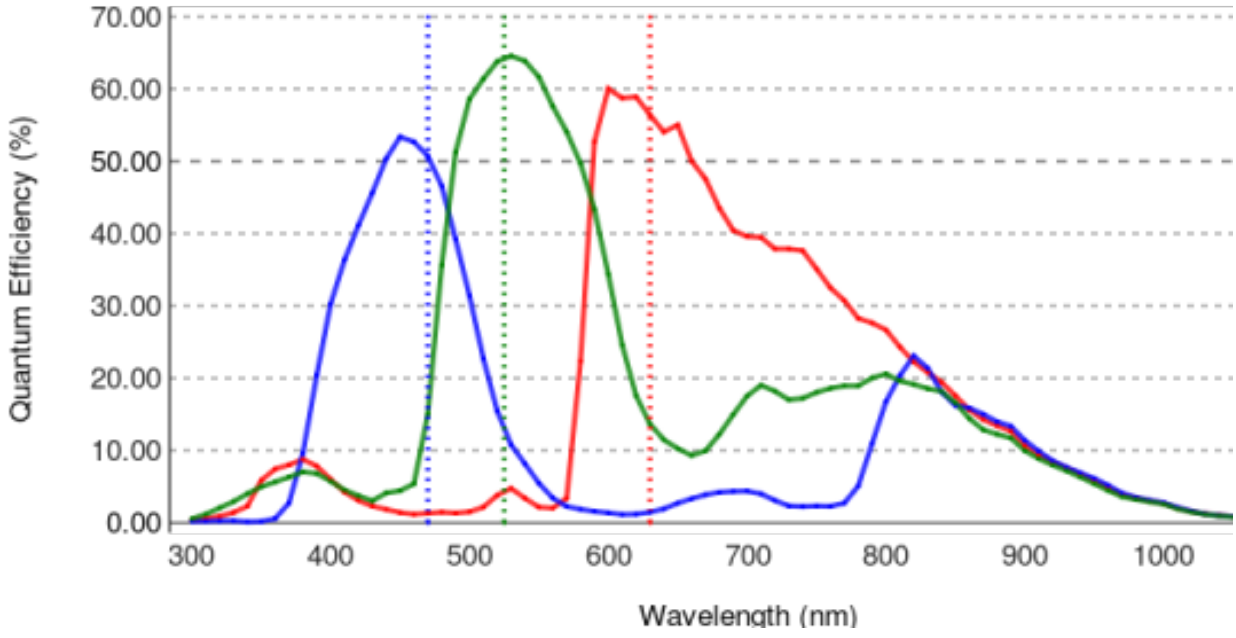


Figure 1.5: Spectral Response Curve of Blackfly S BFS-U3-32S4C-BD [80].

Similarly, CMOS sensors are now widely used image sensors in the field of imaging.

The main distinction between CCD and CMOS is their manufacturing process and how to charge transformations are made and converted to a voltage. A control circuit in a CCD transfers the charge collected on a pixel to its neighboring pixel, and the last pixel in the array transfers the charge to the charge amplifier for voltage conversion. However, in a CMOS sensor array, each pixel has a photodiode and a transistor that amplifies the pixel's signal. Matrix switches allow the signal from each pixel to be retrieved directly from the pixel at a much faster rate than a CCD. Furthermore, unlike CCD, CMOS has very compact circuitry that consumes less power and has less heat dissipation [67, 81, 82]. Aside from these differences, both CCDs and CMOS can be beneficial in digital holography, depending on their application to the system.

1.5.5 Color sensor

A color image sensor is required if one is interested in recording a multiwavelength spectral response for the scene, such as in multiple wave-length digital holography (MWDH) [83]. A color sensor is similar to a monochrome CCD/CMOS sensor, but each array of the sensor records different color components (wavelengths), namely red (R), green (G), and blue (B). The color sensor then generates a color image using the spectral responses of the object, that is, taking RGB as the primary color component. Some color imaging systems use three distinct sensors that independently record R, G, and B spectral responses. In contrast, others employ a single monochrome sensor with a layered color filter. Using such a sensor with a color filter has several advantages, including the need to have only one sensor and the ability to record all color information simultaneously.

Bayer's mosaic filter is perhaps the most widely used color filter in practice [84, 85]. The number of green channel arrays in this filter is twice that of red and blue channels to mimic the human eye, which is more sensitive to green light. Three light channels are recorded when light strikes the Bayer filter on the sensor, each with different intensities for red, green, and blue light. Because each sensor's pixels can only record one of three colors, the irregular patterns in Bayer's filter for each color cause gaps between the pixels for a

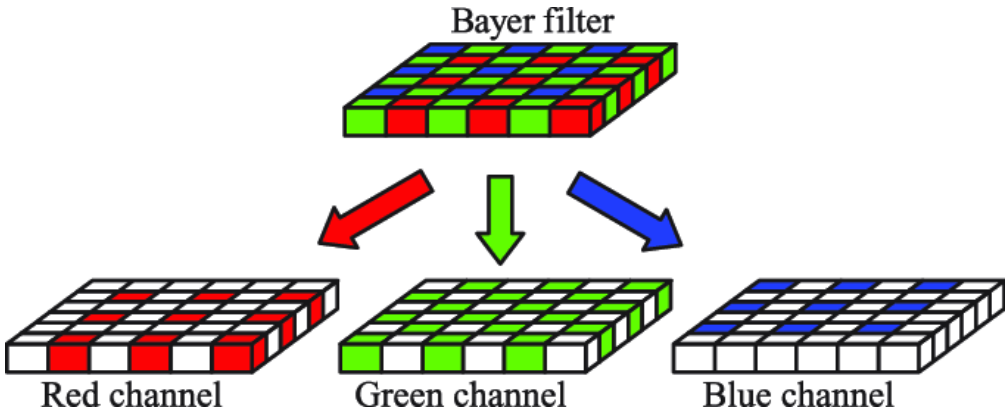


Figure 1.6: Bayer filter mosaic. A square grid of RGB color filters placed over a single-chip digital image sensor used to transmit particular color to the sensor and blocks others. To mimic human eyes, the filter pattern has almost half of green, and one quarter red and one quarter blue filters.

particular wavelength. The raw data (output) will not be able to fill in the information of missing pixels on its own. Only by demosaicing the raw data with algorithms, full-color information can be achieved. The algorithm helps convert the Bayer raw color channels to the full RGB color format by interpolating the gap using the information available from the surrounding pixels [86]. The use of the Bayer filter has a few disadvantages, including false color representation caused by interpolation and color crosstalk, both of which degrade the quality of the image. In addition, Bayer's filter uses dyes or pigments that do not completely absorb the cross-color light and cause the color-cross talk between the spectra of each color channel. As shown in Figure 1.5, the blue spectrum ranges from blue to green to red, and the green spectral ranges from blue to red, while the red spectral ranges from red to green [87].

However, a prism-based color sensor consists of multiple prism blocks which are equipped with hard dichroic coatings to assist in the separation of white light into different colors . Fig. 1.7 shows the separation of white light inside the prism block. The short wavelength, i.e., blue region of the spectrum, is separated first, followed by red while the green passes through the prism block. Light is separated before entering the sensor. In addition, the prism-based sensor has three distinct RGB color sensors. When light passes through the prism system, the first block splits the blue light and reflects it to the first monochrome

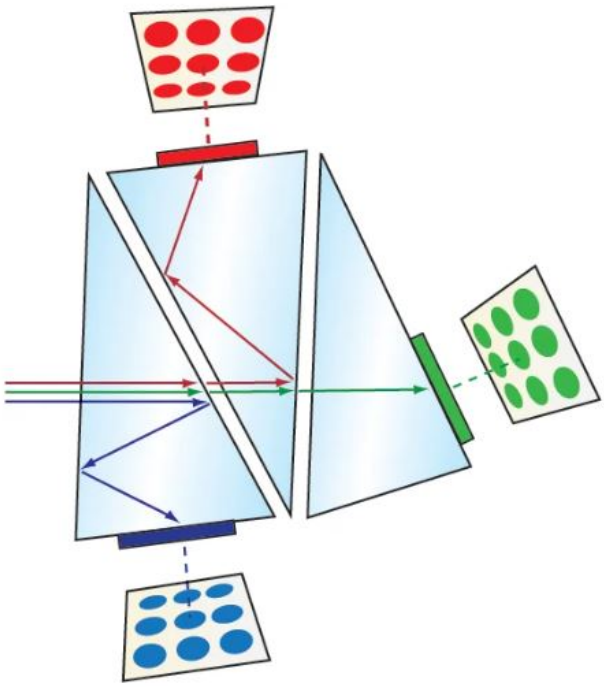


Figure 1.7: Design of a prism-based multisensor camera. The sensor consists of multiple prisms glued with hard dichroic coatings. The first prisms separates the blue light first, then followed by red, and the green is passes through. Each color is recorded by an individual sensor.

sensor. Similarly, the second prism block splits the red light and reflects it to the second monochrome sensor, and finally the green light is transmitted through all of them and reaches the third monochrome sensor, as shown in Figure 1.7.

The multisensor camera offers a few advantages over the single-sensor Bayer filter camera in that each color spectrum is captured by the individual sensors, using all of their pixels, and there is no interpolation required for final image rendition. In addition, because the sensor is superior in color distinction, the color in the image is drastically improved, resulting in an more true color representation with increased image contrast. Another benefit is the increased spatial resolution, since debayering in the Bayer filter requires $2\times$ 2 Bayer patterns, reducing the spatial resolution by 4 for red and blue channels. On the contrary, by a factor of 2 for the green channel, the spatial resolution of the multisensor camera is approximately four times greater than that of the Bayer filter sensor. Furthermore, as previously stated, the sensor with Bayer's filter suffers from color cross-talk. However, in the prism-based

multisensor camera, the dichotic interference coatings on the prism provide better filtering than the dyes used in the Bayer filter, resulting in substantially less color cross-talk, as shown in Figure 1.8. Furthermore, independent sensors adjust the strength and exposure for each channel, providing the best signal-to-noise ratio possible.

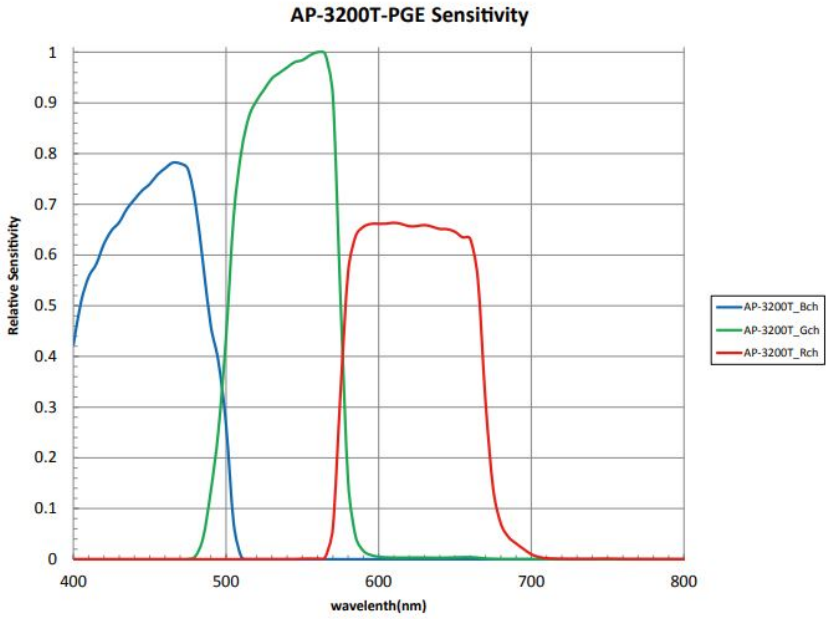


Figure 1.8: Spectral response curves of a multisensor camera (JAI-AP3200T).

1.6 Multiple wavelength digital holography

With the evolution of high-resolution RGB sensors, high-power lasers with longer coherence length, and sufficient computational capability for data processing, full-color 3D images with MWDH are now achievable. The MWDH is, in principle, comparable to monochrome digital holography. The only difference is that it requires three lasers operating at different wavelengths, such as red, green, and blue (R, G, and B), which are used to record the complex amplitude of the object with an RGB color sensor. In the full-color MWDH, three holograms are collected for each primary color channel (RGB). From each hologram, an images is reconstructed. Subsequently, the three images from three holograms are merged to produce a color image of the particle.

The color reproduction of an color image is determined by the spectral characteristics of the laser sources, the spectral response of a color object to the incident light, and the color sensor's spectral sensitivity or quantum efficiency. For example, because an object's spectral response varies depending on the light source, the color of an object illuminated by three-wavelength lasers may differ from that of an object illuminated by a white-light source. However, three-color lasers may be sufficient to produce a color image that can be used to characterize aerosol particles. Thus, digital holography, along with a color measurement technique, is capable of acquiring the object's morphology and spectral information simultaneously.

An object's absorption, reflectance, and refractive index are often wavelength-dependent and can be measured from the multi-wavelength object wave information using MWDH. The MWDH technique is unique because it provides multi-focus color imaging and quantitative phase-contrast analysis. One can perform multi-wavelength phase unwrapping for 3D image shape, assessment of morphology and refractive index simultaneously, and 3D tomographic images of dispersion, to name a few applications. Color digital holography has numerous other practical applications in a variety of scientific domains as well. The study of biological sample structures, sizes, and color reflections illustrates how digital color holography can be used. Many life science investigations rely on multispectral imaging, such as skin cancers, deformities, non-contact skin melanoma selection, and so on. Multispectral imaging is also beneficial in the study of live species, in medicine (for example, in vivo detection of oral neoplasia) and in environmental studies (for example, pollen grains, minerals and dust in air and water quality assessments), among other applications. The MWDH can be applied to almost all the multispectral imaging phenomena mentioned above.

Chapter 2

Theory

Light scattering and interference are two fundamental light phenomena used in digital holography (DH). Before delving into the DH principle, it is necessary to understand these phenomena. This chapter provides an overview of light scattering, interference, scalar diffraction theory, and the Fresnel approximation. Then, hologram recording, image reconstruction, and the resolution of the reconstructed image will be demonstrated.

2.1 Light scattering

Light is an electromagnetic wave (EM wave) [88–90]. When charges are accelerated, both electric field $\mathbf{E}(\mathbf{r},t)$ and magnetic fields $\mathbf{B}(\mathbf{r},t)$ are produced simultaneously. These fields are coupled perpendicularly to each other, propagate in the direction normal to acceleration direction, and evolve in space $\mathbf{r}$ and time t. To understand the concept of digital holography, it is essential to study how electromagnetic waves interact with the medium through which they propagate. Digital holography is based on two fundamental light phenomena: scattering and interference, as they interact with materials. Light scattering is a natural phenomenon in which light is redistributed when it interacts with matter such as dust, gas, water, etc. Understanding light scattering is particularly important, as many natural phenomena occur because of the scattering of light.

The evolution of an electromagnetic wave in a vacuum can be explained by Maxwell's equations, in terms of $\mathbf{E}$(r,t) and $\mathbf{B}$(r,t) where μ_0 and ϵ_0 are the permeability and permittivity of the electromagnetic wave in free space as,

$$\nabla \times \mathbf{B} = \mu_0 \epsilon_0 \frac{\partial \mathbf{E}}{\partial t} \tag{2.1}$$

$$\nabla \times \mathbf{E} = -\frac{\partial \mathbf{B}}{\partial t} \tag{2.2}$$

$$\nabla \cdot \mathbf{B} = 0, \tag{2.3}$$

$$\nabla \cdot \mathbf{E} = 0 \tag{2.4}$$

Aerosol particles exhibit a very weak response to the magnetic field, so $\mathbf{B}$ can be ignored in this study. However, it can be calculated using the knowledge of $\mathbf{E}$ if necessary [91, 92]. If one solves the Maxwell equations, the plane wave becomes the simplest solution. In free space, the plane wave can be written as;

$$\mathbf{E}(\mathbf{r}, t) = \mathbf{E}_0 \, e^{(i\mathbf{k}\cdot\mathbf{r} - i\omega t)} \tag{2.5}$$

where $\mathbf{E}_0$ is a constant vector representing the different polarization directions of the wave, $\mathbf{k}$ ($= \frac{2\pi}{\lambda}\hat{\mathbf{n}}^{\text{ inc}}$) is the wave number and ω is the angular frequency of the wave of wavelength λ. In the case of a laser light source, the light can polarize in any arbitrary direction and be monochromatic. Due to the single frequency present in the laser light, the term exp(− iωt) can be omitted, as the Maxwell equation is reduced to the partial differential equation in only the space part, i.e., $\mathbf{r}$. Then Eq. 2.5 can be written as

$$\mathbf{E}(\mathbf{r}) = \mathbf{E}_0 \, e^{i(\mathbf{k}\cdot\mathbf{r})} \tag{2.6}$$

Assume that a region of space is supposed to be a scattering volume and will eventually contain particles later. However, first consider that there are no particles in that volume and that the electromagnetic wave (light) continuously occupies all available space, including

the scattering volume. Such a wave field is commonly called incident light. In this case, the source of light is considered to lie at infinity, so that the presence of particles in the scattering volume does not have any affect on the source. For the incident wave, Eq. 2.6 can be written in the simplest form as

$$\mathbf{E}^{\text{inc}}(\mathbf{r}) = \mathbf{E}_0^{\text{inc}}\, e^{i\mathrm{k}_0(\hat{\mathbf{n}}^{\text{ inc}}.\mathbf{r})} \tag{2.7}$$

where $\hat{\mathbf{n}}^{\text{ inc}}$ is the direction of propagation of the wave and k_0 $(= 2\pi/\lambda)$ is the wave number in vacuum. If a particle is present in the scattering volume, the incident light interacts with the particles and creates a new wave. In this case, some of the light might be absorbed, and the rest of it is scattered by the particle. The amount of scattered or absorbed light depends on the particle's shape, size, and material composition. A detector measures the total field which can be mathematically written as the sum of the incident and scattered field, but practically the two field can not be resolved.

$$\mathbf{E}^{\text{total}}(\mathbf{r}) = \mathbf{E}^{\text{inc}}(\mathbf{r}) + \mathbf{E}^{\text{sca}}(\mathbf{r}) \tag{2.8}$$

In other words, the scattered field can be obtained by subtracting the incident field from the total field measured after the light is scattered from the particles. i.e,

$$\mathbf{E}^{\text{sca}}(\mathbf{r}) = \mathbf{E}^{\text{total}}(\mathbf{r}) - \mathbf{E}^{\text{inc}}(\mathbf{r}) \tag{2.9}$$

2.2 Interference of light in holography

The principle of holography is not limited only to the visible spectrum; rather, it can be applied to other types of wave interference phenomena, such as microwaves, supersonic waves, and electron waves, among others [93–95]. One should be familiar with light-wave phenomena, such as light interference, to better understand holography. Light interference involves two coherent waves of equal, greater, or lower amplitudes. However, to observe interference,

the frequency of two waves should be equal, or in other words the frequency should be stable. For example, He-Ne is a stable frequency laser with a longer coherent length, normally measured in meters. Young is called upon to discover the occurrence of light interference

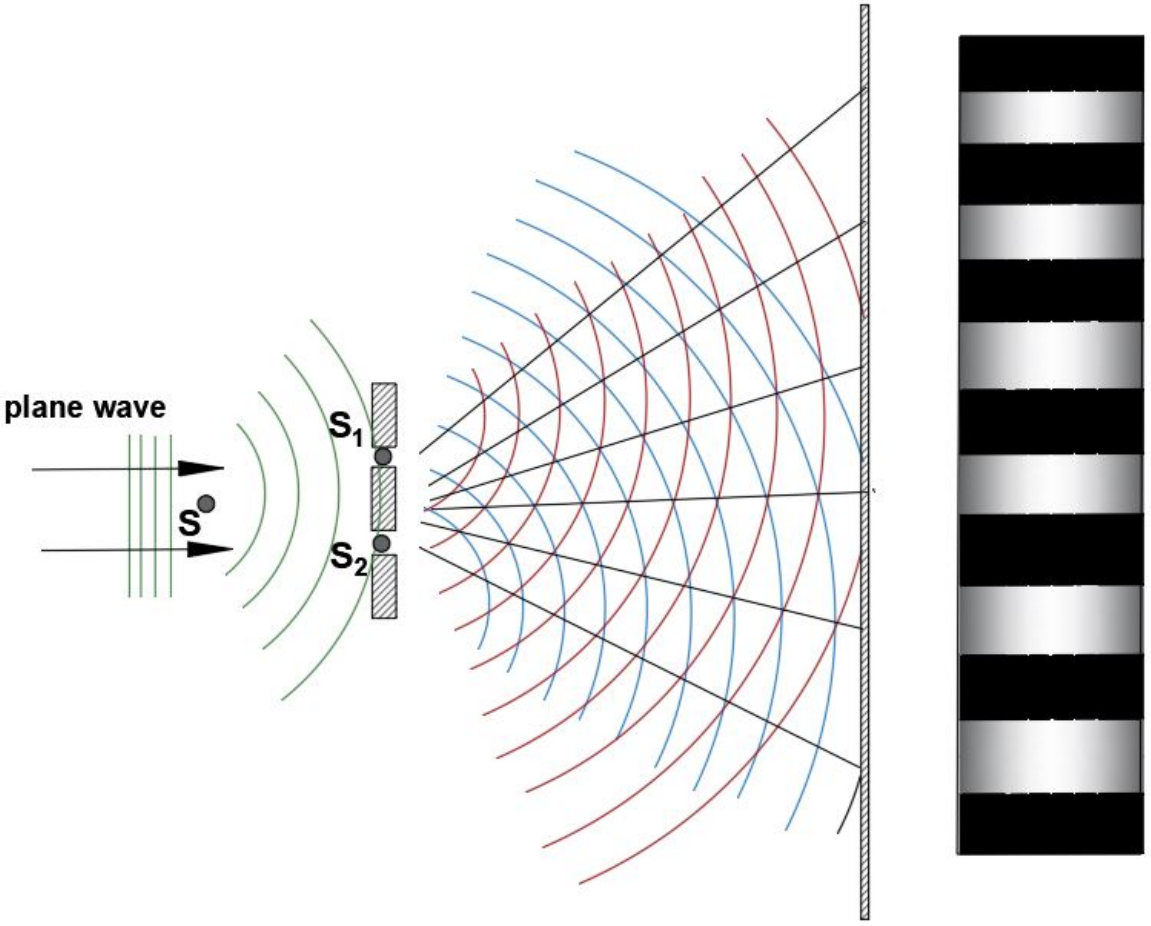


Figure 2.1: Young's double-slit experiment. The two points S_1, and S_2 of a same wavefront behave as new sources, illuminate light of same frequency. The spherical wavefronts generated by S_1, and S_2 interferes with each other and produce interference patterns on the screen.

from two sources. In his principle, a light source produces a spherical wavefront, and two small slits are placed at a distance such that they further divide the wavefront. Now, the slits represent two points on the same wavefront and behave as the new light sources S_1 and S_2 propagate the spherical wavefront with same frequency as shown in Fig. 2.1. The waves are then interfere with each other. The interference patterns are visible on the screen at a distance and consist of a series of bright and dark stripes. When the wave maxima coin-

cide, bright patterns are produced, and dark patterns are produced when the wave minima coincide. Similarly to Young's experiment, in holography, two waves, i.e., a wave scattered from the objects and the reference wave, interfere with each other and produce interference patterns. To develop a theoretical foundation for interference in digital holography, consider an in-line version of the DH set-up, as shown in Fig. 1.2. In this configuration, a coherent light source illuminates a particle. When the particles are illuminated, light is scattered, absorbed, and transmitted through them. If the illuminating beam is much broader than the particles, then most light passes unaffected. However, a particle scatters light and interferes with the light that passes unaffected. An interference pattern, also known as a hologram, is recorded by a detector (sensor). With this hologram, 3-D spatial information can be obtained on the wave amplitude and phase associated with the illuminated wave and the object. The amplitude and phase information in holography helps measure many physical properties of the particles, such as shape, size, numbers, color, scattering cross section, and extinction cross section.

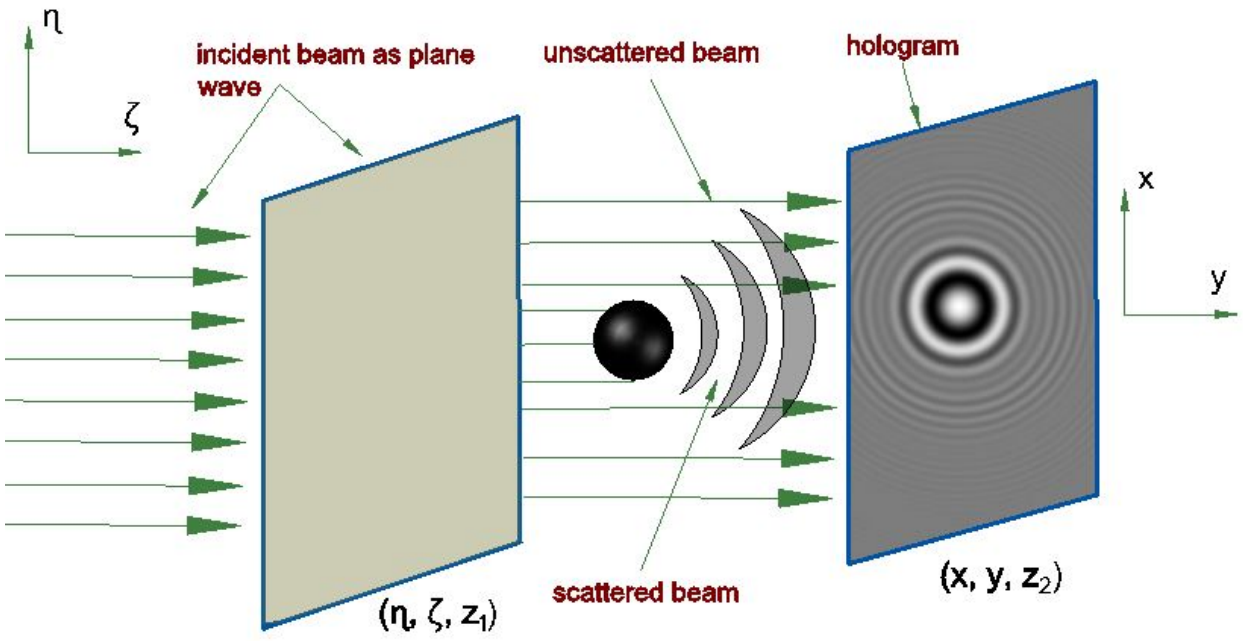


Figure 2.2: Principle of holography. A plane wavefront illuminates a particle, a part of the incident wave is scattered by the particles while the rest of it is passed unscattered. The scattered wave (object wave) and the unscattered wave (reference wave) interfere with each other and produce a interferent patterns, i.e hologram.

Consider two coordinate systems for the incident beam (η, ζ, z_1) and the detector (x, y, z_2) where z is the direction of propagation of the beam. For perfectly aligned inline holography, both the reference and detector planes are parallel to each other. Recall that the distance between the particle and the detector plane is $z = d$. The intensity of the hologram measured at the detector can be written as

$$\begin{aligned} \mathrm{H}(x,y) &= |\mathbf{E}^{\mathrm{O}}(\eta,\zeta,d) + \mathbf{E}^{\mathrm{R}}(\eta,\zeta,d)|^2 \\ &= |\mathbf{E}^{\mathrm{O}}(\eta,\zeta,d)|^2 + |\mathbf{E}^{\mathrm{R}}(\eta,\zeta,d)|^2 \\ &\quad |\mathbf{E}^{\mathrm{O}}(\eta,\zeta,d)|^* \cdot |\mathbf{E}^{\mathrm{R}}(\eta,\zeta,d)| \\ &\quad + |\mathbf{E}^{\mathrm{O}}(\eta,\zeta,d)| \cdot |\mathbf{E}^{\mathrm{R}}(\eta,\zeta,d)|^* \end{aligned} \tag{2.10}$$

The wave equation for the reference and object beams can be written as

$$|\mathbf{E}^{\mathrm{R}}(\eta,\zeta,d)| = \mathrm{E}^{\mathrm{R}}(\eta,\zeta,d)\exp\left[-k\phi_1(\eta,\zeta)\right] \tag{2.11}$$

$$|\mathbf{E}^{\mathrm{O}}(\eta,\zeta,d)| = \mathrm{E}^{\mathrm{O}}(\eta,\zeta,d)\exp\left[-k\phi_2(\eta,\zeta)\right] \tag{2.12}$$

Using Eq. 2.11 and 2.12 in Eq. 2.10 we get

$$\begin{aligned} \mathrm{H}(x,y) &= \mathrm{E}^{\mathrm{O}}(\eta,\zeta,d)^2 + \mathrm{E}^{\mathrm{R}}(\eta,\zeta,d)^2 + \\ &\quad \mathrm{E}^{\mathrm{O}}(\eta,\zeta,d)\mathrm{E}^{\mathrm{R}}(\eta,\zeta,d) \\ &\quad (\exp\left[-\mathrm{k}(\phi_1-\phi_2)\right] + \exp\left[-\mathrm{k}(\phi_2-\phi_1)\right]) \end{aligned} \tag{2.13}$$

For brevity, the Eq. 2.13 can be written as

$$\mathrm{I_H} = (\mathrm{E^R})^2 + (\mathrm{E^O})^2 + \mathrm{E^R E^O}\cos\mathrm{k}(\phi_1-\phi_2) \tag{2.14}$$

In Eq. 2.10, $\mathrm{H}(x,y)$ is the hologram in the detector plane, $\mathbf{E}^{\mathrm{R}}$ represents the unscattered reference wave and $\mathbf{E}^{\mathrm{O}}$ represents the particle-scattered object wave, and * stands for the

complex conjugate. In Eq. 2.14, the first term $(E^R)^2$ is the intensity of unscattered light, which is simply the constant background that can be removed after subtracting the background measurements. The second component $(E^O)^2$ is also a constant intensity term of the object wave, and it is negligibly smaller than the other two terms and can be ignored. The last two terms $(|\mathbf{E}^O|^*| \cdot \mathbf{E}^R| + |\mathbf{E}^R|^* \cdot |\mathbf{E}^O|)$ are the only ones that contribute to the formation of the hologram. As discussed above, the detector measures this cross-term, which is the interference pattern, and is stronger among the three. The term $\cos k(\phi_1 - \phi_2)$ is also called the interference term, which represents the phase difference between the two waves. If two waves are not coherent with each other, the average value of the interference term $\cos(\phi_1 - \phi_2)$ vanishes, and no interference occurs. In this case, the detector only records the amplitude of the two beams, that is, $(E^R)^2 + (E^O)^2$. However, if two waves are coherent with each other, the average value of $\Delta\phi (= \phi_1 - \phi_2)$ does not vanish; it fluctuates between -1 and +1. For maximum interference, it should be $\Delta\phi = n\pi$. When two waves are in phase, that is, $\cos\Delta\phi = 1$, the intensity is maximum, but if two waves are out of phase $\cos\Delta\phi = -1$, the intensity becomes minimum [63].

The total energy received by a photographic plate / sensor during the time of exposure t_e is

$$E_H(x, y) = \int_0^{t_e} H(x, y)\ dt \tag{2.15}$$

2.3 Reconstruction of a hologram

As discussed above, holography is a technique to record interference and produce images with the help of coherent light scattered from an object and a reference wave. When two waves interfere, the resulting pattern depends on the phase difference between the waves. The interference is constructive when the waves are in phase (at the same instant and same point along their path); it is destructive when they are out of phase. The recorded hologram, the object wave, can be reconstructed by illuminating the hologram with a wave called a reconstructed wave field. Once the reconstruction is complete, the observer sees a real and virtual image at the same distance from the recording medium. The reconstructed

image exhibits all the effects of perspective and depth of focus. The photographic plate reconstruction can be performed using an optical method, and a digital hologram can be reconstructed optically and numerically [96, 97].

2.3.1 Optical Reconstruction

The reference beam and the reconstruction beam are identical in phase and frequency. If two waves have the same phase or a constant phase difference, they can always interfere as long as they maintain the phase difference over time. This is true even if they propagate in different directions or at an angle. One of the most exciting aspects of holography is that it does not matter which direction the hologram is illuminated by the reconstruction beam when reconstructing. One can illuminate a beam on either side of a holographic plate as long as one knows which angle should illuminate the plate by the reconstruction beam for a better view. The holographic plate is illuminated by a reconstruction wave in the optical reconstruction process. In this case, the hologram behaves as a diffraction grating element. Once the wave is illuminated on the hologram, the beam undergoes a diffraction phenomenon. The collection of such diffracted waves from the hologram produces real and virtual images of the object. The virtual image is at the same distance as the real image of the photographic plate. Consider t_e as the exposure time and β as the sensitivity of the plate; then, the recorded hologram can be written as

$$\mathrm{H}(x, y) = \mathrm{t_e} \cdot \beta \cdot \mathrm{I}(x, y) \tag{2.16}$$

for brevity, if $\mathbf{E}^{\mathrm{R}}$ represents the complex amplitude of the reference wave and the reconstruction wave, and if $\mathbf{E}^{\mathrm{O}}$ represents the object wave, the total intensity recorded as a hologram is

$$\mathrm{I} = |\mathbf{E}_{\mathrm{R}}|^2 + |\mathbf{E}_{\mathrm{O}}|^2 + \mathbf{E}^*_{\mathrm{R}} \cdot \mathbf{E}_{\mathrm{O}} + \mathbf{E}^*_{O} \cdot \mathbf{E}_{R} \tag{2.17}$$

For optical reconstruction, the hologram is treated with the reconstructed wave $\mathbf{E}_{\mathrm{R}}$. The reconstructed complex wave amplitude is obtained as

$$\begin{aligned}\mathbf{E}_{\mathrm{recon}} &= \mathrm{t_e}.\beta.\mathbf{E}_{\mathrm{R}} \cdot \left(|\mathbf{E}_{\mathrm{R}}|^2 + |\mathbf{E}_{\mathrm{O}}|^2 + \mathbf{E}_{\mathrm{R}}^* \cdot \mathbf{E}_{\mathrm{O}} + \mathbf{E}_{\mathrm{O}}^* \cdot \mathbf{E}_{\mathrm{R}}\right) \\ &= \mathrm{t_e} \cdot \beta.\left(\mathbf{E}_{\mathrm{R}} \cdot |\mathbf{E}_{\mathrm{R}}|^2 + \mathbf{E}_{\mathrm{R}} \cdot |\mathbf{E}_{\mathrm{O}}|^2 + \mathbf{E}_{\mathrm{R}} \cdot \mathbf{E}_{\mathrm{R}}^* \cdot \mathbf{E}_{\mathrm{O}} + \mathbf{E}_{\mathrm{R}} \cdot \mathbf{E}_{\mathrm{O}}^* \cdot \mathbf{E}_{\mathrm{R}}\right) \\ &= \mathrm{t_e}\beta\mathbf{E}_{\mathrm{R}} \cdot |\mathbf{E}_{\mathrm{R}}|^2 + \mathrm{t_e}\beta\mathbf{E}_{\mathrm{R}} \cdot |\mathbf{E}_{\mathrm{O}}|^2 + \mathrm{t_e}\beta\mathbf{E}_{\mathrm{R}}^2 \cdot \mathbf{E}_{\mathrm{O}}^* + \mathrm{t_e}\beta|\mathbf{E}_{\mathrm{R}}|^2 \cdot \mathbf{E}_{\mathrm{O}}\end{aligned} \tag{2.18}$$

The coefficient $\mathrm{t_e}\beta$ in Eq. 2.18 is a constant term representing the brightness in the image, and the first term is a constant representing the zeroth term of diffraction order. This term includes only the non-interfering intensity values of the reference wave, multiplied by the average transmittance, which have no consequences on the image formation. Thus, the term does not play a significant role in interference phenomena, which can be suppressed. The second term is the out-of-focus image representation, commonly referred to as a halo. However, the third term represents the interference term between the reference wave and the complex conjugate of the object wave and produces the actual image of the object wave. This interference produces the conjugate image of the object wave. The last term commonly representing the virtual image of the object wave is also called an orthoscopic image. Two images in a combination are called twin images. These twin images appear in the foreground and in the background and lie at the same distance from the photographic plate after reconstruction. The holographic imaging produces the three-dimensional scene with varying depth of focus and parallax since the full object wave with the amplitude and phase is reconstructed [98–100].

2.3.2 Numerical Reconstruction

Holograms are a collection of fringe patterns produces due to interference of object wave and a reference wave, regardless of the recording medium. When reconstructed, it resembles a collection of diffraction gratings. In a typical holographic system, the waves that reach the hologram plane are usually spherical waves scattered from the object. Holography recording

is a process of intensity mapping of the interference waves to the recording medium. On the other hand, the reconstruction process involves the diffraction of the reconstructed wave from the hologram. To understand the numerical reconstruction of the hologram, it is necessary to understand the diffraction phenomenon of light through an obstacle.

Fresnel-Kirchhoff Diffraction

According to Huygens' principle, each point on a primary wavefront can be considered a new point source that continuously generates spherical wavelets [101, 102]. At any instant, a new wavefront can be formed by taking the envelope of these secondary wavelets. Fresnel utilized the concept of Huygen's principle to explain the idea of interference of the secondary wavelets to explain the phenomenon of diffraction [103]. To explain the Huygens-Fresnel theory, consider that a point source S radiates the spherical wavefronts and, at any instant, the wavefront strikes the aperture P. Each point in that wavefront intercepts the aperture and behaves as a new source. The spherical waves that originate from each source superpose to cause diffraction patterns in the observation plane.

Consider a point source S, which radiates spherical waves that illuminate an aperture. The aperture lies in the $(\xi, \eta, z = 0)$ plane in rectangular coordinates. If $\mathrm{E}(x, y)$ is the complex diffracted field amplitude at any point (x, y) on the observation plane, which is a plane parallel to the aperture plane (ξ, η). The Fresnel-Kirchoff diffraction formula for the diffracted field in the (x, y) plane is given by

$$\mathrm{E}(x, y) = \frac{1}{i\lambda} \iint_{-\infty}^{\infty} \mathrm{U}(\xi, \eta) \frac{e^{i\mathrm{k}r}}{r} \mathrm{F}(\theta)\ d\xi\ \mathrm{d}\eta \tag{2.19}$$

Here, $\mathrm{U}(\xi, \eta)$ represents the complex field amplitude in the plane (ξ, η), $\mathrm{F}(\theta) = \cos(\theta) = z/r$ is an obliquity factor, and θ is the angle between $\mathbf{r}$ and the unit vector $\hat{\mathrm{n}}$. If λ is the wavelength of the incident wave and k is the wave vector.

$$\mathrm{E}(x, y) = \frac{z}{i\lambda} \iint_{-\infty}^{\infty} \mathrm{U}(\xi, \eta) \frac{e^{ikr}}{r^2}\ \mathrm{d}\xi\ \mathrm{d}\eta \tag{2.20}$$

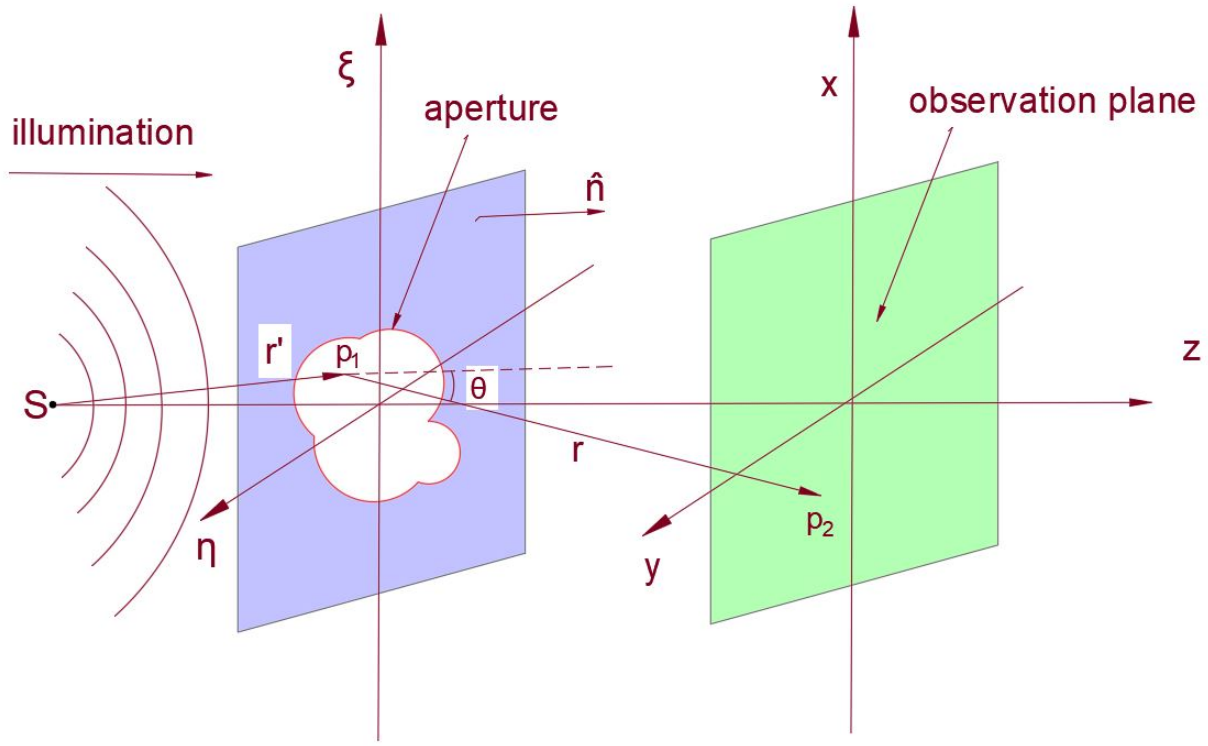


Figure 2.3: Geometry for the Fresnel approximation. A source of light S generates spherical wavefronts. The spherical wave are then diffracted by an aperture. The aperture lies in the $(\xi, \eta, z = 0)$ plane and the complex diffracted field is observed on a plane (x, y, z) in rectangular coordinates.

The oblique distance (r) from the point p_1 in the aperture plane to the point p_2 at the observation point, as shown in Figure 2.3 can be written as

$$r = \sqrt{(\xi - x)^2 + (\eta - y)^2 + z^2} \tag{2.21}$$

Taking into account the distance from the aperture plane to the image plane, that is, z is larger compared to the lateral distance of the points x, y, ξ and η, that is, $z \gg \sqrt{(x - \xi)^2 + (y - \eta)^2}$. The value of r in the denominator of 2.20 can be replaced by z. The exponential term contains k, which is in the sub-micrometer range and is multiple with r, measured in meters. A slight variation of r would lead to a significant phase error and cannot be replaced. Thus, the exponential term needs a precise approximation. The Fresnel approximation uses the binomial expansion of the square root into the series.

$$
\begin{aligned}
r &= \sqrt{(\xi - x)^2 + (\eta - y)^2 + z^2} \\
&= z\sqrt{1 + \left(\frac{\xi - x}{z}\right)^2 + \left(\frac{\eta - y}{z}\right)^2} \\
&\approx z\left[1 + \frac{1}{2}\left(\frac{\xi - x}{z}\right)^2 + \frac{1}{2}\left(\frac{\eta - y}{z}\right)^2\right]
\end{aligned}
\tag{2.22}
$$

Applying Eq. 2.22 to Eq. 2.20, we get

$$
\begin{aligned}
\mathrm{E}(x, y) &= \frac{1}{iz\lambda}\iint_{-\infty}^{\infty} \mathrm{U}(\xi, \eta) \exp\left(ik\left[1 + \frac{1}{2}\left(\frac{\xi - x}{z}\right)^2 + \frac{1}{2}\left(\frac{\eta - y}{z}\right)^2\right]\right)\, d\xi\, d\eta \\
&= \frac{e^{ikz}}{iz\lambda}\iint_{-\infty}^{\infty} \mathrm{U}(\xi, \eta) \exp\left[\frac{ik}{2z}\left[(\xi - x)^2 + (\eta - y)^2\right]\right]\, d\xi\, d\eta
\end{aligned}
\tag{2.23}
$$

Equation 2.23 is called the Fresnel transformation or the Fresnel-Kirchhoff diffraction integral.

Recording and Numerical Reconstruction of Digital hologram

To record the digital hologram using optoelectronic devices such as CCD and CMOS, a coherent laser is required [104, 105]. The source of light illuminates the particles on its path. The scattered light from the particles coherently interferes with a reference beam and produces interference patterns. Interference patterns encoded for amplitude and phase information are recorded in sensor arrays. From the holograms, one can directly access the complex wave field of the object. The complex field provides an additional degree of flexibility in optical metrology. Contactless, non-destructive optical measurements, and characterizations are possible in DH. It has some applications, including shape and deformation measurements, vibration analysis, object identification, refractometry, temperature measurement, etc. [106–108]. To understand the hologram recording, consider a spherical object illuminated by a linearly polarized collimated beam. The wave amplitude recorded in the sensor array when the particle is not present is called the reference wave, and the wave recorded after the

particle is present on the beam path, called the scattered wave, can be written as

$$\mathrm{E}^{\mathrm{ref}}(\mathbf{r}) = \mathrm{E}_0^{\mathrm{ref}}(\hat{\mathbf{r}})\frac{\mathrm{e}^{ik.\mathbf{r}}}{\mathbf{r}} \tag{2.24}$$

$$\mathrm{E}^{\mathrm{sca}}(\mathbf{r}) = \mathrm{E}_0^{\mathrm{sca}}(\hat{\mathbf{r}})\frac{\mathrm{e}^{ik.\mathbf{r}}}{\mathbf{r}} \tag{2.25}$$

Here, $\mathbf{r}$ is the position vector, and $\mathrm{E}_0^{\mathrm{ref}}(\hat{\mathbf{r}})$ and $\mathrm{E}_0^{\mathrm{sca}}(\hat{\mathbf{r}})$ are the amplitudes of reference and scattered waves respectively. The intensity of these waves is

$$\mathrm{I}^{\mathrm{ref}}(\mathbf{r}) = \frac{\mathrm{c}\epsilon_0}{r^2}|\mathrm{E}_0^{\mathrm{ref}}(\hat{\mathbf{r}})|^2 \tag{2.26}$$

$$\mathrm{I}^{\mathrm{sca}}(\mathbf{r}) = \frac{\mathrm{c}\epsilon_0}{r^2}|\mathrm{E}_0^{\mathrm{sca}}(\hat{\mathbf{r}})|^2 \tag{2.27}$$

Here, ϵ_0 is the permittivity of free space, and c is the speed of light in a vacuum. When the particle presents in the beam path, the sensor records the interference intensity of the reference beam and the scattered beam. The hologram intensity is written as:

$$\mathrm{I}^{\mathrm{holo}}(\mathbf{r}) = \frac{\mathrm{c}\epsilon_0}{r^2}|\mathrm{E}_0^{\mathrm{sca}}(\hat{\mathbf{r}}) + \mathrm{E}_0^{\mathrm{ref}}(\hat{\mathbf{r}})|^2 \tag{2.28}$$

Now the contrast hologram can be made by subtracting Eq. 2.26 from Eq. 2.28

$$\begin{aligned} \mathrm{I}^{\mathrm{con}}(\mathbf{r}) &= \frac{\mathrm{c}\epsilon_0}{r^2}\left[|\mathrm{E}_0^{\mathrm{sca}}(\hat{\mathbf{r}}) + \mathrm{E}_0^{\mathrm{ref}}(\hat{\mathbf{r}})|^2 - |\mathrm{E}_0^{\mathrm{ref}}(\hat{\mathbf{r}})|^2\right] \\ &= \frac{\mathrm{c}\epsilon_0}{r^2}\left[|\mathrm{E}_0^{\mathrm{sca}}(\hat{\mathbf{r}})|^2 + \mathrm{E}_0^{\mathrm{sca}}(\hat{\mathbf{r}})[\mathrm{E}_0^{\mathrm{ref}}(\hat{\mathbf{r}})]^* + \mathrm{E}_0^{\mathrm{ref}}(\hat{\mathbf{r}})[\mathrm{E}_0^{\mathrm{sca}}(\hat{\mathbf{r}})]^*\right] \end{aligned} \tag{2.29}$$

In Eq. 2.29, $*$ represents the complex conjugate. The first term is the intensity contribution of the scattered wave only is a constant and negligibly small in magnitude compared to the reference beam. Thus it can be neglected. The last two terms are the interference terms

between the reference, and scattered wave contributes to the formation of the hologram.

$$\mathrm{I}^{\mathrm{con}}(\mathbf{r}) = \frac{c\epsilon_0}{r^2}\left[\mathrm{E}_0^{\mathrm{sca}}(\hat{\mathbf{r}}) \cdot [\mathrm{E}_0^{\mathrm{ref}}(\hat{\mathbf{r}})]^* + \mathrm{E}_0^{\mathrm{ref}}(\hat{\mathbf{r}}) \cdot [\mathrm{E}_0^{\mathrm{sca}}(\hat{\mathbf{r}})]^*\right] \tag{2.30}$$

Now the challenge is to create images from contrast holograms. Recall that in the optical reconstruction of the holographic plate, the hologram is considered a transmission diffraction grating. The patterns of the grating on the plate have a fine-scale variation in the optical density. Furthermore, a reference beam illuminated the diffraction grating in the reconstruction process. The grating diffracts the light into plane waves in the forward direction. However, in digital holography, the holographic plate is replaced by a CCD and CMOS sensor. Each sensor pixels can now be considered a diffraction grating element. The image is then produced from $\mathrm{I}^{\mathrm{holo}}$ using Fresnel- Kirchhoff's diffraction formula [109]. The process is called image reconstruction.

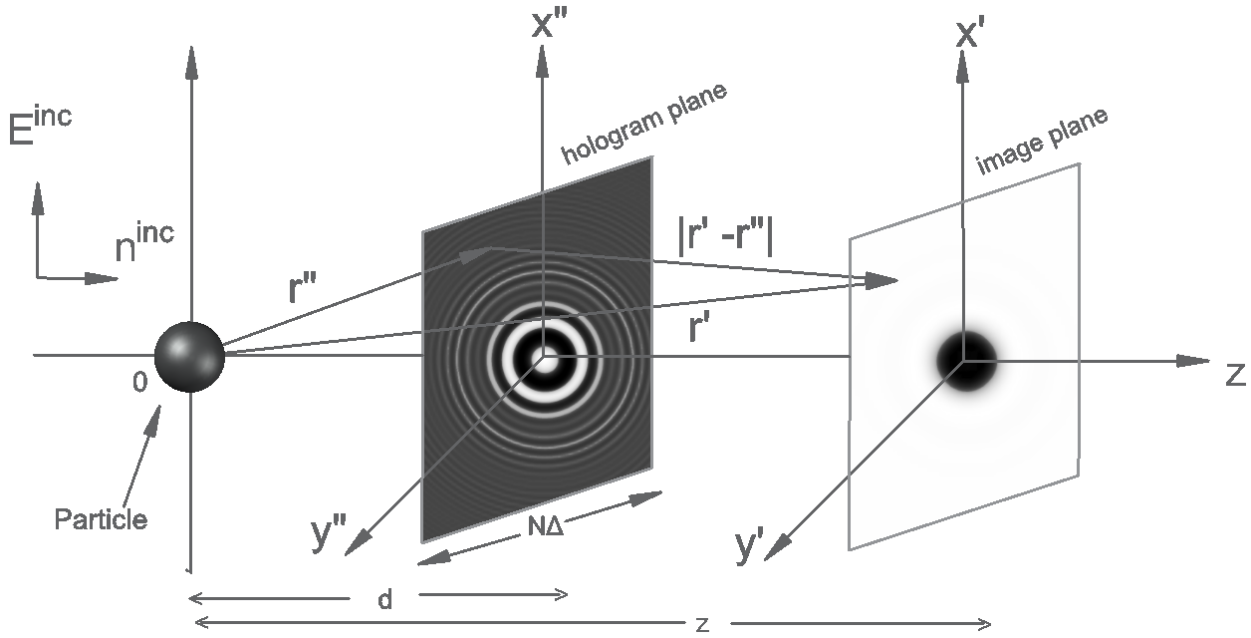


Figure 2.4: Sketch of the image formation and reconstruction process where the hologram is considered as a transmission diffraction grating that produces an image $|K|^2$ (see Eq. 2.31) in the image plane through the application of diffraction theory.

Here, consider a particle at O illuminated by a plane wavefront of the field $\mathrm{E}^{\mathrm{inc}}$, which propagates in the z-direction. A hologram is recorded on a plane (x'', y'') at a distance d

from O. The image is reconstructed on a plane (x', y') parallel to the plane of the hologram (x'', y'')

As explained above, if the particle lies at a distance much larger than the wavelength of light, that is, $z \gg \lambda$, then the Fresnel-Kirchoff equation can be written as follows.

$$\mathrm{K}(x', y') = \frac{e^{ikz}}{iz\lambda} \iint_{-\infty}^{\infty} \mathrm{I}^{\mathrm{con}}(x'', y'') \exp\left[\frac{i\pi}{d\lambda}\left[(x'' - x')^2 + y'' - y')^2\right]\right] \mathrm{d}x'' \, \mathrm{d}y'' \tag{2.31}$$

Here, d is the distance between the particles and the hologram plane. Consider substituting $x' = \nu\lambda d$ and $y' = \mu\lambda d$, then Eq. 2.31 becomes

$$\mathrm{K}(x', y') = \frac{e^{ikd}}{id\lambda} \iint_{-\infty}^{\infty} \mathrm{I}^{\mathrm{con}}(x'', y'') \exp\left[\frac{i\pi}{d\lambda}(x''^2 + y''^2)\right] \exp\left[-2i\pi(x''\frac{x'}{\lambda d} + y''\frac{x'}{\lambda d})\right] \, dx'' \, dy''$$

$$\mathrm{K}(\nu, \mu) = \frac{\exp\left[ikd\right]}{id\lambda} \exp\left[i\pi d\lambda(\nu^2 + \mu^2)\right] \iint_{-\infty}^{\infty} \mathrm{I}^{\mathrm{con}}(x'', y'') \exp\left[\frac{i\pi}{d\lambda}(x''^2 + y''^2)\right] \exp\left[-2i\pi(x''\nu + y''\mu)\right] \, \mathrm{d}x'' \, \mathrm{d}y'' \tag{2.32}$$

Here, the term $\exp\left[ikd\right]/id\lambda$ is independent of spatial frequency and is purely a constant intensity factor and can be simply excluded in further analysis. However, the term inside the integral is a phase factor and is the Fourier transform of the product of the hologram and the two-dimensional chirp function $\exp\left[\frac{i\pi}{d\lambda}(x''^2 + y''^2)\right]$.

Computationally, the integration in Eq. 2.32 requires much computational power. For rapid image processing, convolution can be used between two functions, say f and g, which can be expressed as

$$[\mathrm{f} \otimes \mathrm{g}](x, y) = \iint_{-\infty}^{\infty} \mathrm{f}(x', y') \ \mathrm{g}(x - x', y - y') \ \mathrm{d}x' \ \mathrm{d}y' \tag{2.33}$$

Here, the impulse response is denoted by h and is written as

$$\mathrm{h}(x'', y'') = exp\left[\frac{i\pi}{d\lambda}(x''^2 + y''^2)\right] \tag{2.34}$$

Applying the convolution theorem in 2.32, we get

$$\mathrm{K}(\nu, \mu) = \frac{\exp\left[ikd\right]}{id\lambda} exp\left[i\pi d\lambda(\nu^2 + \mu^2)\right] \mathcal{F}^{-1}[\mathcal{F}(I^{con}) \times \mathcal{F}(h(x'', y''))] \tag{2.35}$$

The absolute square of the wave amplitude, $|\mathrm{K}(\nu, \mu)|^2$, produces the image of the object.

Chapter 3

Forward Scattering Multiple Wavelength Digital Holography

3.1 Introduction

DH for the imaging of aerosol particles has many potential applications. Most importantly, it can be used for monitoring the aerosols in the air in real-time. Direct measurements of the properties of aerosols can reveal what type of aerosol is present in the air and its contribution to environmental changes and air pollution. [54, 110–112]. It also helps identify unknown aerosols and their possible origin, which can help mitigate potential health and environmental hazards. [113–116] . MWDH is not a new concept and has also been used in various fields of study. For example, the MWDH is used in such studies to calculate the volume displacement of various topographic surface features, phase imaging without two π ambiguities, and height measurements of linearly moving and rotating objects. [117–119] etc. However, this work presents the forward scattering multiple wavelength digital holography for imaging aerosolized micron-size particles. Three different colors (wavelength) lasers, i.e., blue, green, and red, are combined with reflective dichroic mirrors to produce nearly a white beam. The detail is explained in the following sections. The white beam is then used to illuminates the aerosolized micro-particles. The forward scattered lights from the aerosol

particle interfere with the lights passed unscattered and produce a color (RGB) hologram. A prism CMOS color sensor records the holograms. The digitally obtained color hologram is then computationally reconstructed for individual color channels, i.e., blue channel, green channel, and red channel, and add them to obtain the final image of the aerosol particle.

3.2 Experimental arrangement

The optical configuration of forward MWDH is shown in Figure 3.1. Three lasers with wavelengths of λ_r= 656 nm, λ_g= 527 nm, and λ_b =440 nm were used. To keep it short, lasers are labeled red, green, and blue in the following order. First, the lasers are aligned parallel to the optical table by using two reflective mirrors by beam walking method. As shown in Fig. 3.1, these lasers are paired with linear polarizers to ensure that the polarization direction is vertical, i.e., along the x axis. A spatial filter (SF) is used in each laser arm to focus the beam to a waist where a pinhole passes the focused beam and blocks all other beam artifacts. Next, the diverging beam from the pinhole is collimated by a plano-convex lens. The diameter of each wavelength's collimated beams is approximately the same size, i.e., 5mm. The focal lengths of the lenses in SF were chosen carefully so that three beams could expand and collimate with about equal diameters. Two dichroic beamsplitters, DM1 (IDEX/Semrock, LM01-552-25) and DM2 (IDEX/Semrock, LM01-466-25), with cut-off wavelengths of 552 nm and 466 nm, respectively, are used to combine three laser beams into practically a white beam.

The initial objective of this research is to capture holograms of freely flowing aerosols as they pass through the sensing region. The camera and lasers are set to pulse mode to capture the moving particles in the frame. In pulsed mode, lasers are engaged for a short period with a variable repetition rate; the output intensities of laser beams for each pulse were not similar. Short pulses are challenging to produce, especially at high pulse repetition rates, as the smaller pulse energy often leads to weaker temporal modulation of net gain over time. The combined beam obtained a different white appearance with each trigger event due to the variations in pulse power. The change is substantial and should not be overlooked. The

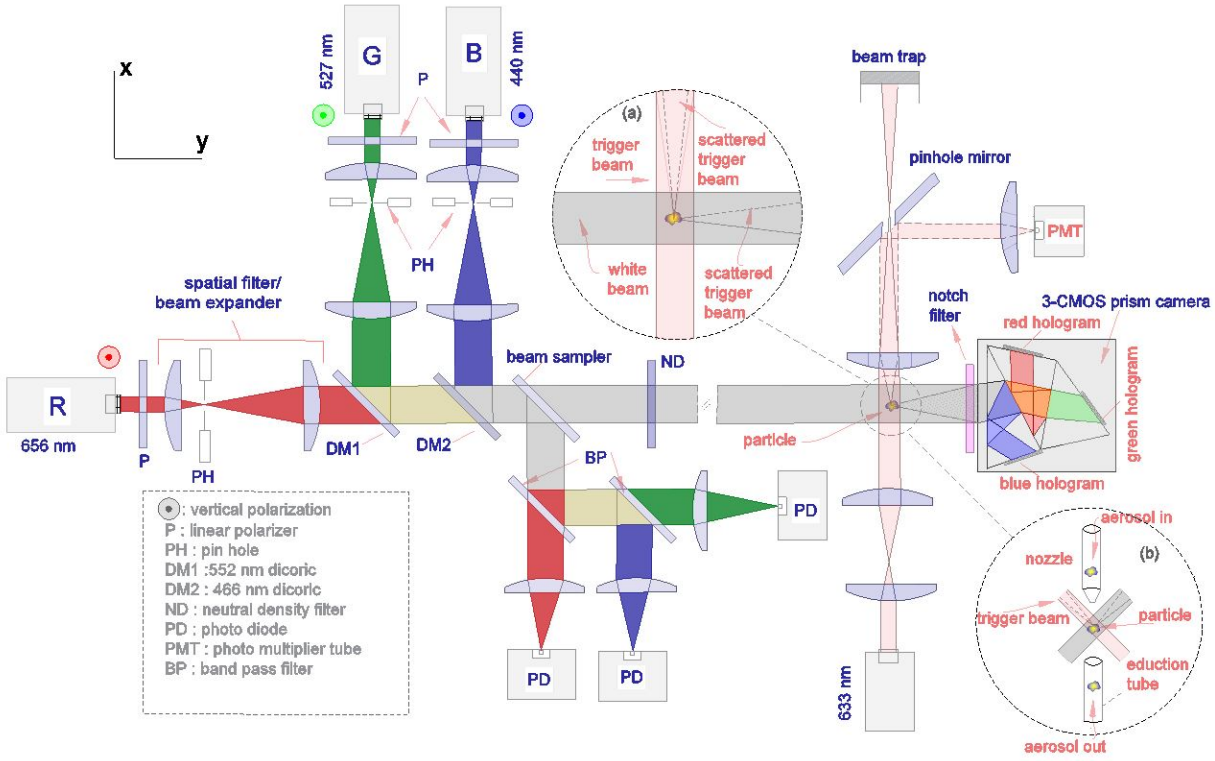


Figure 3.1: Optical setup for forwarding digital holography with multiple wavelengths. Three laser beams having wavelengths of $\lambda_r = 656$ nm, $\lambda_g = 527$ nm, and $\lambda_b = 440$ nm are cleaned, expanded, and merged to make a single white beam. To monitor the intensity fluctuation in each pulse, a beam sample is utilized to pick off the light and quantify it using photodiodes. The free-flowing aerosol particles pass across the trigger beam as they leave the sheath flow nozzle (b). A PMT monitors the trigger event, which initiates a single pulse emission from the three lasers and simultaneously records a hologram in a 3-CMOS color sensor (a).

change in intensity of lasers for each pulse is monitored and computationally implemented later during the reconstruction of holograms. To monitor the laser intensity in each pulse, a beam sampler is used to pick off the beam by reflecting 1% while transmitting 99 % of beam intensity. Then, using band-pass filters, the reflected combined beam is split into red, green, and blue beams, and the intensities of each were measured with photodiodes via an oscilloscope for each trigger event.

Further, an aerosol generator system is designed to aerosolize the dust from a container made of two components. The first component of the generator is a custom-designed circular glass flask with two side ports and both are threaded. A vent is designed at an angle of

45 degrees to the positive x axis and is used to introduce clean air into the flask via an airtight glass tube through the hole in screw-on cap. The air provides positive pressure on the dry powdered particles. Another capillary tube is inserted airtight into the flask through the second vent designed vertically along the positive x axis to extract the stream of dry particles. The pipe heights can be altered to regulate the amount of aerosol flow, or the positive pressure in the flask can also be adjusted. In addition, a few millimeters of the bottom of the round flask are submerged in an ultrasonic water bath, which gives a mechanical vibration to the core of the flask and, therefore, to the sample powder. Because of the vibration, any aggregation, if present in the sample, is broken, and also, when the aerosols leave the glass flask, they pick up more kinetic energy.

The second component of the aerosol-generating system is a sheath flow nozzle. In this nozzle design, aerosols exit from the glass flask and are passed via the inner tube while clean sheath air is passed through the outer tube, as shown in Figure 3.2.

The sheath air passed through the outer tube that encircled the nozzle's inner tube, mixing with the aerosols as it exited the inner tube. Finally, the aerosol particles and sheath air combine and exit the outer tube through the nozzle. The airflow rate into the round glass flask and the sheath flow tube is regulated by two mass flow meters provided with an adjustable knob on each one.

Finally, the sheath flow nozzle delivers the regulated stream of aerosol particles to the designated sensing zone. Furthermore, for the trigger system, a collimated beam from a CW laser with a wavelength of 632 nm is directed perpendicular to the white beam in the negative y direction and a photomultiplier tube (PMT) is used to monitor it continuously. It is also explained in detail in Chapter 5 below. As the moving aerosol passes across this trigger beam, light is scattered. The particles are subsequently evacuated by an eduction tube once they pass across the sensing region. A positive lens is used to collimate the scattered light while simultaneously concentrating the unscattered light to a waist. At the waist, a 500 um pinhole mirror is positioned at a 45-degree angle to the trigger beam's direction, allowing unscattered light to pass through the hole and into a beam trap. The collimated scattered light is reflected by the pinhole mirror and focused by another positive lens on the PMT's

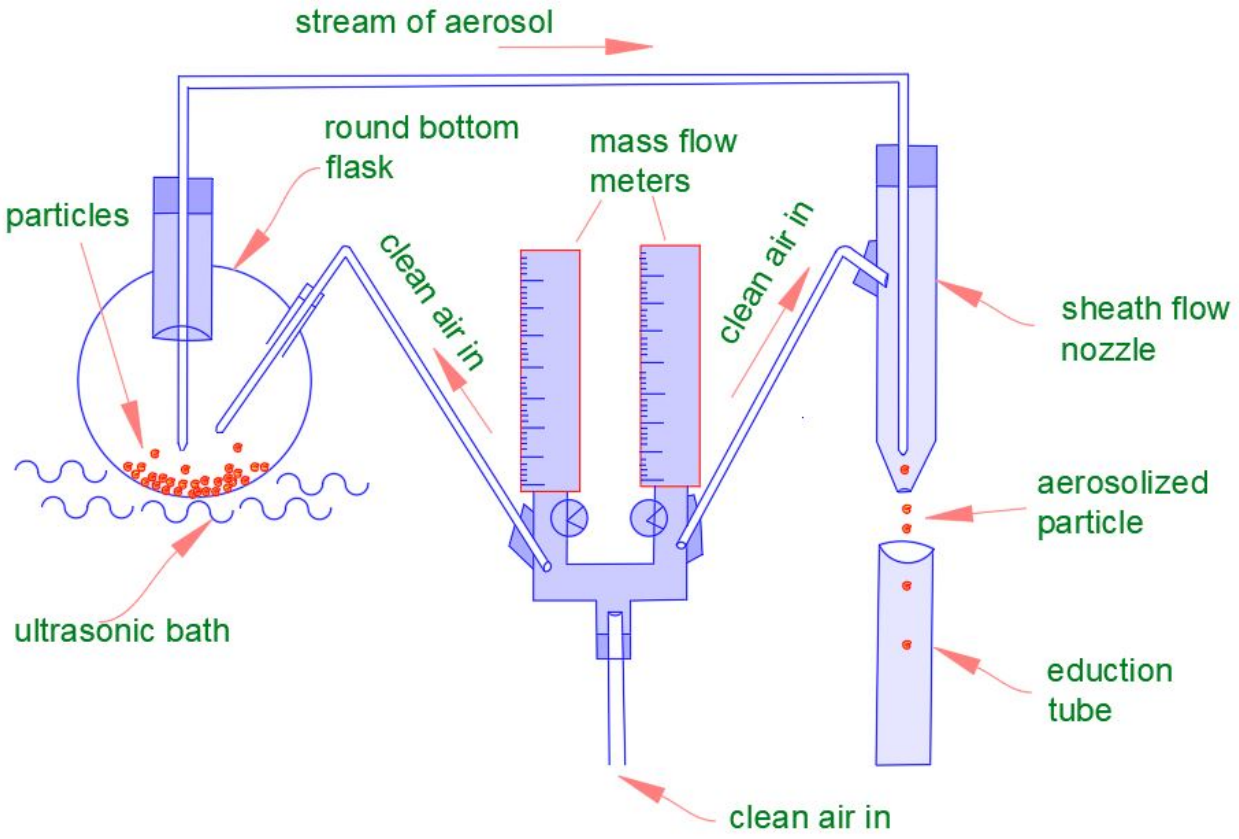


Figure 3.2: Sketch of the aerosol-generating system. The dry powdered sample is kept in a round bottom flask treated with an ultrasonic wave to disintegrate the aggregation. A positive pressure is applied to push the aerosols out. A sheath flow nozzle controls the flow of aerosol, and the exited aerosols arrive at the sensing region and are finally removed through an eduction tube.

sensor plane. The voltage level in the PMT is altered because smaller particles scatter less light than larger particles, which is accounted for by the series of electronic components. As shown in diagram 3.3, an analog processor module (APM) is used to enhance the low voltage signal in PMT due to small particles. Here, the APM divided the signal by 100 after differentiating it; as a result, the high-frequency signal is enhanced while noise is drastically reduced. The signal is further amplified by an amplifier (ORTEC Mo. 570). In addition, the NIM signal is converted to a TTL signal through a NIM-TTL converter (CAEN N59).

Finally, the output signal from the TTL converter is used to trigger a digital delay generator (DDG). When the DDG gets the signal, it simultaneously delivers a trigger pulse to the lasers, the camera, and the oscilloscope. Because the lasers and camera respond to

the trigger signal at different times, the delay in the trigger signal for each component is adjusted in DDG accordingly.

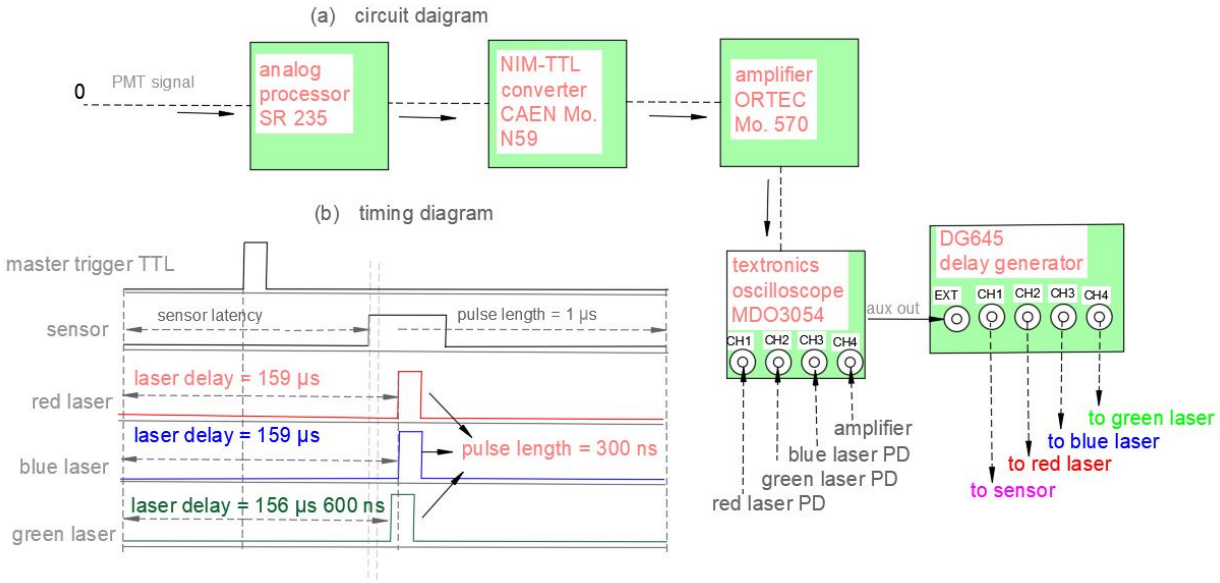


Figure 3.3: (a): The circuit diagram of the electronic system. (b): The timing diagram for the sensors and the lasers. The pulse width is provided to trigger the lasers, and the sensor is set to 300ns. A DDG adjusts the relative latency between the lasers and the sensor.

The transmitted beam from the beam sampler is then used to illuminate the aerosol particles. As stated previously, light is scattered when particles reach the detecting zone. The scattered light, also known as the object wave, interferes with the light not scattered by the particles, i.e., the reference beam. The interference patterns are then received by a color sensor.

A prism sensor (JAI, AP-3200T-PGE 3-sensor) with global shutter capabilities is utilized to record the hologram, that means the entire CMOS array for each channel is read-out at once. This sensor has separate CMOS arrays (Sony, IMX265) for each color channel, i.e., red, green and blue, where the colors are separated by coatings on the prisms as shown in Fig. 3.1. Each array is 2064×1544 pixels with $3.45\,\mu$m $\times 3.45\,\mu$m pixel size. Unlike a Bayer filter sensor, which has a single array with a Bayer filter over it, it records three holograms for each color denoted as $I_{\mathrm{r}}^{\mathrm{holo}}$ for the red channel, $I_{\mathrm{g}}^{\mathrm{holo}}$ for the green channel, and $I_{\mathrm{b}}^{\mathrm{holo}}$ for the blue channel. The camera's spatial resolution is improved about three times since

it uses all of the sensor's pixels. A reference hologram is captured and recorded before the particles are supplied into the sensing zone. The reference holograms for each channel are denoted as $I_{\mathrm{r}}^{\mathrm{ref}}$, $I_{\mathrm{g}}^{\mathrm{ref}}$, and $I_{\mathrm{b}}^{\mathrm{ref}}$. Finally, the contrast holograms are created for each channel by subtracting the reference from the holographic measurements

$$I_{\mathrm{i}}^{\mathrm{con}} = I_{\mathrm{i}}^{\mathrm{ref}} - I_{\mathrm{i}}^{\mathrm{holo}}. \tag{3.1}$$

Where, i represents the individual hologram from each channel, i.e red, green, or blue.

3.3 Result

The sensor's recorded hologram is subsequently digitized, and the contrast holograms for each color are generated, as explained in sec 3.2. The Fresnel diffraction integral, or Rayleigh-Sommerfeld solution to the Helmholtz scalar wave equation that describes the diffraction as the Fresnel approximation simplifies it, can be used to produce images of each color as given by Eq. (2.35). The resolution of the image of a computationally reconstructed hologram depends upon the wavelengths of the laser used to illuminate the object, the distance between the objects and the recording medium, i.e., CCD/CMOS, and the size of a pixel on the array. Consider a simple in-line digital holography arrangement, as shown in Fig. 1.2. If λ is the wavelength of the incident laser, d is the distance between the object plane and the CCD plane, and $\Delta\xi$ is the square pixel size of the CCD. The spatial resolution of the reconstructed image along x dimension can be written as

$$\Delta x = \frac{\lambda d}{N \Delta \xi} \tag{3.2}$$

where N is the total number of pixels along the dimension x of the CCD array.

For the size and white balance calibration of the experiment, soda lime glass microspheres (Duke Standards:Therm-Scientific, Cat No: 9040) of size 40 µm in diameter are aerosolized, and the single-shot RGB hologram is recorded using pulsed lasers as explained in figure 3.1.

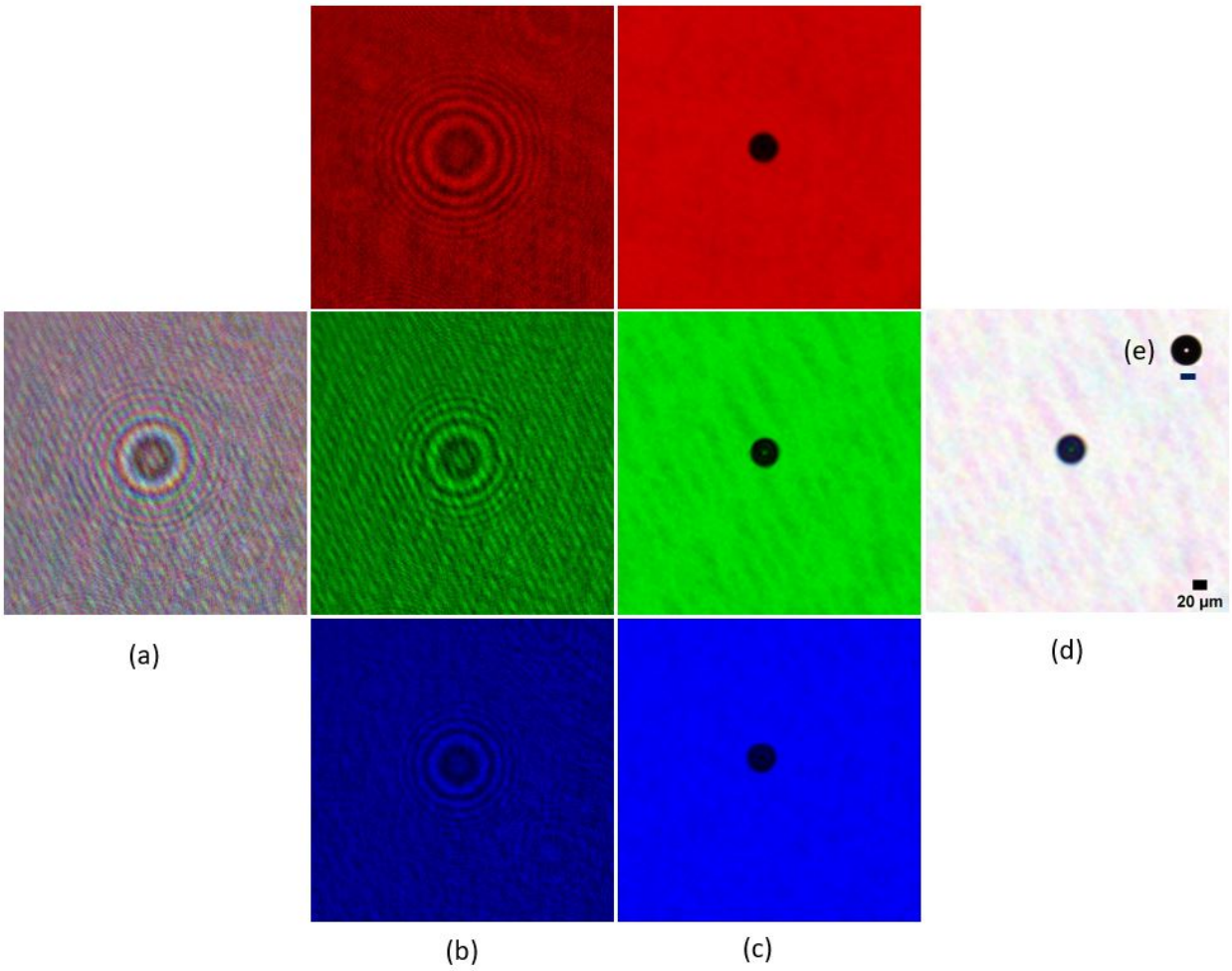


Figure 3.4: (a) A contrast hologram of an aerosolized clear glass micro-sphere of size $40\mu m$ recorded in MWDH. (b) The separation of contrast hologram into the RGB color channels. (c) The Image is reconstructed from the separated color channels for each color channel. (d) The Image is obtained by combining RGB channels and white balance the background. (e) white light transmission microscopic image of the same glass sphere, and the scale bar is $20\mu m$.

The RGB hologram is then computationally separated into red, green, and blue channels by the color-separation method. The red, green, and blue holograms are then individually reconstructed using Kirchoff's Fresnel diffraction theory, as explained above. The obtained images are then considered for the red, green, and blue channels and combined into one image applying the additive color principle. Figure 3.4(a) represents the contrast hologram of the sphere, which is obtained by subtracting the reference hologram from the raw hologram according to Eq. 3.1. The color separated into three channels (RGB) from the contrast

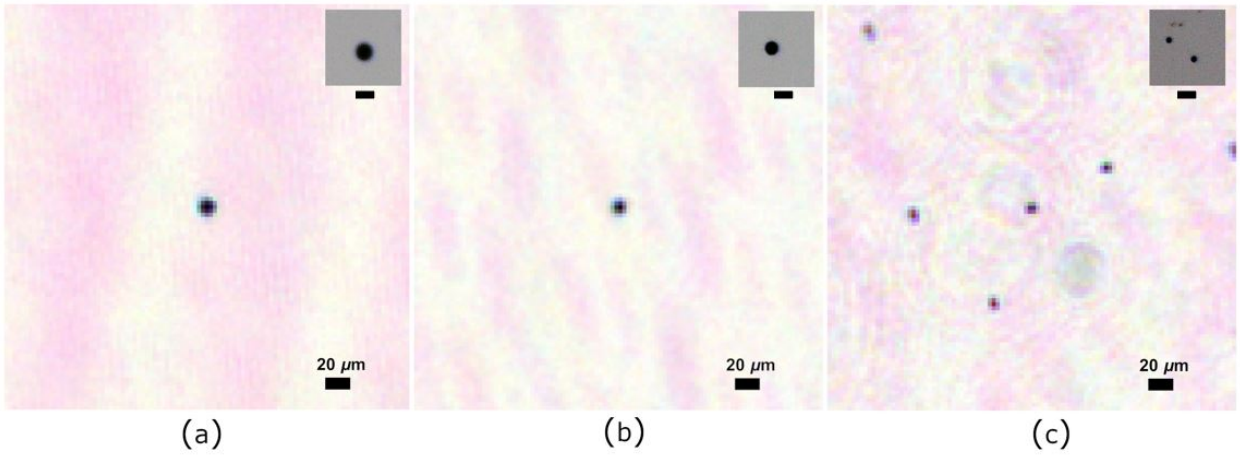


Figure 3.5: The resolution test of the experiment. The clear glass spheres (a) 20 μm,(b) 10 μm, and (c) 5 μm were aerosolized, and the holograms were recorded. The holograms were reconstructed to generate the images.The scale bar on inset images is 20 μm.

hologram is represented by Fig. 3.4(b). The individual channels are then reconstructed according to the Eq. 2.35. The absolute square value of K that produces the monochrome images for each channel is shown in Fig. 3.4(c). Finally, the monochrome images are combined to produce the final image of the microsphere, as shown in Fig. 3.4(d). Since the intensities of the used lasers are not equal, it is critical to balance the image's background. Therefore, for calibration, each channel image's background intensity is normalized. In forward scattering holography, most of the incident light on the particle is passed unscattered, and the addition of the unscattered light in the background of the image should appear white to represent the equal intensity of lasers. The inset Fig. 3.4(e) is the image of the same sphere obtained from the white-light color microscope in transmission mode.

Furthermore, to understand the resolution of the experiment, various sizes of glass spheres are aerosolized to record the digital holograms. The sizes of the microspheres are consequently decreased from larger sizes to smaller sizes, and the images are obtained. Figures 3.5 (a), (b), and (c) are images obtained from the reconstruction of the holograms of clear glass spheres of sizes 20 μm, 10 μm, and 5 μm, respectively. The images demonstrated the ability to achieve the resolution limit of the experiment, which is $\leq$ 5 μm. We tested with smaller sizes of the spheres as well, for example, 2 μm, but due to the small mass/size, the

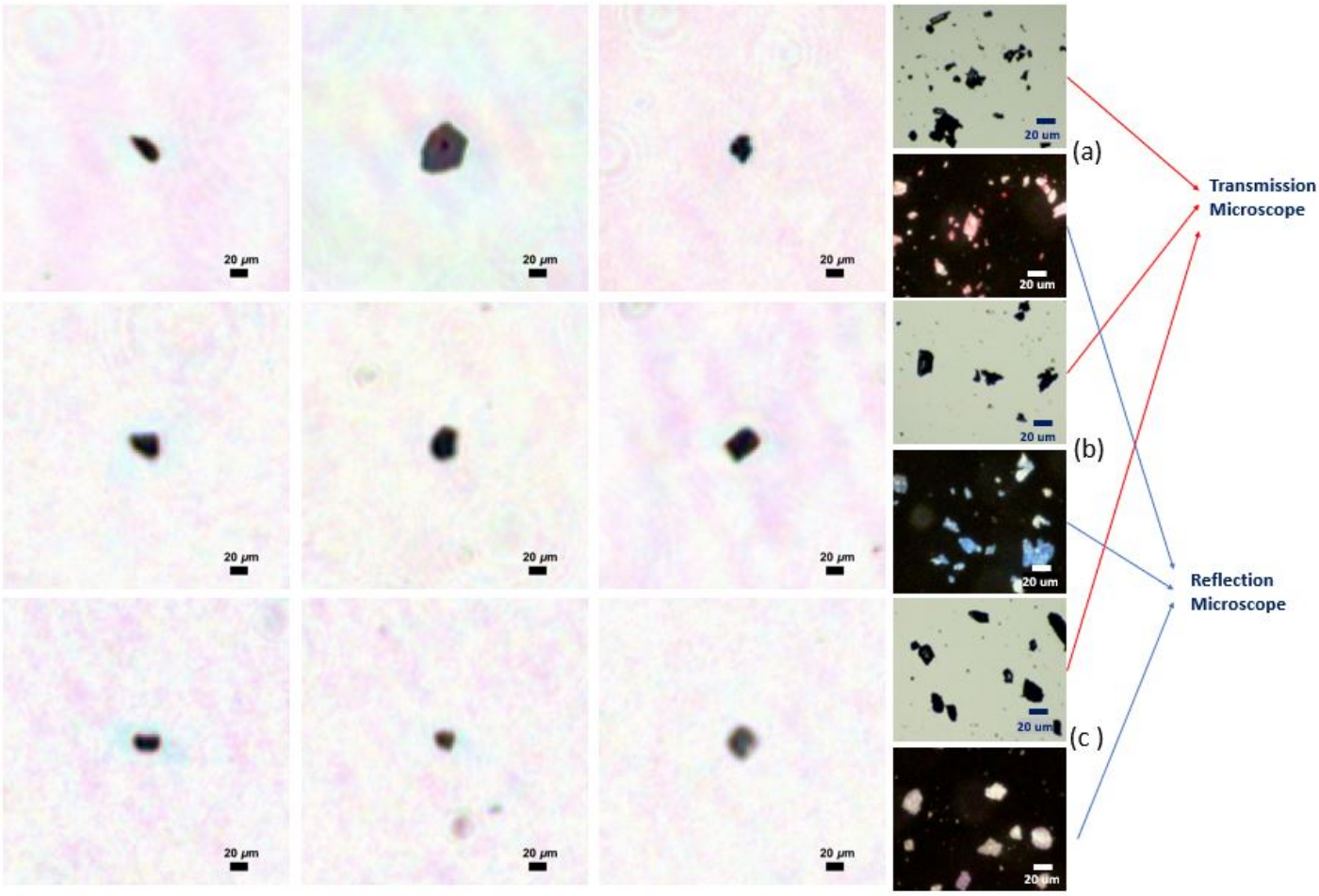


Figure 3.6: Images obtained from aerosolized dust particles of various shapes and sizes using MWDH. The insets (a-c) are the images obtained from the white-light microscope, the top are the images obtained in transmission mode, and the bottom images are from reflection mode.

particles move too fast, and it is hard to capture the holograms with this pulse duration.

Different colored sand samples were collected to see if multispectral forward digital holography could demonstrate the color signature of aerosol dust. The sand grains are then crushed and cascaded through various sizes of sieves to separate a specific size range of particles. After that, the dry powder is aerosolized, and the holograms were recorded. Figure 3.6 shows the image that reconstructed the holograms for various samples of varying shapes and sizes. The insets (a), (b), and (c) in Fig. 3.6 show transmission and reflection microscope images. The images from the holograms and the microscope clearly show that the aerosolized dust particles do not exhibit any color signature.

3.4 Discussion

This study examines whether forward scattering in-line digital holography can measure the aerosol particle's color characteristics. Although the experiment did not reveal any color of the aerosol particles, it helped in developing a new design and selection of experimental assemblies for a more complex backscatter MWDH experiment, which is explained in the following chapters. The low power of the lasers, which is insufficient to penetrate the samples, might explain why we cannot view the samples' color information. Another possibility is that the aerosol samples we studied are opaque enough to prevent light from passing. These facts are further supported by the microscope images taken in transmission mode, which also do not exhibit any color signature of the particles shown in Figure 3.6 (a-c). However, the concept of forward MWDH has a potential to characterize samples in many other scientific fields of study, for example in biological samples with decent transmission of light. From this study one can realized that, to observe the color signature from the such opaque aerosol particles, a backscatter digital holography is necessary.

Chapter 4

Backscatter Multiple Wavelength Digital Holography

The content of this chapter is based on Giri and Berg [83].

4.1 Introduction

In this work MWDH approach is used to image stationary micro-particles in color. A Michelson interferometer is used to mix reference light with weak-intensity light backscattered from a distribution of particles. To enable color images, three CW lasers with differnet wavelengths are used as primary light sources. Three separate backscattered holograms are recorded simultaneously, one for each wavelength using a three-CMOS prism sensor. A variety of colored polyethylene micro-spheres and nonspherical dust particles are used to demonstrate the feasibility of the experiment and illustrate the effect of simple speckle-noise suppression and white balance methods. Finally, a chromaticity analysis is applied that is capable of differentiating particles of different color in a quantitative and objective manner.

This work is motivated by aerosol science and technology, where a general interest is the determination of individual aerosol-particle size, shape, and material composition [120]. Such information is important in many contexts including atmospheric science, national security,

medicine, and industrial manufacturing among others [33, 120–123]. While a variety of methods are available to provide some of these particle characteristics, such as elastic light scattering methods, the most effective is an imaging approach. The difficulty, however, is that aerosol particles often cannot be collected or immobilized for analysis with conventional microscopy. Here, digital holography with its contact-free ability becomes an ideal choice because particle size and shape are easily determined provided that a well-resolved image is obtained. A number of examples are available to illustrate the effectiveness of digital holography for this purpose including the imaging of free-flowing particles in the laboratory [124–127], in the outdoor environment from an unmanned aerial vehicle [111] and aircraft [128], and as a ground-based instrument [110].

In the majority of cases in the literature, a single wavelength is used, wherein the resulting image is monochrome in nature [129]. However, it is possible to employ multiple wavelengths and obtain a colorized image [130–133]. Again, this can be understood by the similarity of digital holography and conventional microscopy. Colorized images are useful in material analysis, biomedical imaging in the study of tissue structures, water quality, and the analysis of stained tissue sections [134–136]. Moreover, a hologram can be formed from light scattered by the particle either around the forward-scattering direction or around the backward-scattering direction [137, 138]. The resulting image then takes the appearance of a light-transmission or reflection image, respectively. Indeed, some authors refer to the forward and backward holograms as transmission and reflection holograms, respectively. There is no physical difference between these terms [139], i.e., between backscattering and reflection etc.

Backscatter holography presents a unique opportunity for particle characterization. The color of an opaque object that one sees when it is illuminated by white light is due to the spectral components that *reflect* from the object [133, 140]. And, this reflection is governed, in part, by the material composition. Thus, it is plausible that backscatter holography carried out with multiple wavelengths could provide information about particle material, which is perhaps the most difficult aerosol characteristic to obtain.

The following presents an application of multiple wavelength digital holography (MWDH) in the backscatter configuration with the goal of discriminating between particles of different

color. Due to the difficulty of aerosol handling and control, this initial effort is carried-out on particles that are stationary on a transparent stage, a window. However, it is emphasized that immobilizing particles is not required and most of the methods developed would apply to free-flowing aerosol particles in future work. The particles considered are relevant to the largest category of atmospheric aerosols, which are called the coarse mode, consisting of particles larger than one micrometer. While MWDH is achieved by others in various contexts [130, 131, 141–143], this work is the first to apply it to objects of this scale, i.e., coarse-mode particles. To the authors' knowledge, the work is also the first to develop a MWDH-image analysis that enables a quantitative discrimination of particles of differing color. This is achieved by chromaticity analysis applied to the color image, where the magnitude of different wavelength components resolved in the image represent a signature for a given particle class.

4.2 Optical arrangement

Figure 4.1 shows the optical layout of MWDH. The lasers used are CW and consist of a 21 mW He-Ne $\lambda_r = 633$ nm laser, a 100 mW $\lambda_g = 532$ nm solid state laser, and a 10.3 mW $\lambda_b = 430$ nm solid state laser. For brevity, these lasers are called red, green, and blue in the following. Each beam passes a liner polarizer (P) and is then cleaned and expanded by a spatial filter. The lenses of the spatial filter are selected to expand the beams to approximately the same diameter, 5 mm, and are then combined by two dichroic beamsplitters (DM1) and (DM2). These beamsplitters are the same as used in Chapter 3. The combined beams appear nearly white in color. The white beam passes through another linear polarizer to ensure polarization in the vertical direction, which is the x-axis as shown in Fig. 4.1. Then, the beam passes through an achromatic quarter-wave plate (QWP) with its optical axis oriented at 45° to the x-axis to produce circular polarization for reasons that will be explained below.

Next, an achromatic lens (ACL) focuses the white beam through an iris to a waist at a 45% reflection, 55% transmission pellicle beamsplitter (Thorlabs, BP145B1). The portion of the beam transmitting through the pellicle, along the positive y-axis, expands from its

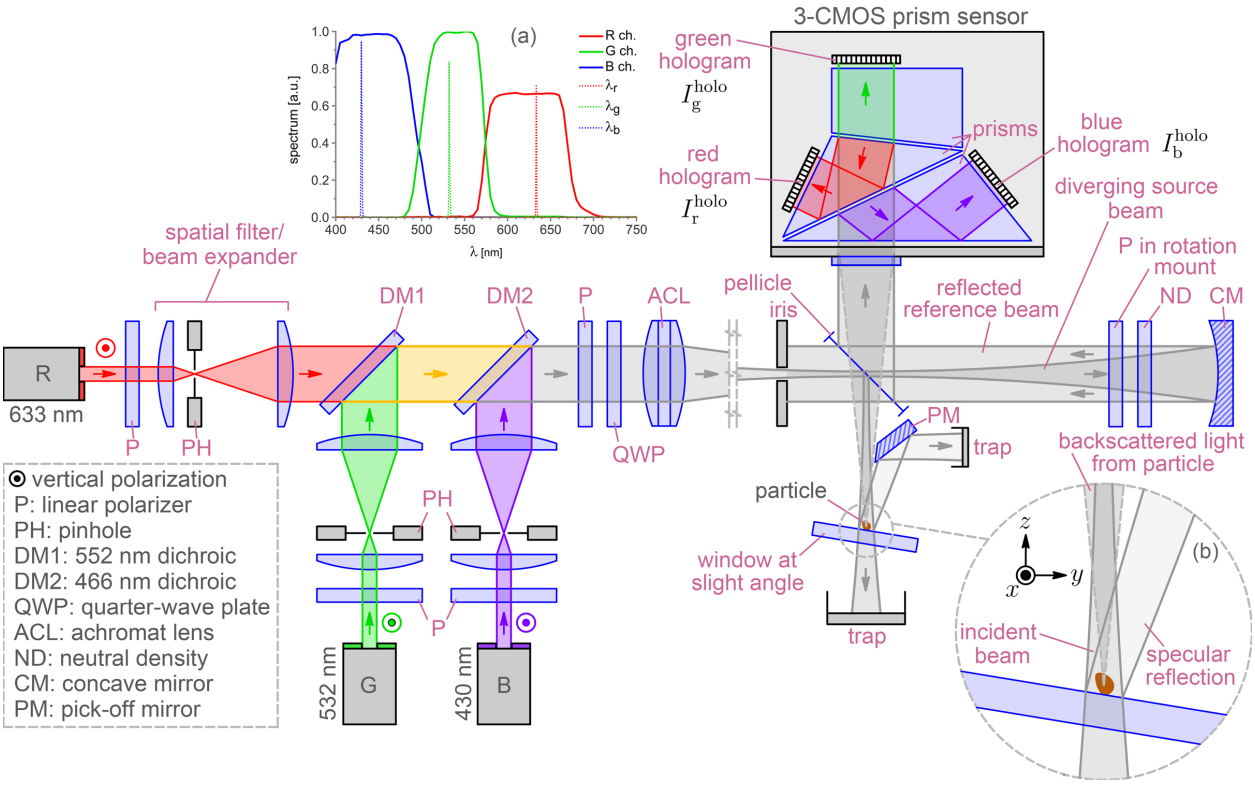


Figure 4.1: Optical arrangement for backscatter multiple wavelength digital holography. Three CW laser beams of wavelengths $\lambda_r = 633$ nm, $\lambda_g = 532$ nm, and $\lambda_b = 430$ nm, are cleaned, expanded, and combined to form a single white beam. The beam is focused to a waist at a pellicle beamsplitter where approximately half proceeds and expands as it reaches a concave mirror. There it is retro-reflected and collimated, and then reflected again by the pellicle to constitute the reference beam at the sensor. The other half of the beam illuminates a sample of micro-particles on an anti-reflection coated window. Backscattered light from the particles that transmits through the pellicle reaches the sensor, constituting the object beam. The inset plot (a) shows the spectral response of the sensor's color channels along with the laser spectra while the other inset, (b), shows how specular reflection from the window is rejected. Further discussion is provided in the text.

waist and passes through another linear polarizer and a neutral density (ND) filter (Thorlabs, NE20A-A). This polarizer resides in a motorized rotation mount (Thorlabs, K10CR1), which allows the direction of the resulting linear polarization of the beam to be rotated by an angle θ_p in the x-z plane without diminishing the beam intensity, aside from the attenuation of the ND filter. The beam, which continues to expand, is then retro-reflected and collimated along the negative y-axis by a 100 mm focal length concave mirror (Thorlabs, CM508-100-P01), passes back through the ND filter and polarizer, and then reflects off the pellicle along the

positive z-axis to the sensor. This collimated beam at the sensor constitutes the reference wave required in digital holography.

The portion of the white beam incident on the pellicle that reflects from it travels, diverging, along the negative z-axis to illuminate the particle sample. A small portion of this incident beam is backscattered by the particles, see Fig. 4.1(b), and this scattered light travels along the positive z-axis, through the pellicle, to the sensor to constitute the object beam in digital holography. The particles reside on a 2 mm thick anti-reflection (AR) coated window. Even with the AR coating, there is an unavoidable small amount of light that specularly reflects and this enough to overwhelm the intensity of the weak object-beam at the sensor. For this reason, the window is slightly tilted to divert the specular reflection to a small pick-off mirror (PM) where it is then sent to a beam trap and prevented from affecting the sensor's measurement. The portion of the beam that does not scatter from the particles and transmits through the window is discarded in another beam trap. The use of a trap here is important to prevent additional portions of the beam from backscattering to the sensor. The sensor used in this work is also the same that we used in forward MWDH experiment. More details about the sensor is in Chapter 2.

In this configuration, the object beam consisting of backscattered light from the particles interferes with the reference beam to form three holograms, one for each color channel. These are denoted $I_{\mathrm{r}}^{\mathrm{holo}}$ for the red channel, $I_{\mathrm{g}}^{\mathrm{holo}}$ for the green channel, and $I_{\mathrm{b}}^{\mathrm{holo}}$ for the blue channel. Recall that these interference patterns also depend on θ_{p} describing the (linear) polarization direction of the reference beam. Next, the particles are removed, which removes the object beam at the sensor, and measurements of the reference beam are made in each channel. These are called reference measurements, $I_{\mathrm{r}}^{\mathrm{ref}}$, $I_{\mathrm{g}}^{\mathrm{ref}}$, and $I_{\mathrm{b}}^{\mathrm{ref}}$. Finally, the difference between the reference and hologram measurements is formed to constitute contrast holograms [126] as Eq. 3.1.

4.3 Image rendering

It is now well established that an image of the objects (particles) producing the object beam can be computationally rendered from the interference pattern of the contrast hologram, e.g., see [63, 144]. In the so-called in-line configuration, the hologram is produced by interference of the portion of the illumination beam that scatters from a particle, around the *forward* direction, with the unscattered portion of the same beam [126]. The image is then rendered from the hologram using Fresnel diffraction theory (FDT) [144]. Here however, the hologram is formed by interference of *backscattered* light with the reference beam. The configuration is still in-line as the interfering beams co-propagate along the same axis and an image can be rendered using the same FDT [138].

Figure 4.2 depicts the image rendering process. The axes in this figure correspond to those in the experimental arrangement, Fig. 4.1. A particle is illuminated by an incident beam propagating along the negative z-axis. A small portion of the light is backscattered, which along with the reference beam, propagates along the positive z-axis to interfere across any of the sensor's CMOS arrays. An array's surface is denoted by $\mathcal{S}_\mathrm{h}$. Each array is characterized by an $N \times N$ square array of $\Delta x \times \Delta x$ square pixels. In actuality, the sensor arrays are rectangular, i.e., 2064×1544 pixels. However, when the image is read from the sensor, it is symmetrically cropped relative to the array center to retain only the $N \times N$ portion, i.e., 1544×1544. Note that the distance between the particle and sensor is $z = d$, which will be a slightly different value for each array due to the different locations of the arrays in the sensor.

Once the interference pattern in each color channel has been digitized and the contrast holograms have been formed as explained in Sec. 4.2, each is used in the Fresnel diffraction integral to render an image. This integral is the Rayleigh-Sommerfeld solution to the Helmholtz scalar wave equation describing diffraction simplified under the Fresnel approximation [144, 145]. Specifically, it reads

$$K(x, y, z, \lambda_i; \theta_\mathrm{p}) = \iint_{\mathcal{S}_\mathrm{h}} I_i^\mathrm{con}(x', y'; \theta_\mathrm{p}) h(x - x', y - y', z, \lambda_i)\, \mathrm{d}x' \mathrm{d}y' \tag{4.1}$$

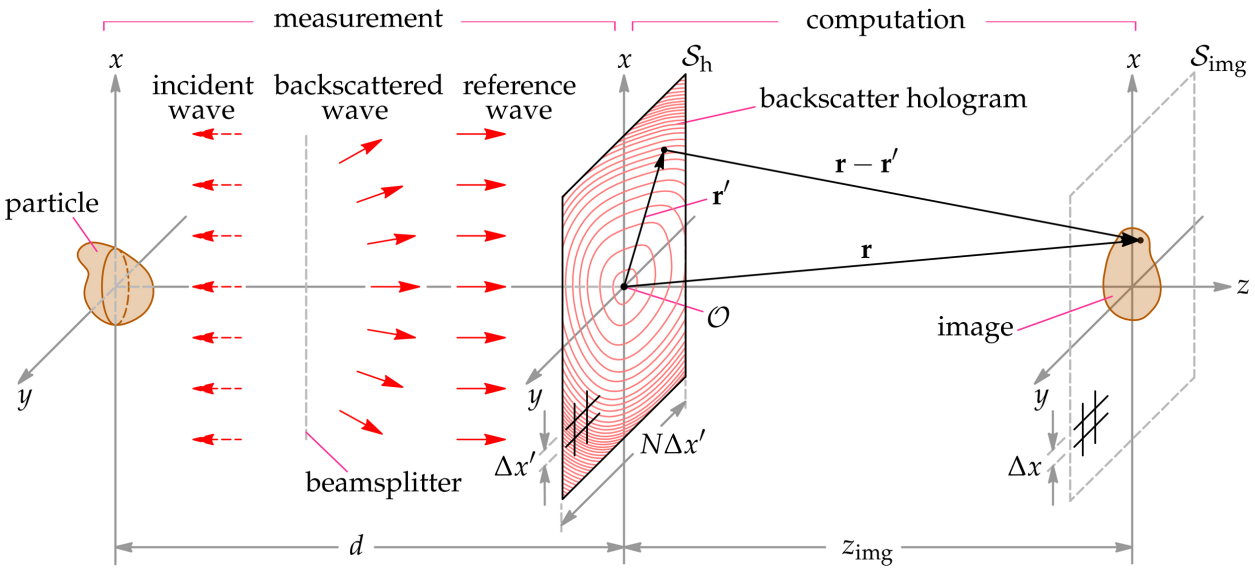


Figure 4.2: *Image rendering process from a contrast hologram. Light backscattered from a particle interferes with reference light across one of the sensor's CMOS arrays*/Image rendering process from a contrast hologram. Light backscattered from a particle interferes with reference light across one of the sensor's CMOS arrays, denoted by the $\mathcal{S}_\mathrm{h}$ plane, to form a fringe pattern. The separation between the particle and sensor is approximately d. The pattern is sampled by the array's pixels, digitized, and then supplied to the Fresnel diffraction integral, (4.1). Evaluation of the integral across $\mathcal{S}_\mathrm{h}$, carried out in primed coordinates, for points across the $\mathcal{S}_\mathrm{img}$ plane, using un-primed coordinates, yields the diffracted wave amplitude, K of (4.1). The absolute value of this amplitude equates to a silhouette-like image of the particle if $z = z_\mathrm{img} \approx d$. The size of the sensor's pixels is $\Delta x'$ whereas the size of the pixels in the image plane is Δx; these values are equal when (4.3) is used.

where K represents the complex amplitude of the diffracted wave for the λ_i corresponding to a given color channel, which is indicated by the subscript i in I_i^con. In (4.1), h is the impulse response of free space,

$$h(x, y, z, \lambda_i) = \frac{\exp\left(2\pi i z/\lambda_i\right)}{i\lambda_i z} \exp\left[\frac{i\pi}{\lambda_i z}\left(x^2 + y^2\right)\right]. \tag{4.2}$$

Note that (4.1) takes the form of a convolution integral, and thus, can be efficiently evaluated using Fourier transforms and the convolution theorem [63], i.e.,

$$K(x, y, z, \lambda_i; \theta_\mathrm{p}) = \mathcal{F}^{-1}\left\{\mathcal{F}\left[I_i^\mathrm{con}(x', y'; \theta_\mathrm{p})\right] \circledast \mathcal{F}\left[h(x', y', z, \lambda_i)\right]\right\} \tag{4.3}$$

In (4.3), $\mathcal{F}$ represents the forward Fourier transform and $\mathcal{F}^{-1}$ is the reverse (inverse) transform. The symbol $\circledast$ is the Hadamard product, i.e., the element-by-element product. The diffracted wave produced by (4.3) is evaluated in the $\mathcal{S}_{\text{img}}$ plane, which is parallel to $\mathcal{S}_{\text{h}}$ but separated by a distance z_{img}. When $z_{\text{img}} \approx d$, the magnitude of the diffracted wave, $|K|$, converges to form a silhouette-like image of the particle similar in appearance to what would be obtained from a microscope.

4.3.1 Speckle suppression

Before discussing how the images from the various color channels are combined to render a color image, the problem of speckle noise should be briefly reviewed. The highly coherent nature of the light sources makes such noise inherent to imaging with digital holography. Indeed, for the red laser, being a HeNe means that its coherence length is likely on the order of a meter or greater. For the green and blue lasers, it is estimated that their coherence length is far smaller, on the scale of millimeters, but still much larger than the particles studied. Speckles are due to the interference of portions of the laser light scattering from random, rough features on the surfaces intercepting the beam. In the context of this work, speckle noise manifests as grain-like domains of sharply varying intensity several pixels in size that are randomly distributed across the particle image. Speckle grains exhibit several statistical characteristics that are related to the optical arrangement. As explained by Bianco et al. [146], the mean size of a speckle grain $\Delta\eta$ in terms of the sensor pixel size $\Delta x'$ is

$$\Delta\eta_i = \frac{d\lambda_i}{N\Delta x'}. \tag{4.4}$$

Note from (4.4) that the speckle grains are wavelength dependent, and thus, will differ between the color channels. In this work, the grains are $\Delta\eta_i < 10\Delta x'$ for all channels.

Speckle noise in digital holography is a well-studied topic and numerous methods are available to suppress the effect to varying degrees [146–153]. The approach taken here relates to the varying linear polarization directions produced by the rotating polarizer following

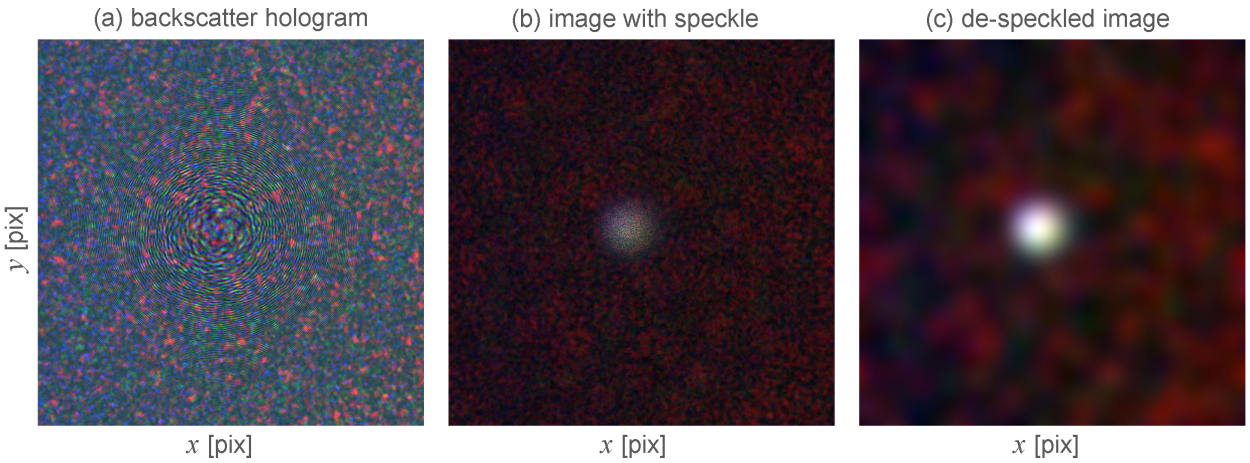


Figure 4.3: Examples of speckle and its reduction in backscatter MWDH. In (a) is a backscatter color contrast hologram $I_{\text{rgb}}^{\text{con}}$ formed by the white-beam spot on a reflectance standard in place of the window in Fig. 4.1. Only a single polarization direction for the reference beam is used here, $\theta_{\text{p}} = 0°$. Reconstruction of beam-spot image from this hologram is shown in (b). In (c), is the image after all polarization directions are included, (4.5), and the filtering of (4.6) is applied.

the QWP in Fig. 4.1. For each polarization direction, the speckle distribution in a given channel's particle-image changes slightly because reflection (or backscattering) is polarization dependent. Due to the random nature of the distribution, it is then plausible that averaging the images as the polarization is changed will reduce the overall impact on the image quality. This is the reason that the polarizer is mounted in a motorized rotation stage. A set of holograms and reference measurements are taken as the polarizer rotates θ_{p} from 0° (the positive x-axis) through 180° in 20° steps. Recall that because the polarization state of the white beam is circular following the QWP, the rotating polarizer does not alter the beam intensity. Then, contrast holograms are formed for each color channel and polarization direction and images are rendered via (4.3) for each. The i^{th} channel's average image is then given by

$$|K(x, y, d, \lambda_i)| = \frac{1}{N_{\text{p}}} \sum_{j=1}^{N_{\text{p}}} |K(x, y, d, \lambda_i; \theta_j)| \,, \tag{4.5}$$

Even with the polarization-based speckle suppression, significant speckle noise remains in the images. Further suppression of the speckle is possible by convolving a channel's image $|K|$ from (4.5) with a two-dimensional Gaussian kernel G to generate a de-speckled image

$|K'|$ as

$$|K'(x,y,d,\lambda_i)| = \iint_{\mathcal{S}_{\text{img}}} |K(x',y',d,\lambda_i)|\, G(x-x',y-y')\,\mathrm{d}x'\mathrm{d}y' \tag{4.6}$$

where the kernel is given by

$$G(x,y) = \frac{1}{2\pi\sigma^2}\exp\left[-\left(\frac{x^2+y^2}{2\sigma^2}\right)\right]. \tag{4.7}$$

The effect of applying (4.6) to an image is to blur it uniformly. The parameter σ^2 in (4.7) is the variance, which determines the extent of the added blur. Here, the variance is $\sigma^2 = (\alpha\eta_i)^2$ where $\alpha = 10$ such that the amount of blur is limited to roughly ten speckle grains for a given color channel. This blurring reduces speckle noise but at the loss of spatial (image) resolution.

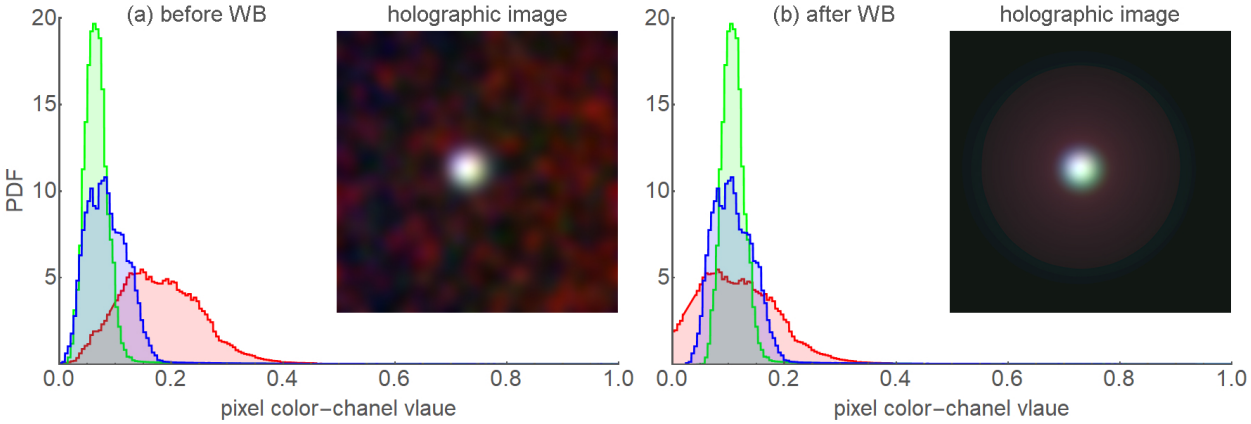


Figure 4.4: Demonstration of the simple white balance (WB) method. In (a) is plotted the probability distribution function (PDF) for the pixels in a backscatter color hologram image for the white beam on the reflectance standard; the image is included inset. Here, one can see the mean of each color channel's PDF is different. In (b) is shown the same distribution after the WB procedure along with its effect on the beam-spot image. Both images are de-speckled.

To illustrate the effect of the de-speckling method, Eqs. (4.5), the gray-level images corresponding to the red, green, and blue color-channels are combined to form a color image. This is done by basic color addition where the red channel's (gray-level) image is colored red and then added to the green image colored green and then to the blue image colored blue. The luminance of each color is defined by the gray level of the corresponding channel's

image. For example, if a pixel in the red channel's image has a gray level of zero, which is black, the luminance of red color assigned to that pixel is zero, again black. If the gray level is one, which is white, then the red color has maximum luminance, a value of one. This same procedure can be applied to the contrast holograms $I_{\mathrm{r}}^{\mathrm{con}}$, $I_{\mathrm{g}}^{\mathrm{con}}$, and $I_{\mathrm{b}}^{\mathrm{con}}$ to assemble a color contrast hologram, $I_{\mathrm{rgb}}^{\mathrm{con}}$. Figure 4.3(a) shows an example of $I_{\mathrm{rgb}}^{\mathrm{con}}$ measured when the particle sample is replaced by a white diffuse-reflectance standard. This color hologram is only one of the N_{p} holograms collected as the polarization direction is rotated; here the direction is $\theta_{\mathrm{p}} = 0°$. The white illumination beam backscatters from the standard and the resulting MWDH image is that of the beam spot on the standard. Figure 4.3(b) shows this image, again for only the single polarization direction, and when the blurring method of (4.6) is *not* applied. That is, this image displays full speckle, as does the hologram in Fig. 4.3(a). Finally, Fig. 4.3(c) shows the image after the full de-speckle method is applied. One can clearly see that the speckle effect is diminished to some degree and the beam-spot feature is enhanced.

4.3.2 White balance

One challenge associated with combining multiple single-color (holographic) images to mimic a full-color image is white balance (WB). Simply, WB is the recognition that if equal-luminance single-color images are added, meaning red, green, and blue (RGB) images here, the result should be a gray or white image depending on the specific luminance value. This is the motivation for using the reflectance standard in Fig. 4.3. The standard (Ocean Optics, WS-1) is a white surface with Lambertian characteristics, i.e., matte white, with a nearly uniform reflectance $> 98\%$ over a broad spectral range of 400-1500 nm. Thus, the addition of the color-channel images in Fig. 4.3 should yield a beam spot with a white appearance. While the spot does appear white, the balance between colors is not perfect. For this reason, a WB procedure is justified, which will be especially important for later considerations when particles are examined.

An important factor that contributes to the need for WB is that the lasers are not equal in

power [154]. This results in $I_{\mathrm{r}}^{\mathrm{con}}$, $I_{\mathrm{g}}^{\mathrm{con}}$, and $I_{\mathrm{b}}^{\mathrm{con}}$ with differing-magnitude features producing a color image with unequal color addition for an object that is otherwise white. In other words, the three beams do not constitute an ideal true-white light source. A simple WB method is developed to correct for the unequal laser power and is shown in Fig. 4.4. Here, the de-speckled image in Fig. 4.3(b) is analyzed in terms of the probability distribution function (PDF) for each color channel in the image. The PDF is a way to visualize the distribution of RGB pixel values in a given color channel's image. In Fig. 4.4(a), the distribution of pixel values clearly shows that the mean pixel value for the red channel is greater than the other channels. The WB shifts the pixel values to the average of the means of each channel's PDF. Figure 4.4(b) shows the PDFs after this shift of pixel values along with the resulting image. Note that this WB is not as sophisticated as others used in the literature for related applications [133, 155].

To further illustrate the cumulative effect of the de-speckle and WB methods, consider Fig. 4.5, which shows how the hologram-derived images are layered to generate a colorized image. Here, the reflectance standard is removed and the AR-coated window in Fig. 4.1 is reinstalled. A small amount of white polyethylene micro-spheres are spread across the window. These spheres (Cospheric LLC, WPMS–1.00 45-53 μm–5g) are non-fluorescent and range from $45-53\,\mu$m in diameter. The window is placed as close as possible to the former location of the reflectance standard, with the help of an xyz translation stage, so that the focus-distance d in Sec. 4.3 is nearly the same, and thus, the same WB used for the reflectance standard can be applied. Figures 4.5(a)-4.5(c) show the backscattered contrast holograms in each color channel, $I_{\mathrm{r}}^{\mathrm{con}}$, $I_{\mathrm{g}}^{\mathrm{con}}$, and $I_{\mathrm{b}}^{\mathrm{con}}$, colored accordingly for the $\theta_{\mathrm{p}} = 0^{\circ}$ polarization direction. While it is difficult to see, each hologram features a rich pattern of interference fringes. Figures 4.5(d)-4.5(f) show the particle images resulting from the application of (4.3) to these holograms, again for each color channel and a single polarization direction. In Fig. 4.5(g) is the result of layering the individual RGB images of Figs. 4.5(d)-4.5(f) via additive color mixing to form a single color image. This image shows strong speckle because only a single polarization-direction is considered. Figure 4.5(h), however, shows the color image after all polarization directions are considered, the images are averaged via (4.6),

and the simple WB is applied. Here, it is evident that the speckle is reduced, resulting in a notably improved image. Finally, Fig. 4.5(i) shows a microscope image of the *same* particles.

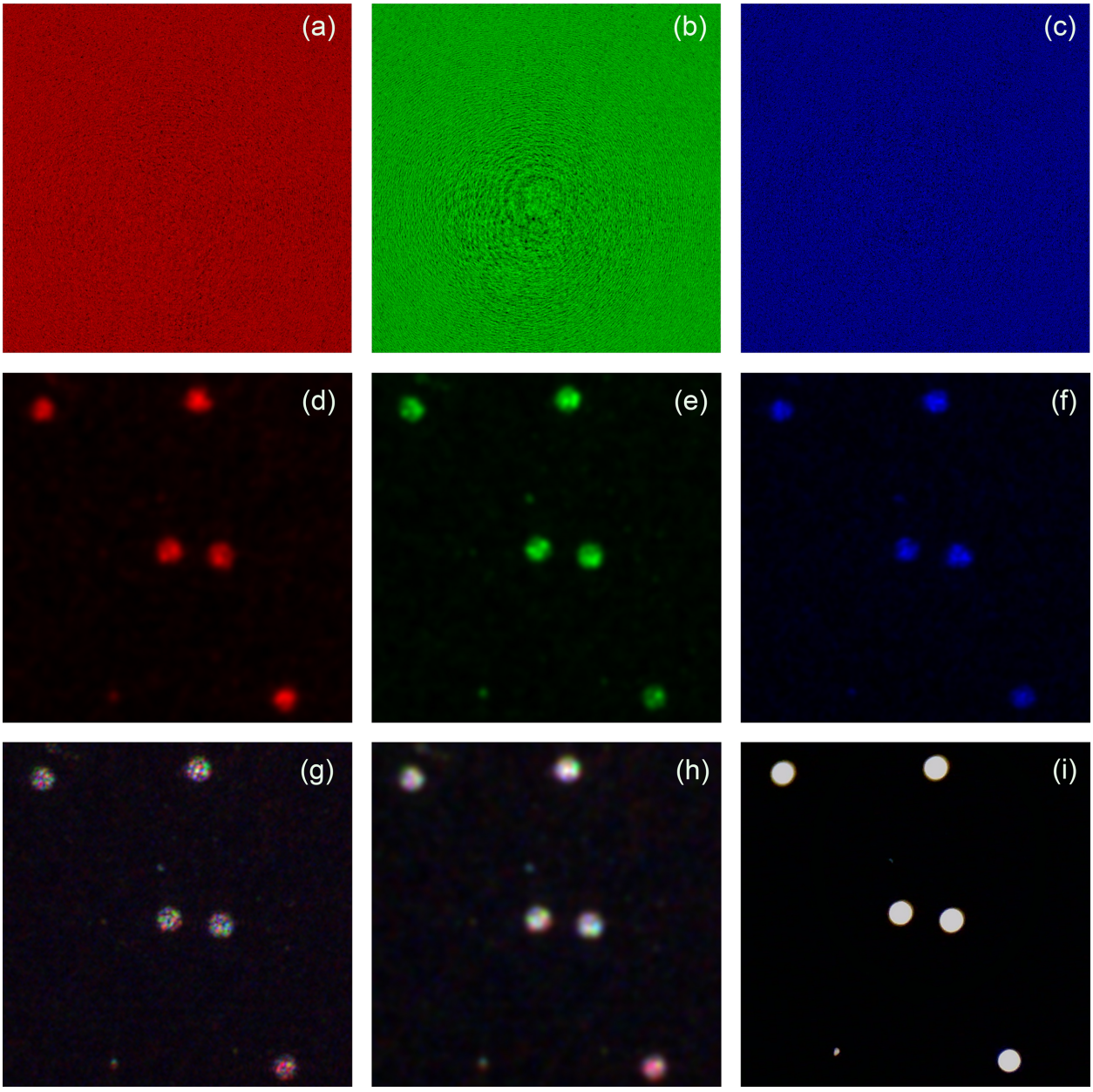


Figure 4.5: Synthesis of color particle-images via additive color mixing. The individual color channel backscatter holograms, $I_{\mathrm{r}}^{\mathrm{con}}$, $I_{\mathrm{g}}^{\mathrm{con}}$, and $I_{\mathrm{b}}^{\mathrm{con}}$ are shown in (a)-(c), respectively, white 50 μm diameter spheres on the window in Fig. 4.1. The particle images resulting from reconstruction of these holograms are presented in (d)-(f). In (g) is the result of adding (d)-(f). Only one of the N_{p} polarization directions is considered for (a)-(g) and strong speckle is evident. In (h) is shown the result of applying the speckle suppression and WB methods, and (i) shows a microscope image of the same particles under epi-illumination.

Figure 4.5 demonstrates several important aspects of MWDH. At the most basic level, it is clear that digital holograms can be formed from the comparatively weak light scattered from micro-particles around the *backward* direction, and this can be done for multiple particles at several wavelengths (R, G, and B) in the visible spectrum. While this has been demonstrated previously for a single wavelength in [138], in most work considering color digital holography of objects at this (small) scale, the holograms are formed with the significantly more intense forward-scattered light, i.e., the conventional in-line configuration, e.g., see [130]. Indeed, the forward-scattered light intensity for a 50 μm diameter glass sphere illuminated by $\lambda_{\mathrm{r}} = 633$ nm light is four orders of magnitude greater than the backward-scattered intensity [156]. The resulting color image following partial speckle-suppression and WB, i.e., Fig. 4.5(h), does represent the particle size and shape well in addition to a fair degree of correct color rendition. This is seen via comparison to the microscope image. However, it is clear that the color rendition is not optimal, meaning that the particles in Fig. 4.5(h) still display uneven pixels of R, G or B, preventing a truly uniform white appearance. The reason for this is the fact that the speckle is wavelength dependent and the de-speckle method used is not able to completely remove the effect. We remind the reader that more sophisticated speckle suppression can be considered, e.g., see [133, 155, 157, 158].

4.4 Chromaticity analysis

A persistent difficulty with analyzing color images is to have a method that can characterize the color characteristics of one image to others in a quantitative way; in particular, a method that avoids the subjective nature of human vision as much as possible. Much work exists on the general topic of color science, color rendering, color perception and the like, and the reader may consult [159–161] for context and details. The approach taken here is that of chromaticity, which has the advantage of characterizing the colors in an image in a way amenable to visual perception while simultaneously doing so with quantitative measures.

Because human color vision involves three types of color receptors, the cones, the perception of color exhibits a property known as trichromacy. This is the concept that given three

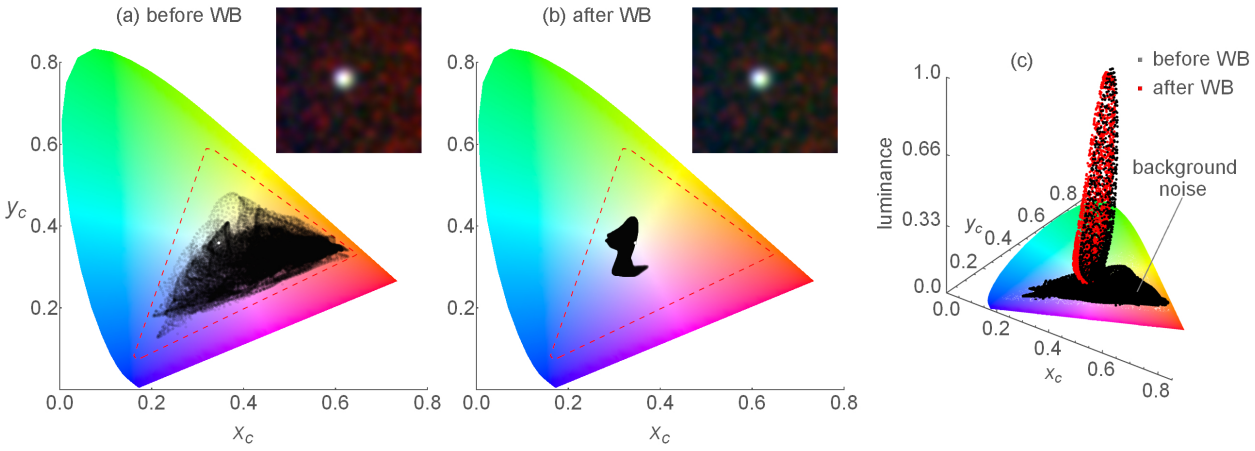


Figure 4.6: Chromaticity analysis of backscatter MWDH images. The distribution of pixel colors in the MWDH image of the beam spot on the reflectance standard is shown in (a) as points in the chromaticity plot. In (b), is the same plot following the WB and noise-thresholding operations. Plot (c) shows the data of (a) and (b) together in a three-dimensional chromaticity plot where the vertical coordinate is the luminance of a given pixel's color. Here, black dots correspond to (a) whereas red dots correspond to (b).

sources of light, each being a primary color such as red, green, or blue, any other perceptible color can be rendered via simple mixing of these primaries, i.e., via color addition. The choice of primaries involves a degree of freedom; they may be nearly monochromatic like the lasers used here, or they may be sources of light with finite bandwidths. An important property of the primaries is that a mixture of any two cannot produce the same perceptual response (color) as the third. The color that one perceives can be described by three tristimulus values, denoted X, Y, and Z by convention [162], which depend on the primaries, and describe the eye's cone sensitivities. The tristimulus values amount to coordinates of a three-dimensional vector in a color space, where the direction specifies the color and the length of the vector specifies the amount of said color, i.e., the color's luminance. By normalizing the tristimulus values by their sum, a new set of values can be defined that do not depend on the luminance and only specify the color. The result is a new color space with coordinates, denoted x, y, and z by convention, and these are known as chromaticity coordinates. To avoid confusion with the spatial coordinates of Figs. 4.1 and 4.2, these will be specified as x_c, y_c, and z_c here.

Because they are normalized, i.e., $x_c+y_c+z_c = 1$, only two of the chromaticity coordinates

are needed to specify any perceptible color as a single point (x_c, y_c) in a two-dimensional plot, which is called a chromaticity plot. The color is represented in this way independent of its luminance, which is an advantage as one can analyze the colors present in an image regardless of the intensity of any given color. An example is shown in Fig. 4.6(a) where the chromaticity plot of the beam spot on the reflectance standard before WB, i.e., Fig. 4.4(a), is shown. Here each pixel corresponds to a point on the plot where the corresponding color is indicated by the background pallet. There is a special point, called the white point, where the primaries balance to produce white. The large spread of points around the white point indicate that the image (inset) contains a diversity of color other than white. Following the WB procedure above and a thresholding of the pixel luminance to remove the speckle noise background, the result is Fig. 4.6(b). One can see that the points are more tightly clustered around the white point, indicating that the image has been transformed to a more balanced color appearance. The luminance of each color point can be recovered from Y and used as a vertical coordinate to produce the three dimensional chromaticity plot in Fig. 4.6(c), where the points for both Fig. 4.6(a) and 4.6(b) are shown in black and red, respectively. Here, one sees that the majority of the points in Fig. 4.6(a) most spread from the white point belong to the dim speckle noise background seen surrounding the the beam spot in the inset in Fig. 4.6(a). Thresholding of this noise and the slight shift of color of the surviving pixels produces the distribution of red points in Fig. 4.6(c).

4.5 Particle discrimination

The purpose of the chromaticity analysis in this work is not to render the most accurate color representation of a particle as possible with respect to human vision, but rather to enable a quantitative, objective method to discriminate particles of different color. To explain how this is done, first consider Fig. 4.7. Here, non-fluorescent colored polyethylene microspheres $45-53\,\mu$m in diameter are deposited on the AR-coated window in Fig. 4.1. The colors of the spheres include the white spheres of Fig. 4.5, red spheres (Cospheric LLC, REDPMS–0.98 45-53 μm–5g), green spheres (Cospheric LLC, GPMS–0.98 45-53 μm–5g), and blue/cyan

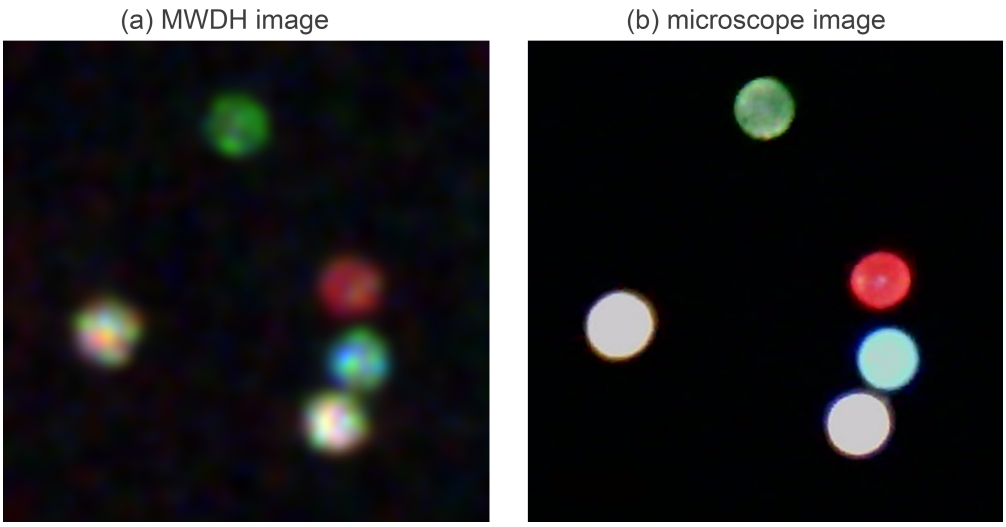


Figure 4.7: Color resolution in backscatter MWDH images. In (a) is the MWDH image for a collection of colored 50 μm diameter micro-spheres with the de-speckle and WB methods applied. In (b) is a microscope image of the same spheres under white-light epi-illumination. The colors of the spheres include white, red, green, and blue/cyan.

spheres (Cospheric LLC, BLPMS–1.00 45-53 μm–5g). Figure 4.7(a) shows the MWDH image reconstructed from a backscattered color hologram $I_{\text{rgb}}^{\text{con}}$ of a collection of these spheres following the de-speckle and WB procedures. For comparison, the same group of spheres as imaged with a microscope in epi-illumination mode is shown in Fig. 4.7(b). This is achieved without disturbing the particles or the window by imaging them via reflection from the pick-off mirror (PM) in Fig. 4.1. When imaged this way, the lasers are shuttered and the microscope's own white light source is used. Because the microscope's light source is broadband with low spatial coherence, there is no speckle. One can see that while the quality of the MWDH image is not perfect and speckle-noise remains, the image does successfully render a color image of the group where the different colors of the spheres is obvious.

The success of the color-resolved image from a single $I_{\text{rgb}}^{\text{con}}$ measurement in Fig. 4.7 is more notable than it may appear. Recall, that the hologram is formed from backscattered light, which is far less intense than forward scattered (or transmitted) light. Being approximately 50 μm in diameter, these particles are significantly smaller than most objects in similar attempts at color imaging with digital holography, e.g., [155]. Perhaps the salient feature of Fig. 4.7(a) is that neighboring particles of different color, which are separated by less than

their respective size, can be distinguished without the color content of one interfering with the other. This can be seen most dramatically in Fig. 4.7(a) for the red and cyan particles.

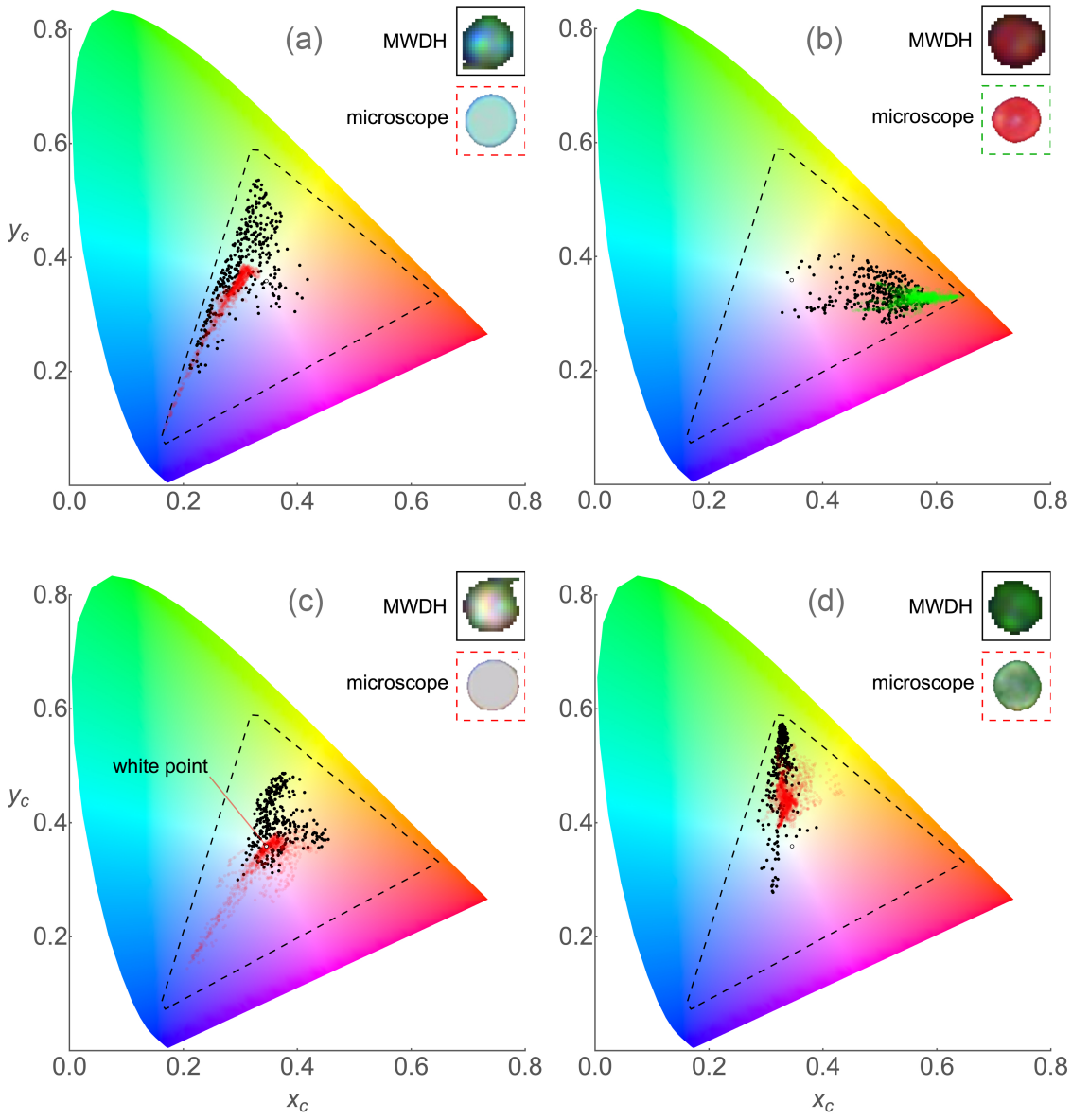


Figure 4.8: Particle discrimination based on color with chromaticity analysis. Each plot presents the chromaticity points for the pixels of an individual particle in Fig. 4.7. The blue/cyan particle is presented in (a), the red particle in (b), one of the white particles in (c), and the green particle in (d). Black points correspond to the MWDH images, shown inset in a black frame, and the red or green points correspond to the microscope images, shown in a dashed frame of the same color. Green points are used in (b) to provide contrast with the chromaticity diagram in the background.

Chromaticity analysis is applied to Fig. 4.7(a) to objectively discriminate particles of

different color in Fig. 4.8. Four sub-images are formed from Fig. 4.7(a) where each is cropped to display only a single particle from the right half of the image in Fig. 4.7(a). Although not required, the black background of each of these sub-images is removed to leave only the particle image without background. Each of these sub-images is shown inset in Fig. 4.8. The same process is applied to the microscope image of Fig. 4.7(b) and these are also shown inset. Then, points are plotted on a chromaticity plot for each sub-image, where the MWDH image corresponds to black points and the microscope image corresponds to the red or green points. In each case, the points are clustered in a portion of the chromaticity plot that is representative of the overall color of the particle. The spread of points indicates a variety of colors are present, which can be verified by close inspection of the sub-images themselves. Overall, however, it is clear that particles of different color are differentiable from the chromaticity analysis in terms of the region of the plot in which the majority of the points appear. Two striking examples are the red and green particles of Figs. 4.8(b) and 4.8(d), respectively. The points are relatively tightly clustered in the red and green portions of the chromaticity plot and one could confidently assign each particle to one of the two colors without visual interpretation of the image. Notice that the darkness of a pixel color in the sub-images has no effect on the position of its corresponding point's location in the chromaticity plot. In other words, the distribution of pixel-points in the chromaticity plot are independent of the variation in brightness across the corresponding sub-image.

If a chromaticity plot of the pixels of the entire image in Fig. 4.7 were made, the result would be equivalent to combining the point distributions of all the plots in Fig. 4.8. In that case, the spread of points in Fig. 4.8, which is due to the remaining speckle noise in the sub-images, would make it difficult to know that there are multiple objects of distinctly different color, i.e., without engaging an observer to make the determination. Yet, as long as the MWDH image has sufficient spatial resolution, it is usually possible to partition it into single particle sub-images and perform the chromaticity analysis without the need for an observer to subjectively assign particles to a given variety of color categories. It is in this sense that chromaticity analysis is regarded as a quantitative means for differentiating particles of different color independent of how an observer may perceive the image.

4.6 Volume imaging with discrimination

The reader may wonder what is the advantage of MWDH imaging over conventional epi-illumination microscopy, especially given the inferior image quality of MWDH in terms of both color rendition and spatial resolution, e.g., recall Fig. 4.7. The answer relates to a number of unique abilities of digital holography and the specific context in which the imaging is done.

Recall from Sec. 4.3 that an image can be rendered from a *single* color hologram in any number of image planes $\mathcal{S}_{\text{img}}$ by simply re-evaluating (4.3) for different values of the focus distance $z = d$. Thus, if particles reside a different axial locations (different z), one can bring each into focus from $I_{\text{rgb}}^{\text{con}}$ post-measurement. This has led to a variety of volume imaging applications [5, 163–165], and in the case of a single wavelength, Subedi et al. [137] shows this can be done over an axial distance greater than 4 cm. For the same to be done with microscopy requires that multiple measurements (images) be taken with mechanical adjustments of the position of the microscope, or optical element within, in order to have a focused image for each axial location. For the stationary particles here, there is little practical advantage for MWDH in this regard as it is straightforward to simply capture multiple images with the microscope. However, if the particles were moving, as would be the case in an aerosol for example, imaging with a microscope would become highly challenging. This is because it is often difficult to control the trajectory of aerosol particles to flow within a volume confined to the microscope's depth of focus. Moreover, the particles generally move too fast for a microscope to be mechanically re-focused.

Figure 4.9 demonstrates the advantage of MWDH in this regard. Here, different particle samples are placed on *both* sides of the window in Fig. 4.1, called side 1 and side 2. On side 1, which is closest to the sensor, the particles are the $\sim 50\,\mu$m diameter white micro-spheres of Fig. 4.5, and on side 2 an axial distance of 2 mm farther from the white particles are yellow-colored chalk-dust particles, with an average size of $\sim 50 - 100\ \mu$m. A single backscattered color hologram $I_{\text{rgb}}^{\text{con}}$ is captured and an image is reconstructed at the two different focus depths corresponding to the axial locations of side 1 and 2. The WB and de-speckling

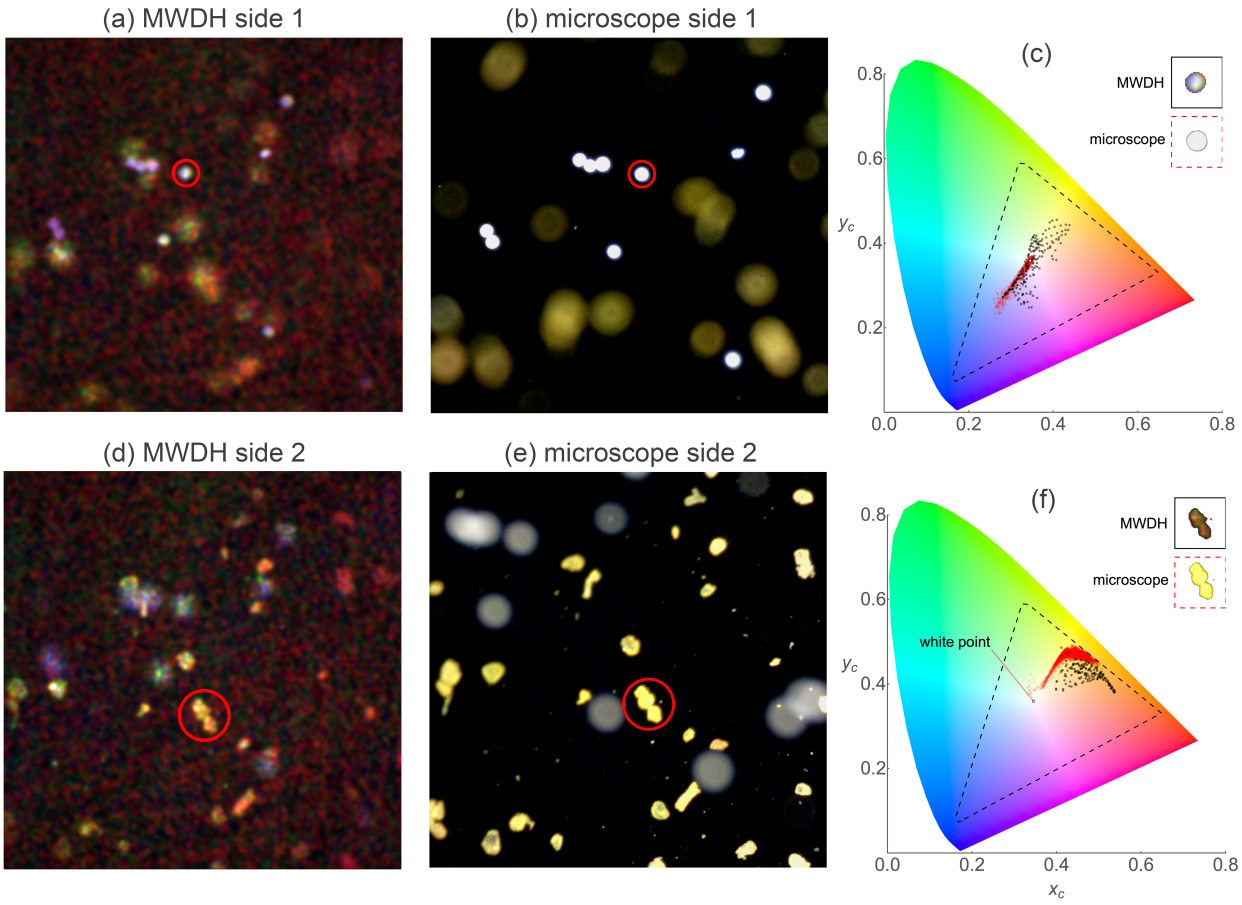


Figure 4.9: Volumetric discrimination of particles by color with backscatter MWDH. White micro-spheres 50 μm in diameter are deposited on side 1 of the window in Fig. 4.5 and yellow chalk-dust particles are deposited on the other side, side 2. The particles are thus separated by 2 mm along the axial direction, i.e., the z-axis. In (a) is the image resulting from the backscattered color hologram where the focus distance in (4.3) is selected to bring this side into focus. White particles are evident, one of which is outlined in red. In (b) is shown the microscope image of the same region of the window, again focused (manually) to bring side 1 into focus. Chromaticity analysis is applied in (c) to the particle in the red outline in (a) and (b). In (d)-(f), the same analysis is applied to side 2 where the chalk particles reside.

methods are also applied. Then, the particles on each side are imaged with the microscope. In Fig. 4.9, the first row considers the white particle on side 1 with Fig. 4.9(a) showing the MWDH image, Fig. 4.9(b) the microscope image, and in Fig. 4.9(c) is a chromaticity plot of the image pixels for the particle inside the red outline in the two images. The second row in Fig. 4.9 shows the same analysis for the chalk particles on side 2. Comparison of the MWDH-image quality to that in Fig. 4.7 shows a degree of degraded quality, which is

attributed to the increased speckle noise due to the greater concentration of particles used and the greater degree of particle-surface roughness of the chalk. Nevertheless, comparison of the MWDH and microscope images in Fig. 4.9 shows that holography is able to render both the morphology and color of the particles well enough that they can be associated unambiguously with the corresponding microscope images.

Examination of the chromaticity plots in Fig. 4.9 reveals that white particles are clearly differentiable from the yellow chalk and the MWDH colors are close to those rendered by the microscope. Perhaps as important is the spatial color resolution. While Fig. 4.7(a) shows that particles of different color are resolved for neighboring particles less than 50 μm apart in the lateral directions, i.e. x and y-axes, here one sees that different colors are also differentiated well along the axial direction. That is, the yellow particles in Fig. 4.9(d) on side 2 do not prevent the rendering of a mostly white particle on side 1. Of course, if yellow and white particles were to be at the same lateral location on sides 1 and 2, then it would be unlikely that this degree of color separation would be seen as the images would overlap. As a final note, Figs. 4.9(d) and (e) demonstrate that nonspherical particles are rendered well in terms of size and shape with MWDH, at least for particles of this size (approximately 50 μm).

4.7 Discussion

This work has demonstrated the feasibility of imaging individual particles approximately 50 µm in size and in color over a three-dimensional volume from a single backscatterd color hologram. The significance of this demonstration lies in the fact that most applications of color digital holography consider far larger objects and that given the comparatively small size of the particles here, the backscattered light is orders of magnitude weaker than related demonstrations. Because of the backscatter nature of the measurements, speckle noise is most pronounced and it significantly impacts efforts to white balance the images. However, we emphasize, again, that the objective is not to develop the most perfect color image of particles, but rather to have enough color resolution in an image to discriminate particles

of substantially different color. This is achieved via chromaticity analysis, see Sec. 4.5. The unique ability of digital holography to bring particles at different axial positions into focus after the fact has useful applications. These would include imaging moving particles, such as aerosols, and the development of instruments capable of imaging particles in a contact free manner without the need to move optical elements. Our work adds color to these abilities and a method to distinguish particles of different color in a quantitative, objective manner.

Chapter 5

The Color of Aerosols

The following work uses MWDH to generate a color image of aerosol microparticles. Three different pulsed lasers are combined to produce white light. In addition, a Mach-Zehender interferometer is used to interfere the backscattered light from the freely flowing aerosol and the reference beam. A prism CMOS sensor captures the interference patterns. A trigger system is built to monitor the events that activates when particles enter the sensing region. A digital delay generator is used to adjust lasers' and the sensor's latency. Further, the Fresnel diffraction theory is used on the three holograms (R, G, and B) separated from the sensor's color hologram. The monochrome images obtained from each hologram are then combined to produce a color image by using a color additive approach. For color calibration, different colored polyethylene microspheres are used. A few minerals of various colors are aerosolized and chromaticity analysis is applied to the color images to demonstrate the ability of the MWDH approach to quantitatively characterize aerosol particles of different colors, shapes, and sizes.

5.1 Introduction

The primary interest in this work is the determination of the morphology of a coarse-mode aerosol particle (CMA) *in situ*. CMAs are global atmospheric aerosols that have an impact

even thousands of miles away from their origins. The size range of CMA particles is approximately > 2 um or larger [126, 166] and is widespread in agricultural fields, deserts, and urban areas [33, 167]. Such particles are complicated not only in terms of morphology but also in terms of refractive indices. Calculating the refractive index is important during modeling, as it influences the reflection and absorption of the particle to sunlight [19]. Remote sensing is typically used to estimate the refractive index of the material, although this is not precise in general. In this situation, an accurate characterization of aerosol particles is critical for modeling aerosols to understand their impacts better, but it is not an easy task. Numerous studies have been conducted on the characterization of aerosol particles, for example, characterization by using atomic force microscopy, X-ray microscopy, etc. [168–170], and some studies use the optical trapping techniques; see [37]. However, these studies have been performed by collecting samples in the field and taking them to the laboratory for analysis. To properly assess the sample, it must be handled and transported without causing any distortion of the morphology and chemical properties. To address such problem, one should devise a novel method that is collection-free and capable of working in the actual aerosol environment using a portable platform like [111].

As already explained, light scattering is a tried and tested method to assess angle-resolved light scattering measurements related to aerosol particle size and shape [171–173]. However, inferring particle morphology from scattering patterns of complex-structured particles is frequently problematic because there is no acceptable way to accomplish this association. As an alternative, a new measurement strategy based on an accurate morphology characterization is needed rather than presumptions. Imaging with MWDH becomes an excellent way to characterize aerosols. In addition to being an excellent method for free-flowing imaging of aerosols, MWDH can also be beneficial for a wide range of other purposes, particularly in the fields of atmospheric and climate science, as well as industry, health, and agriculture.

The following study provides an innovative optical experiment method in which aerosolized CMA particles are imaged using a MWDH approach. This research aims to develop a novel sensing mechanism capable of characterizing individual CMA particles on the basis of their structure, size, and color. Previous experiments in DH have used a single wavelength laser

to produce holograms based on particle transmission or reflectance properties for the given wavelength, a grayscale image is generated [174]. The multiwavelength approach used in this work can produce a color image of aerosols that helps differentiate them based on their color properties. MWDH itself is not new, but the novelty of this work is the application of color DH to characterize free-flowing aerosols at the micrometer level. In addition, aerosol color images are also analyzed using a color-metric technique called chromaticity analysis. This analysis quantifies the color content in the image regardless of the apparent brightness of the color.

5.1.1 Optical arrangement

A back scatterer digital holography experiment for color imaging of aerosol particles is shown in Fig. 5.1. Choosing suitable lasers is fundamental to produce good color images from holography. Color holography requires at least three lasers with different wavelength. A typical white beam that is utilized to illuminate the particle is created by combining the spatially filtered and expanded laser beams. A color hologram is created using the backscattered light from the freely-flowing particles that successively interfered with a reference beam. In this experiment, three primary color lasers are used: the red (QL-656-100 Crysta laser) with a wavelength of 656.5 nm and maximum pulse energy of 15 uJ, the Q-switched Nd:YLF, the second-harmonic green laser (dc-50-527, Nd:YlF) with a wavelength of 526.5 nm and maximum pulse energy of 1 mj, and the blue (QL-440-50 Crysta laser) with a wavelength of 440 nm and maximum pulse energy of 10 uJ. The red and blue lasers are horizontally polarized, and green is vertically polarized. To adjust the polarization state of the lasers, a half-wave plate is mounted on a rotating mount and placed in front of each laser. The polarized beams are then aligned parallel to the optical table using the beam waking technique by two flat mirrors. The aligned beams are then cleaned and expanded to a diameter of (∼5mm) using a spatial filtering method. The first planoconvex lens (e.g., PCL1) focuses the beam. A pinhole removes any artifacts present by passing only the focused beam. Finally, the expanding beam from the pinhole is collimated by a second planoconvex lens (e.g., PCL2). Here, the

pinhole and PCL2 focal length selection determine the beam size after collimation. Attention is paid to selecting the second lens to ensure that the size of the laser beams is approximately equal. The reason behind to choose a Planoconvex lens is that, it works best for focusing parallel rays into a single point with a minimum aberrations. Following collimation, two dichroic mirrors, DCM1 and DCM2 combine laser beams and produce almost a white beam. More detail about these dichroic mirrors is explained in section 3.2.

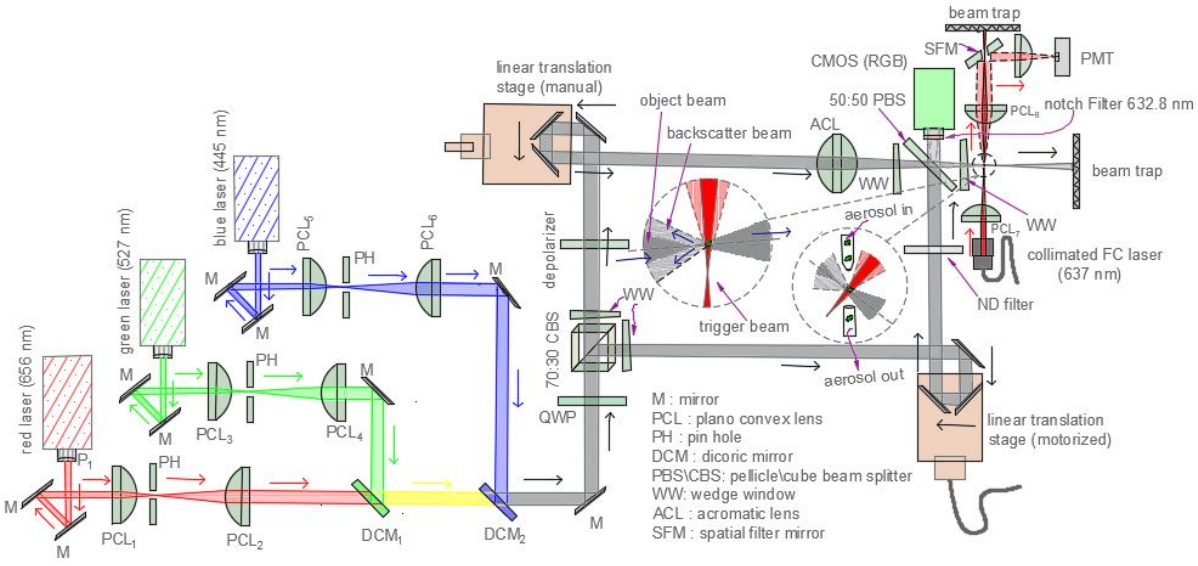


Figure 5.1: Optical arrangement of MWDH for free-flowing aerosol particles. Three pulsed lasers of wavelength $\lambda_r = 656$ nm, $\lambda_g = 527$ nm, and $\lambda_b = 440$ nm are combined by two dichroic mirrors (DCM) to produce a white beam. A cube beam splitter is used to split the beam in a 70:30 ratio. Then, two delayed stages (DS) are used to fold the beams and adjust the distance to manage the path lengths so that the backscattered light from the particles interferes well with the reference beam. In a trigger system, when particles reached the sensing region, the trigger beam is scattered and collected by a PMT. The PMT then activates the three lasers and the sensor to capture the color hologram of the particles.

The white beam is then circularly polarized by an achromatic quarter wave plate (QWP), then divided into two perpendicular beam using a cubic beam splitter (CBS) with a transmission-reflection ratio of 70:30. The beam transmitted by the CBS, the object beam (OB), is directed at aerosol particles, whereas the reflected beam is later used as the reference beam (RB) during interference. The pulsed lasers used here are low in coherence length, and the

blue laser has the lowest among three, i.e, less than a millimeter. The coherence length is calculated by measuring the spectral width of the pulse by a spectrometer. Therefore, matching the path lengths between OB and RB is particularly important to observe a good interference between them. Two delayed stages (DS) are used to fold the beams and adjust the distances to manage the path lengths so that the backscattered light from the particles interferes well enough with the reference beam. To calibrate the delay stages, a bare glass fiber is placed where the aerosol stream would otherwise flow in the sensing region, which is explained more in section 5.1.2. To make things simple, DS on RB is kept fixed after the path of the two arms become roughly equal. After, the path length of RB is gradually change for fine tuning through a motorized linear translation stage until the contrast interference is observed.

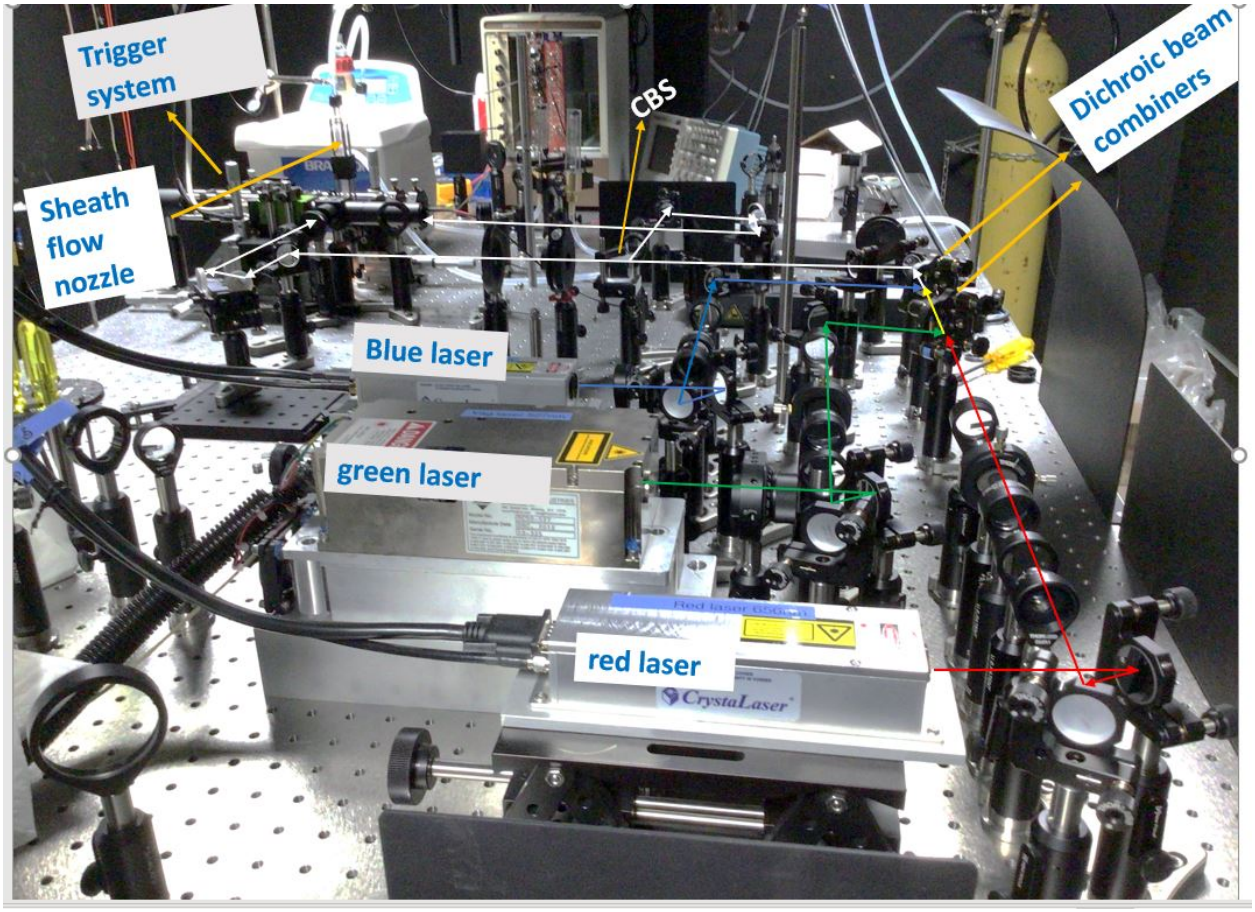


Figure 5.2: MWDH laboratory arrangement for free-flowing aerosol particles on an optical table.

Following the OB folded by the DS is focused by an achromatic lens (ACL) on a waist through a pellicle beam splitter (PBS) that has 45% reflection and 55% transmission (Thorlabs: BP145B1). There is significant amount of stray light originating from multiple reflection between the various optical surface even though they are coated with an antireflection coating. The augmented back-reflections from all optical surfaces is strong enough to saturate the sensor. Therefore, to prevent the back-reflected light from reaching the sensor, wedge windows are used in multiple places, as shown in Fig. 5.1. The wedge surface of the window deviates the back reflections out of the optical axis. Now, the converging OB that is transmitted from the PBS and focused and diverged as it moved toward the sensing region along the y direction. By converging the OB to a waist near the particle, the intensity is significantly increase and thus the backscattered light from the particle is also more intense. Once the particles are illuminated, a small amount of light is scattered back on the negative y-axis. PBS subsequently reflects it towards the sensor along the x-axis. A beam trap eliminates the portion of the beam that passes unscattered along the y-axis. To prevent the sensor from being overexposed by RB, the intensity of RB is reduced with a neutral density filter (ND= 0.5). When the particle arrives in the sensing region, the scattered trigger beam might also influence the sensor. A notch filter (Semrock: NF03-633E-25) is placed in front of the sensor to block scattered trigger light from entering the sensor. The weak intensity backscattered light from the particle interferes with the RB, and the sensor records the interference.

5.1.2 Trigger and electronics system

The trigger and electronic system is similar to that is explained in Chapter 3. When the particles reach the sensing volume, the trigger beam is scattered. The PMT collects the scattered light through a series of optical components. The PMT signal is passed through a series of electronic components and then used to trigger the lasers and the sensor as explained in section 3.2. A band pass filter (ThorLab: FL05635-10) is used in front of PMT to filter out all other wavelengths except 637 nm. The pulse durations of the lasers are set to 300 ns. The

delay between the laser and the sensor is adjusted appropriately for full pulse integration. For this, the sensor is set to activate approximately 350 ns before the laser pulses and shuts off after 350 ns when the pulse has finished its duration. The TTL pulse is sent to a digital

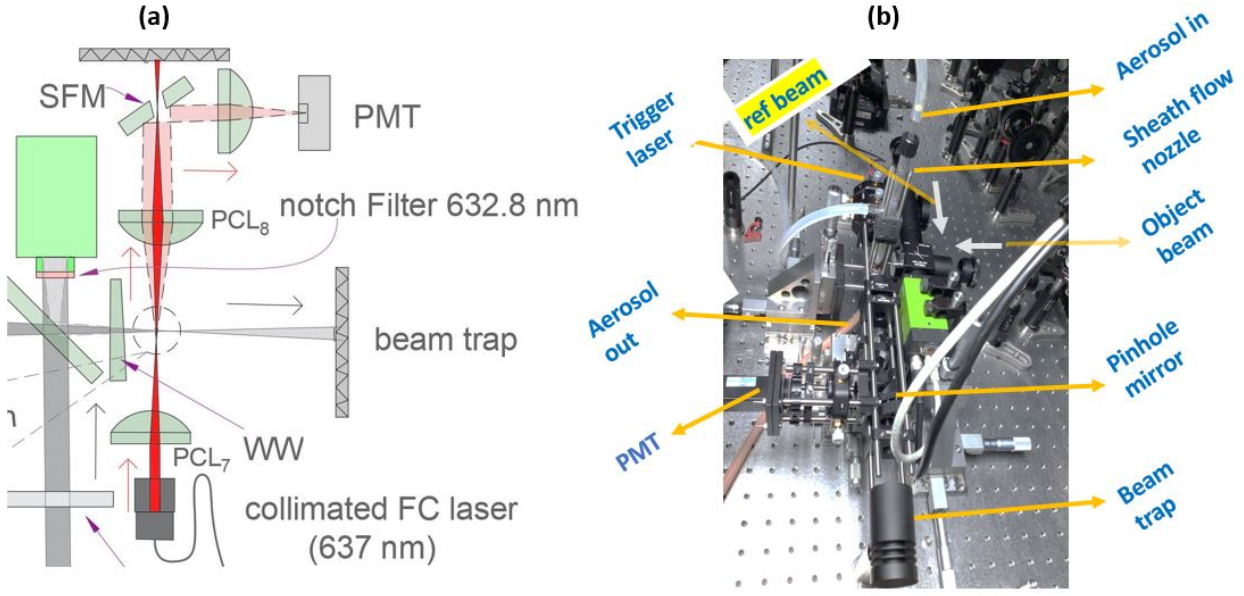


Figure 5.3: (a): The trigger system. When the particle arrives in the sensing zone, a collimated FC laser of wavelength $637nm$ is scattered. The scattered light is collected by the PMT while the unscattered light is eliminated through an SFM. The PMT signal is later used to activate the main three lasers and the sensor. (b): Picture of the trigger system of the actual laboratory arrangement.

delay generator to perform a delay on the lasers and the sensor. The delay generator then adjusts the duration of the laser pulses and the relative latency between the laser and the sensor. The measured relative latency of the sensor over the lasers is approximately 159 ns.

As mentioned above, pulse widths of DDG output signal for lasers are about 300 ns, and for the sensor, it is 1 us. These pulses are short enough for the particles to capture a hologram without blurring throughout the measurement at a flow rate of approximately 1m/s. Once the latency in lasers and the sensor have been appropriately addressed, an optical fiber is inserted into the sheath flow nozzle through which aerosols will flow later. Using a bare glass fiber inserted into the properly mounted sheath flow nozzle. This helps to adjust the delay stages until a backscatter hologram of the stationary fiber appears on the sensor and also assists to align the OB, RB, and the trigger beam. The sheath flow nozzle system and

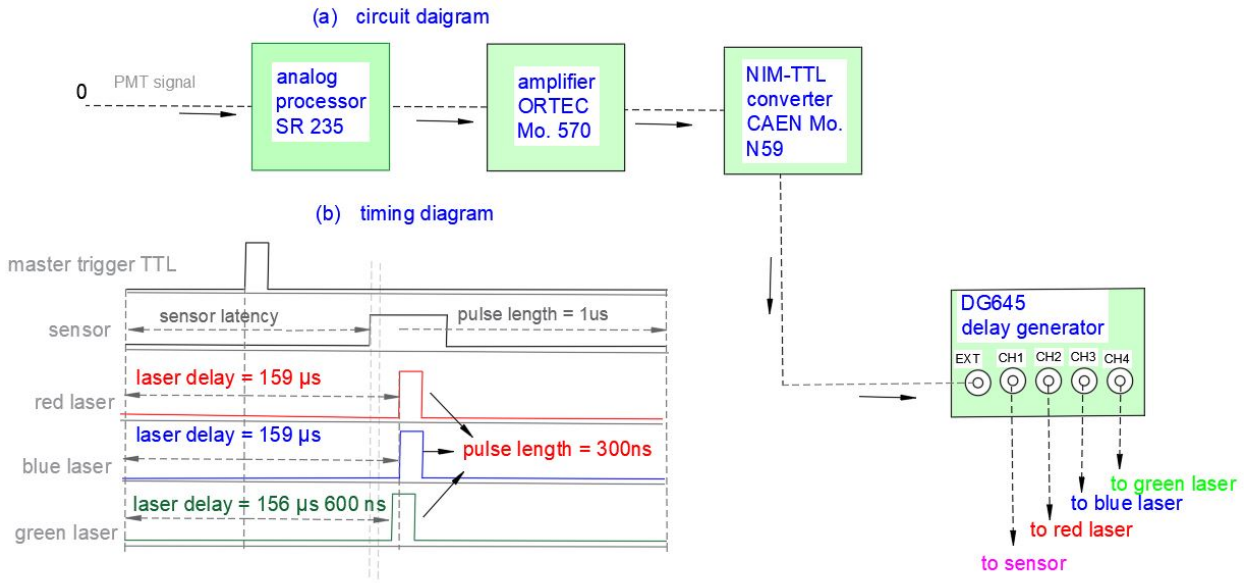


Figure 5.4: Electronic circuit diagram to rectify PMT signals. An analog processor converts the scattered trigger beam from aerosol particles received by a PMT to a sharp positive edge. Then the signal is amplified 1000 times by an amplifier.The amplifying signal is converted to TTL by the NIM-TTL converter. The TTL signal acts as an external trigger for the digital delay generator, causing the delivery of signals to lasers and sensors to delay to compensate for the relative latency between lasers and the sensor.

the entire trigger unit are mounted on two separate XYZ translation stages and adjusted to allow trigger and object beams to pass through the fiber and keep the fiber roughly in the center of the beams.

5.1.3 Sample collection and preparation

Suitable sample materials that are typical and similar to atmospheric particles are needed for laboratory research to study the characteristics of aerosols. Most of the dust in the atmosphere is made up of different types of minerals. This study used four different colored standard spherical particles and a wide range of different minerals for the analysis. For calibration, various standard color spheres are purchased from a commercial vendor (Cospheric LLC). The particles are in size range of 45-53 um. The selected calibration particles are opaque white particles (WPMS-1.00 C-5g) made of titanium dioxide (TiO2), red polyethylene (REDPMS-0.98 45-53um-5g), green polyethylene (GPMS-0.98 45-53um-5g), and blue/-

cyan polyethylene microspheres (BLPMS-1.00 45-53um-5g). The minerals are received from the Department of Geology at Kansas State University and the road dust is collected in glass containers from neighboring agricultural fields. In the laboratory, the samples are pulverized with a mortar and pestle, and the powder is gently dried in a low-heat oven to evaporate the moisture. Dry powders are cascaded through a series of sieves to separate particles of sizes greater than 40 μm but smaller than 210 μm. The separated powder is then collected in glass vials and stored in a desiccator to keep it dry until it is aerosolized in the experiment.

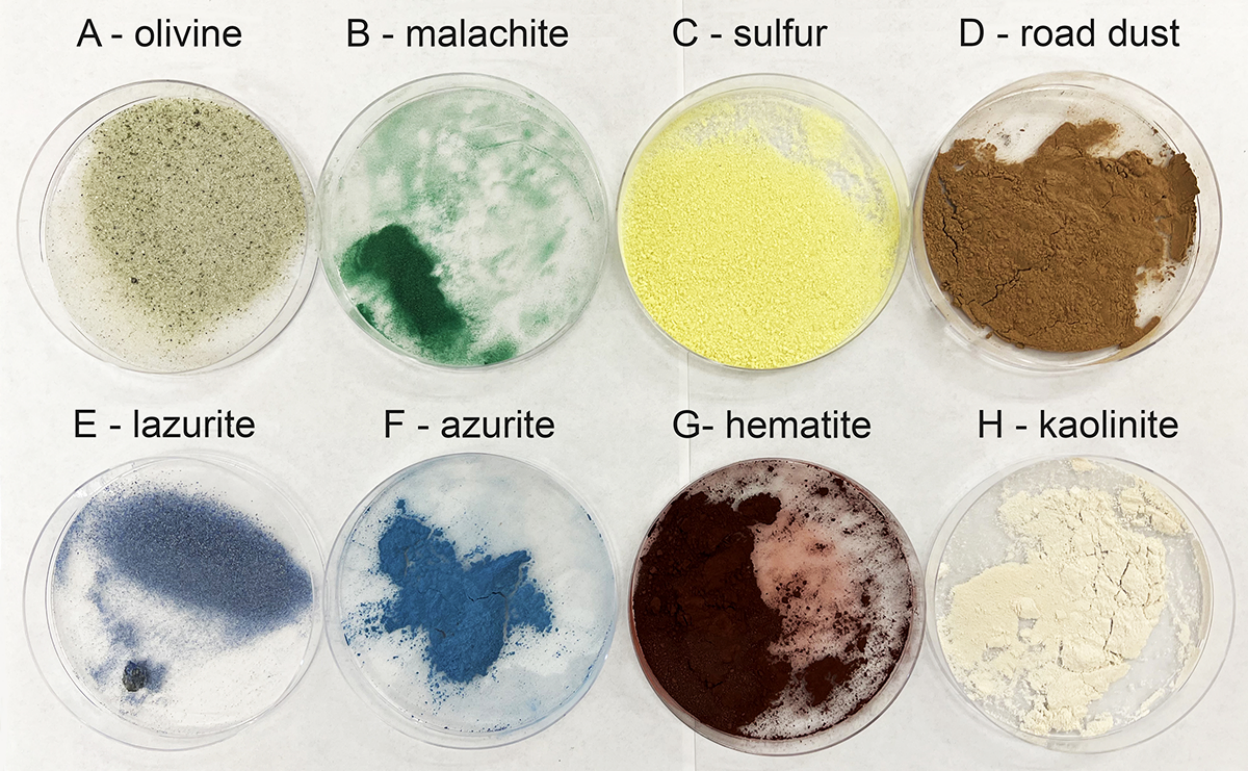


Figure 5.5: Picture of prepared mineral samples. The bulk of the minerals are pulverized using mortar and pestle and cascaded through series of sieves of different opening sizes.

5.1.4 Aerosol generation

An aerosol generator system is already explain in details in Chapter 3. The sheath flow nozzle delivers a stream-line flow of aerosols to the sensing volume, where a trigger system is continuously monitored for the event to occur. In this work, unlike the trigger system explained in section 3.2, the entire trigger system is constructed on a cage system. Mounting

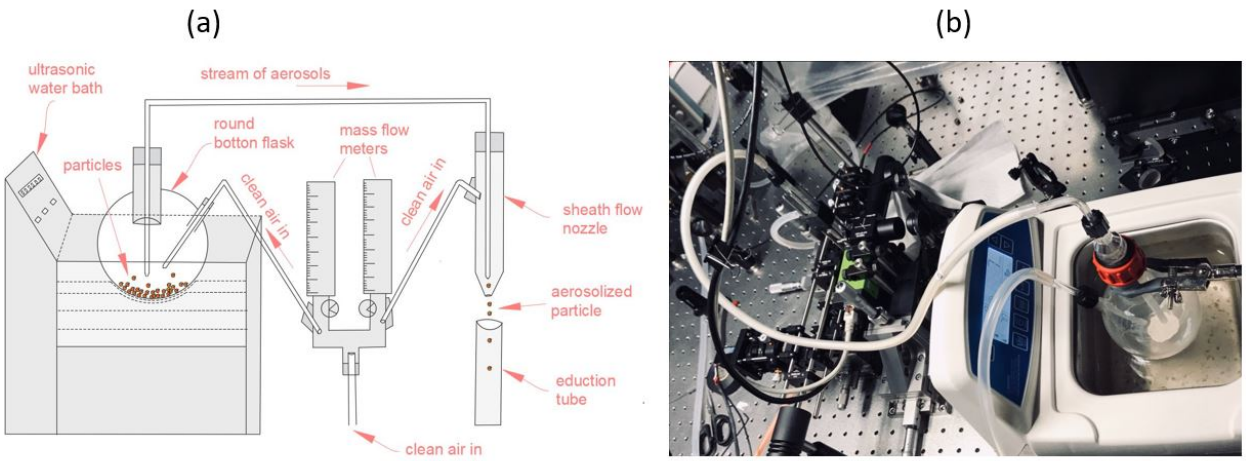


Figure 5.6: (a): Sketch of an aerosol particle generation system. Aerosols are produced by providing positive pressure to dried particles in a round flask. An ultrasonic water bath vibrates the sample to disintegrate the aggregations if present. A sheath air is used to circumvent the aerosol stream that exits the inner nozzle that controls the flow rate and the divergence angle of the flow while exiting the outer nozzle. (b): lab image of the aerosol system as described.

the system on a cage that can be translated by a XYZ translation stage helps to align the trigger beam in a precise manner. The trigger system consists of a fiber pigtails collimated CW laser of a wavelength of 637 nm. As shown in Figure 5.3(a), the trigger beam is perpendicular to the direction of the white beam, that is, along the y direction. As the particles come in contact, the trigger beam is scattered. A positive lens collimates scattered light from particles while focusing unscattered light on the waist. First, the focused beam is eliminated by a 500 µm pinhole mirror positioned at the waist at an angle of 45 degrees to the trigger beam's direction. Later, the collimated scattered light from the particles is converged by another positive lens to a photomultiplier tube (PMT). To prevent false triggering of the PMT, it is protected with a bandpass filter (Thorab: FLH05633-5), which blocks the stray lights.

5.1.5 Speckle reduction

Although the lasers used in this work are less in coherent length compared to the CW lasers used in our previous work in Chapter 4, speckle noise is always expected to be present in the

image. Speckle noise occurs when a coherent laser illuminates the rough surface of aerosol particles. The laser is randomly scattered with random phases, and when the phases interact with each other, they produce micro fringes. Subsequently, the micro fringes appeared in the image when the hologram is reconstructed as grain-like structures and randomly distributed across the images with significantly varying intensity. The size of these speckles can be statistically explained in terms of the physical parameter of the optical experiment as given by Eq. 4.4. Where $\Delta\eta$ is the mean size of a speckled grain,d is the focus distance while reconstructing the image from the hologram, λ_i is the wavelength of the laser, and Δx is the sensor pixel size.

Speckle noise reduction is one of the most studied topics in coherent digital holography. In our previous study in Chapter 4, the particles are on a glass window with the antireflection coating, and the speckle noise is reduced by averaging several images from the holograms produced by rotating a plane polarizer. A QWP is used to circularly polarize the input beam before passing through the plane polarizer which is install on a rotating mount. The details is explained in section 4.3.1. Inspired by our previous work, which shows that multiple polarization can reduce the speckle in the image. However for moving particles, it is not possible to capture multiple images with different polarization of the reference beam. For this an optical component is required that can produce the spatial polarization with in the beam. To incorporate this problem, a depolarizer (Thorlabs, DPP25-A) is used to produce a spatial periodicity on the input beam's polarization (or pseudorandom polarization). The depolarizer prevents the micro fringe formation and reduces the coherent interference of the backscattered light because light with different polarization interferes less.

The depolarizer technique is effective to some extent but does not entirely remove the speckle effect. As a result, there is still a significant amount of speckles present in the image. Furthermore, the speckle is minimized by implying a Gaussian convolution over $|K|^2$ in Eq. (4.3) with a two-dimensional Gaussian kernel G to generate a despeckled image $|K^{'}|$ as in Eq. (4.6). The Gaussian kernel is given by Eq. (4.7). The Gaussian convolution method is beneficial for reducing the speckle effect on the image; however, the uniform blurring also reduces the resolution. In Eq. (4.7), $\sigma^2 = (\alpha\eta_i)^2$ is the variance of the value of pixels in

a particular image channel. Here, the value α controls the amount of blur in that color channel. In this work, the value of α is 10; that is, the convolution that is considered ten neighborhood speckle grains in the calculation. The best image resolution that can be achieved in this study is effectively set by the value of η_i , which range approximately 16 to 30 μm in this work. This explains why the resolution is lower than that of forward-scatter DH images of comparable aerosol particles obtained using equivalent optical systems in Chapter 3.

5.1.6 Chromaticity analysis

Color perception in human vision is arbitrary [175]. Characterization of aerosols in terms of color requires a sophisticated method that eliminates bias and able to analyzes the colors of an image in quantitative manner. Many studies have been conducted on colorimetry, color science, color perception, and other color metrology, see [175–177]. The originality of this study is that it quantifies the color of the image using a technique known as chromaticity analysis (CA). The advantage of using CA is that it can objectively measure the colors and describe them in an image corresponding to how humans perceive color. The visible spectrum ranges from deep blue (380 nm) to red light (700 nm). To sense the visible colors, the human vision system utilizes three types of color receptors or cones. Different wavelengths of visible light cause the cones to respond differently. When receiving light reflected from objects, cones can detect primary colors in red, green, or blue. Any color other than primary colors can be detected simply by mixing the three primaries. The concept of rendering the image in this way is known as trichromacy [178].

According to the tristimulus system, color is created using the contributions of three primary colors. It can be quantified in coordinate values of X, Y, and Z that represent the sensitivity of the cones and visually matched under normal conditions. The tristimulus values are the three-dimensional vectors in the color space, where the length and direction represent the amount, i.e., luminance, and type of color, respectively. The value of chromaticity coordinates (x_c, y_c, z_c) is calculated by normalizing the tristimulus value by their

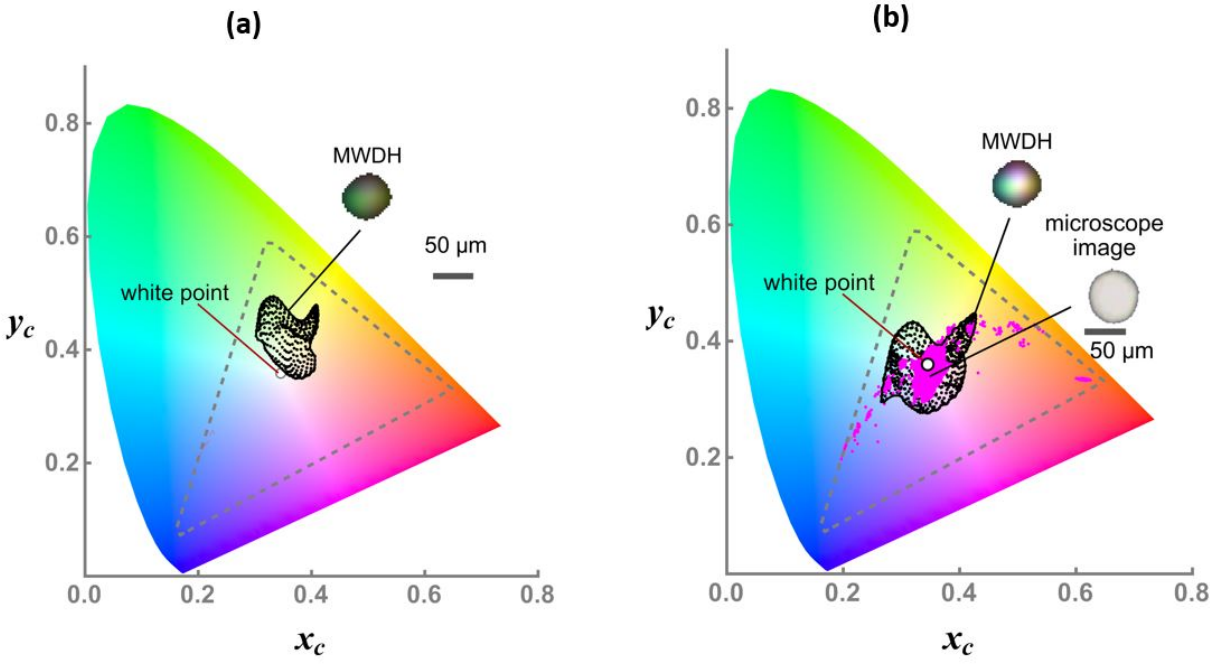


Figure 5.7: Chromaticity analysis of the image of white spheres obtained from MWDH before and after white balance. (a): CA of the image of white spheres 50 μm obtained from MWDH before WB. (b): CA of the image of the same particle after WB and CA of the optical microscope image plotted together in a chromaticity plot.

sum, which does not depend on the luminance, but only represents the colors. Transformation of the tristimulus value to the chromaticity coordinate has the benefit of examining the color contained in the image regardless of its brightness.

$$\begin{aligned} x_c &= \frac{X+Y+Z}{X}, \\ y_c &= \frac{X+Y+Z}{Y}, \\ z_c &= \frac{X+Y+Z}{Z} \end{aligned} \tag{5.1}$$

In the chromaticity plot shown in Fig. 5.7, two of the coordinates (x_c, y_c) are capable of representing any observable color as a single point on a two-dimensional graph. The third component, which represents the luminance, can be easily calculated using these coordinates, as they are normalized, that is, $x_c + y_c + z_c = 1$. If two colors are represented by two

points on a chromatic diagram, the color generated after mixing these two colors always lies in a straight line between these two points. Any set of three colors defines a triangular region in the chromaticity diagram. The chromaticity coordinate specifies the corners for that particular color. Any color falling into this triangle combines the three colors with a different proportion. Such a triangular region is commonly called a color space. A white point is a unique location on the chromaticity plot where the three primaries mix equally. The white point (WP) on the chromaticity plot is essential because it allows one to gauge how saturated the colors are in the image. The saturation measures the purity of color in the image. The saturation is independent of the brightness of the image. Darker images can also have a high color saturation. The saturation label can be measured by drawing a line from the white point to the border of the chromaticity plot. As one moves away from the WP towards the edge of the diagram along the line, the image has increased saturation in that particular color. For example, if the chromaticity distribution of an image falls close to the white point, the image will be less saturated; however, if the distribution is located farther from the white point and closest to the border, the image will be more saturated in that particular color signature.

Color Space in Chromaticity Diagram

Chrominance is a term that defines the hues, and the saturation of a color can be quantified by chromaticity analysis. The chromaticity diagram represents the chrominance of a color independent of the image's luminescence (brightness). Various CCD sensors have different spectral sensitivity and introduce different responses to RGB values [179, 180]. This variation caused an ambiguity in the color representation. To account for this device-dependent color production, a standard model is required that correlates the device's RGB signals to the CIE color matching function. One such model is the standard RGB (sRGB) color space model implemented in many sensors and digital media, including the sensor used in this experiment. sRGB is an international color standard defined by the International Electrotechnical Commission (IEC) [181]. This color space is standard and adapted by many display devices

and applications, such as JASC Paintshop, Photoshop, Microsoft windows, and many others [182]. However, the color-gamut covers a smaller area in the chromaticity diagram. As R = (0.64,0.33), G = (0.30,0.60), B = (0.15,0.06) are the corner points of the sRGB color space and forms a triangle in the chromaticity diagram, see dotted triangular region in Fig. 5.7. The device with sRGB color space can only produces the colors that covers by this color space [182, 183].

5.1.7 White balance

After dealing with speckles in the images, white balance (WB) became a fundamental challenge when multiple single-color (holographic) images are combined to reproduce the full-color image. Most importantly, it is evident that lasers with unequal power yield inaccurate color in the image of the particle in MWDH. Human eyes have color constancy, allowing them to adjust to various lighting conditions, whereas digital sensors lack this feature. The purpose of white balance is to produce an image that appears to have been captured in a white-light environment. To represent the accurate proportion of primary red, green, and blue colors in the final image one need to perform a WB on the image in MWDH. This should be done in a way that the image roughly represents the particle's natural color in white light illumination. Here, we utilize a simple white-balance technique to account for the unequal power of the lasers. The WB can also be done as exercised in section 4.3.2. The fundamental idea of simple WB in both works is that an image of a calibrated white object is considered white balanced when the pixel values of each channel must induce equal camera responses i.e, the value of RGB should be (c, c, c), where c ranges from 0 to 1. However, in this work we set the value of RGB value to the maximum camera responses , i.e, $(1, 1, 1)$ In other words, the white balance images should have normalized pixels, that is, R / Rmax, G / Gmax, and B / Bmax [184]. By doing so, one can achieve a vibrant image possible. In this context of WB, white spheres of known size and color are aerosolized as a proxy. The white spheres (Cospheric LLC, WPMS–1.00 45–53 µm–5 g) are nonfluorescent and range from 45-53 µm in diameter. These spheres are chosen because their reflectance functions are

consistent over a wide range of wavelengths, and white surface of the spheres scatters $\sim 99\%$ of light incident over it. The WB is followed by despeckling the reconstructed image of each channel by normalizing, where the brightest pixels value of the array becomes 1 and darkest pixel becomes 0. The normalization factors of white sphere of each channels are taken as references and will be applied to the pixel value of the respective color channel for all other color images later.

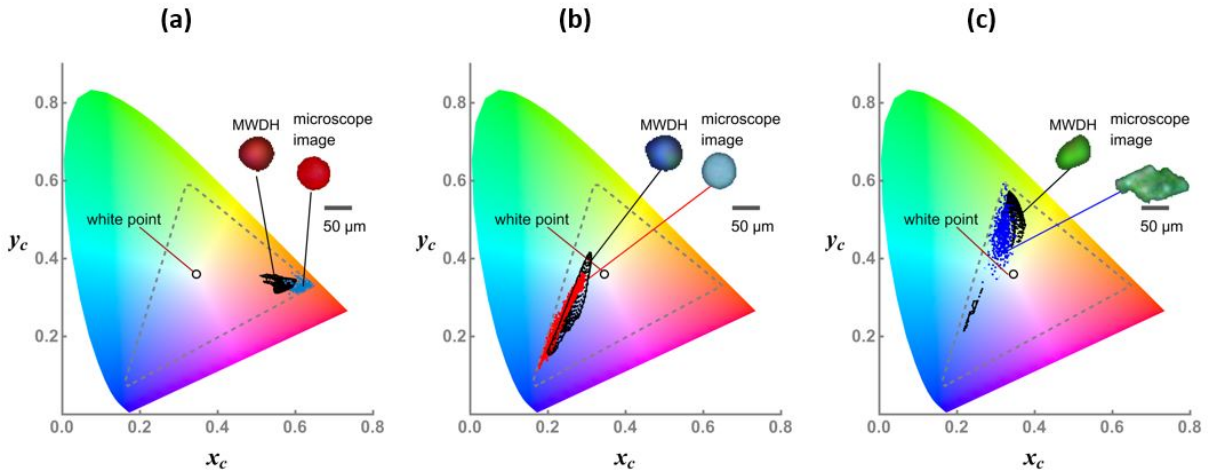


Figure 5.8: Chromaticity analysis of aerosolized color micro-spheres and non-spherical malachite mineral dust image from MWDH along with the corresponding white light optical microscope image is shown. (a,b) CA of the image of aerosolized $45 - 53$ μm red and cyan microspheres obtained from MWDH and the image of the same spheres using a white-light microscope. (c) CA of the image of the malachite mineral obtained from MWDH and the image obtained from the microscope.

Figure 5.7 shows the effectiveness of the white balance in the image of white particles (holography). One can observe that before white balance, the image is more greenish; however, the WB shifted the pixel value of each channel so that the combined pixel value in the final images falls around the white point in the chromaticity plot. The distribution of the points keeps the white point in the middle, indicating that the image is white, but it still contains the speckle noise that shifted a few pixels slightly away from the white point.

To further highlight the effectiveness of the speckle noise reduction and the white balancing approach, several primary color particles are used, including red spheres (Cospheric LLC, RPMS-0.98), green spheres (Cospheric LLC, GPMS-0.98), and blue/cyan spheres (Cospheric

LLC, BPMS-1.00 45-53 m). In Fig. 5.8, the chromaticity plot of these color spheres acquired with holography is shown, and the color representation is compared to the chromaticity of the color microscopic images. Figures 5.7 and 5.8 show many key characteristics of MWDH. The MWDH approach produced color images using weak backscattering light from the microparticles. This approach can image a wide range of color particles with significant color accuracy with several wavelengths (R, G, and B) in the visible spectrum. Although forward-scattering and digital backscattering holography have been studied in several publications to characterize such small-scale particles, this is a first for multiwavelength digital holography in aerosol particles. More importantly, for a glass sphere with a 50 μm diameter illuminated by the light of $\lambda = 633$ nm, the forward scattering light is four orders of magnitude greater than the backward scattering intensity [185]. The color image produced after partial speckle reduction and WB in Figures 5.7 and 5.8 provides the particle size and shape, in addition to the fair accuracy of the color rendition. The Fig. 5.7(b) shows wider distribution of points around the white point, which limits a real uniform white appearance as would appear under a microscope, indicating that the color rendition, in this case, is not optimal. The speckles in the image are wavelength-dependent, and the despeckled approach used in this work cannot eradicate the effect. However, one can practice more sophisticated speckle methods, see [147–149].

5.2 Results

When light is incident on a material, some photons bounce off the surface, some pass through it, and others are absorbed. Light scattering or absorption might depends on the elemental composition of the materials. Different in composition have different ability to absorb or scatter light. For example, hematite looks red because it scatters red light and absorbs the rest of the visible colors contained in incident light. In contrast, olivine looks green because it absorbs all of the other colors except the green color. Since modern sensors and computer technology have provided standardized color definitions, colors can be applied to identify materials. The color of any material is one of the key characteristics that make it possible to

identify its composition or type. It is a visual characteristic widely used to identify minerals in optical mineralogy . However, our objective in this study is not to precisely identify the composition of the material but rather to characterize aerosols according to their shape, size, and color. Chromatic analysis (CA), as discussed above, is used to quantify the color of an aerosol. CA is a relevant way to analyze the color contained in an image, as it replicates the spectral reflections from a surface of the material based on the RGB sensitivity of the human eye. The quantifiable feature of CA allows one to differentiate between two colors, as each coordinate on CA represents a unique color. Then, it is evident that particles made of different materials might have different distribution points on the chromaticity diagram and, therefore, be able to differentiate from one another without further measurements. When the chromaticity signatures of different aerosols are compared, it is possible to identify the different aerosols. The DH used in this work can access not only the shape and size of the particle but also its color. In this case, the color offers an additional characterization that aid in identifying aerosols. For example, minerals' morphology and color differ from those of pollen, bioaerosols, etc.

Measurements are made on various minerals to verify the objective of discriminating particles based on their shape, size, and color. Since mineral dust (MD) is a significant and widespread atmospheric CMA component, this study may be useful for many other atmospheric investigations.

During the experiment, the mineral dust samples except the road dust are generated by pulverizing rock samples provided by the Department of Geology, Kansas State University (KSU). As stated in the section 5.1.3, collected particles in a particular size range are aerosolized and digital holograms are recorded. The colors of the minerals are analyzed through CA using their holographic color images shown in Fig. 5.9. During CA, the black background of each image is removed, leaving only the particle image for evaluation. Although not required, cropping the images reduces the noise that the background adds to the chromaticity plot. Each black point in the CA distribution represents a color coordinate (x_c, y_c) of a pixel in the image. The distribution of these coordinates is called the particle's chromaticity signature, which represents the overall color of the particle. The distribution of

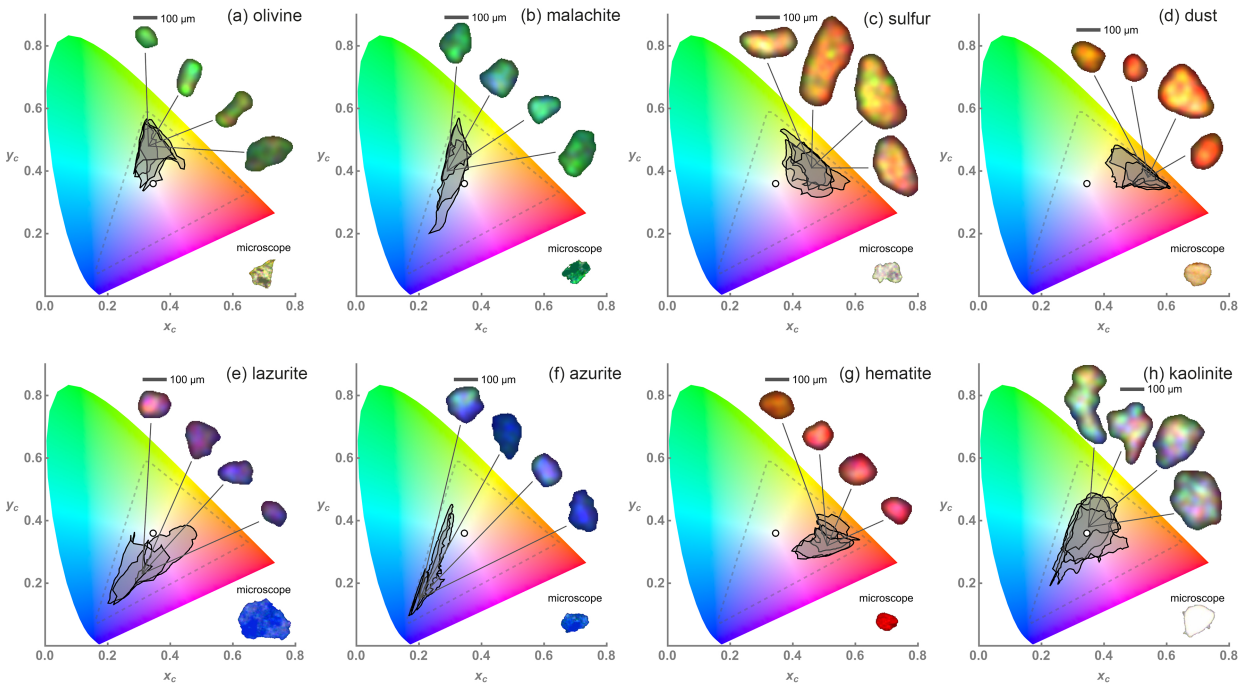


Figure 5.9: Chromaticity analysis of a variety of free-flowing mineral dust aerosol particles is shown. Various mineral crystals are pulverized in the laboratory. The powder is aerosolized, and the holograms are recorded in MWDH. Each particle-image corresponds to a separate measurement. The images obtained are plotted in a chromaticity diagram. In the chromaticity plot, each black shaded region represents the particle's chromatic signature. The shown scale bar is of length 100 µm. Also, an optical microscope image of a typical particle obtained from the powder from which the aerosols are produced is shown in the bottom right corner of each panel.

points indicates the presence of a range of colors, which is confirmed by carefully examining the image. In the plot, while observing the area where most of the points occur for different minerals, it is clear that particles of various colors are distinct from each other. Although they have noticeably different brightness, particles have a similar chromaticity signature, highlighting one of the benefits of using CA. The reader should be aware that in images, for example, in Fig. 5.9 (a), the position of chromaticity signatures on the chromaticity plot is not significantly affected by the brightness of the color of the pixels in the images. In other words, the brightness variation contained in the corresponding image does not affect the distribution of pixel points in the chromaticity plot. However, the shifted-point distribution for the different particles Fig 5.9(a)-(h) clearly shows that the particles are noticeably different.

CA can show sufficient variation of the particles' spectral reflections (or absorption).

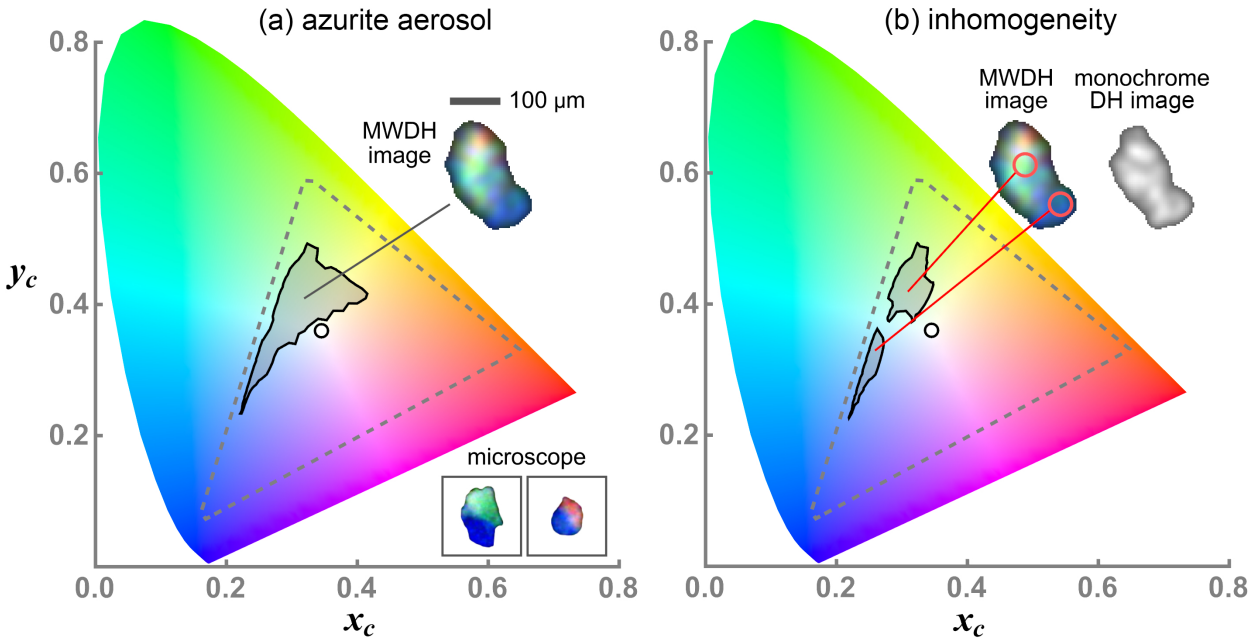


Figure 5.10: Material inhomogeneity inside a single mineral-dust aerosol particle is demonstrated. (a): The chromaticity signature of an azurite mineral obtained via MWDH is shown, showing both green and blue contributions. The particle exhibits discrete regions of green or blue that are noticeably bigger than the $\sim 30\mu$m speckle size in the MWDH image. Given that the particle is mostly made up of a green and blue mineral, indicates the particle is inhomogeneous. (b): The same aerosol particle is examined, but the chromaticity signature is only shown for the particle-image pixels located inside the circles indicated. Similar to the azurite particles in Fig. 5.9(F), the blue signature also appears in this region of the color space, while the malachite is most closely associated with the green characteristic as in Fig. 5.9(B). The second image in (b) shows a monochrome image produced by reconstructing the identical particle image using just λ_b. There isn't any obvious proof of the inhomogeneity in this image.

As explained above, each point on CA has a distinct color coordinate that allows it to differentiate particles with very close color differences. However, particles with almost white appearance and have low contribution to a particular color are hard to distinguish. In our study of MDs, they have sufficient visible color differences that can be easily differentiated in CA. But, sometimes, it can be challenging to tell whether two fundamentally different particle types belong to the same categories or not when their chromaticity signatures are almost identical. Fortunately, this limitation can also be overcome in MWDH since the hologram provides information on the shape and size of the particles along with the color. One type of aerosol may have a morphological character different from other types of particles. For

example, many pollen grains have a basic symmetry morphology, such as spherical, capsule, and bean-shaped shapes. However, most minerals exhibit significant irregularity in shape, sharp edges, and uneven surface profiles.

A sample of a particle with a consistent color signature or a particle with a homogeneous composition is shown in Figure 5.9. In this examination, holographic images of several types of aerosolized minerals are fed into the CA, generating distinct clusters of points in the chromaticity diagram for each mineral. The chromaticity signatures in the chromaticity diagram are distinct enough that one can visually identify their types and recognize the color of certain minerals both subjectively and quantitatively. For example, azurite appears blue, and there is a distinct cluster of points in the blue region of the diagram. The graphic 5.9 also reveals that minerals that are difficult to differentiate with the eyes can be quantified here by CA. Lazurite and azurite, for example, both appear deep blue in human eyes and are difficult to distinguish, yet they differ significantly in CA. In addition, particles sometimes have a heterogeneous composition. In other words, the particle is composed of two or more separate compositions. In this case, the particle has a color variation on its surface. The chromaticity signature for such a particle does not appear in a specific area of the CA but rather extends or covers a larger area of the chromaticity plot. As shown in Fig. 5.10(a), an image of azurite ore samples is produced using MWDH. The image of the particles clearly shows a heterogeneous color signature since one part of the particle image is bluish, and another part is greenish. The CA of such an image further verifies its heterogeneity in color. When all pixels in the image are considered, the chromaticity diagram displays the distribution of black points; see 5.10(a). Although it is clear from the image itself that the particle is heterogeneous, plotting the entire image in CA shows that the distribution of points covers a wide area. To identify the different contributions to this heterogeneity, different parts that show variations of colors in the same image are plotted in CA. Figure 5.10(b) shows the CA analysis of two different parts of the same particle image showing different chromaticity signatures, which provides proof of color inclusions. These examples present the ability to quantify the heterogeneous composition on a particle of such a micrometer-size level by MWDH that a monochrome DH image cannot.

In this study, a range of common minerals is taken into account and demonstrated the ability of MWDH to produce color images that are sufficiently distinguished in CA. In fact, without the ability to discriminate between distinct particles, CA would be of limited analytical use; it should provide regions of the chromaticity diagram that represent definite categories of minerals in our collection. Observing Figures 5.9 and 5.10, it is possible to distinguish different types of minerals based on their chromaticity signature along with various shapes and sizes.

Bibliography

[1] Paulo Artaxo and Hans-Christen Hansson. Size distribution of biogenic aerosol particles from the amazon basin. *Atmospheric Environment*, 29(3):393–402, 1995.

[2] A. McDonagh and M.A. Byrne. A study of the size distribution of aerosol particles resuspended from clothing surfaces. *Journal of Aerosol Science*, 75:94–103, 2014.

[3] Bradley J. Ingebrethsen, Stephen K. Cole, and Steven L. Alderman. Electronic cigarette aerosol particle size distribution measurements. *Inhalation Toxicology*, 24 (14):976–984, 2012.

[4] Panich Intra and Nakorn Tippayawong. An overview of aerosol particle sensors for size distribution measurement. *Maejo international journal of science and technology*, 1: 120–136, 2007.

[5] F. Gaudfrin, E. Santos, D. Presley, and M. J. Berg. Time-resolved imaging of settling mineral dust aerosols with digital holography. *OSA Continuum*, 3, 2020.

[6] Zhang Ren Jian, HO Kin Fai, and Shen Zhen Xing. The role of aerosol in climate change, the environment, and human health. *Atmospheric and oceanic science letters*, 5(2):156–161, 2012.

[7] Charles S Zender, R.L.R.L Miller, and Ina Tegen. Quantifying mineral dust mass budgets: Terminology, constraints, and current estimates. *Eos, Transactions American Geophysical Union*, 85(48):509–512, 2004.

[8] Gottfried Hänel. Influence of relative humidity on aerosol deposition by sedimentation. *Atmospheric Environment*, 16(11):2703–2706, 1982.

[9] Hongfei Xie, Junfang Zhao, Weixiong Yan, Xiangna Kong, and Huiwen Peng. Integrated remote sensing and crop model approach for impact assessment of aerosols on biomass accumulation of maize. *IEEE Journal of Selected Topics in Applied Earth Observations and Remote Sensing*, 14:7237–7245, 2021.

[10] Tianyi Zhang, Tao Li, Xu Yue, and Xiaoguang Yang. Impacts of aerosol pollutant mitigation on lowland rice yields in china. *Environmental Research Letters*, 12:104003, 2017.

[11] Kimberly A Prather. Our current understanding of the impact of aerosols on climate change. *Chemistry and Sustainability Energy and Materials*, 2:377–379, 2009.

[12] Henrik Grythe, Johan Ström, Radovan Krejci, P Quinn, and Andreas Stohl. A review of sea-spray aerosol source functions using a large global set of sea salt aerosol concentration measurements. *Atmospheric Chemistry and Physics*, 14:1277–1297, 2014.

[13] Ina Tegen and K Schepanski. The global distribution of mineral dust. In *IOP Conference Series: Earth and Environmental Science*, volume 7, page 012001. IOP Publishing, 2009.

[14] K Roberts, A Hathway, LA Fletcher, CB Beggs, MW Elliott, and PA Sleigh. Bioaerosol production on a respiratory ward. *Indoor and Built Environment*, 15:35–40, 2006.

[15] Peter F DeCarlo, Anita M Avery, and Michael S Waring. Thirdhand smoke uptake to aerosol particles in the indoor environment. *Science Advances*, 4:8368, 2018.

[16] TA Mather, DM Pyle, and C Oppenheimer. Tropospheric volcanic aerosol. *Geophysical Monograph-American Geophysical Union*, 139:189–212, 2003.

[17] Chul Eddy Chung, V Ramanathan, Dohyeong Kim, and IA Podgorny. Global anthropogenic aerosol direct forcing derived from satellite and ground-based observations. *Journal of Geophysical Research*, 110, 2005.

[18] Robert J Charlson, SE Schwartz, JM Hales, Ro D Cess, JA Coakley Jr, JE Hansen, and DJ Hofmann. Climate forcing by anthropogenic aerosols. *Science*, 255:423–430, 1992.

[19] Ying Zhang, Zhengqiang Li, Yuhuan Zhang, Donghui Li, Lili Qie, Huizheng Che, and Hua Xu. Estimation of aerosol complex refractive indices for both fine and coarse modes simultaneously based on aeronet remote sensing products. *Atmospheric Measurement Techniques*, 10:3203–3213, 2017.

[20] Walter John. Size distribution characteristics of aerosols. *Aerosol measurement*, 3: 41–54, 2011.

[21] Gregory R Carmichael, Bhupesh Adhikary, Sarika Kulkarni, Alessio D'Allura, Youhua Tang, David Streets, Qiang Zhang, Tami C Bond, Veerabhadran Ramanathan, Aditsuda Jamroensan, et al. Asian aerosols: current and year 2030 distributions and implications to human health and regional climate change. *Environmental science & technology*, 43:5811–5817, 2009.

[22] D Sharma, AK Srivastava, K Ram, A Singh, and D Singh. Temporal variability in aerosol characteristics and its radiative properties over patiala, northwestern part of india: Impact of agricultural biomass burning emissions. *Environmental Pollution*, 231:1030–1041, 2017.

[23] SG Yeatman, LJ Spokes, and TD Jickells. Comparisons of coarse-mode aerosol nitrate and ammonium at two polluted coastal sites. *Atmospheric Environment*, 35:1321–1335, 2001.

[24] Louis A Derry and Oliver A Chadwick. Contributions from earth's atmosphere to soil. *Elements*, 3:333–338, 2007.

[25] GP Ayers and JL Gras. Seasonal relationship between cloud condensation nuclei and aerosol methanesulphonate in marine air. *Nature*, 353(6347):834–835, 1991.

[26] Philipp Reutter, H Su, J Trentmann, Martin Simmel, Diana Rose, SS Gunthe, H Wernli, MO Andreae, and U Pöschl. Aerosol-and updraft-limited regimes of cloud droplet formation: influence of particle number, size and hygroscopicity on the activation of cloud condensation nuclei (ccn). *Atmospheric Chemistry and Physics*, 9(18): 7067–7080, 2009.

[27] Daniel A Knopf, Peter A Alpert, and Bingbing Wang. The role of organic aerosol in atmospheric ice nucleation: a review. *ACS Earth and Space Chemistry*, 2(3):168–202, 2018.

[28] KM Lau, KM Kim, YC Sud, and GK Walker. A gcm study of the response of the atmospheric water cycle of west africa and the atlantic to saharan dust radiative forcing. In *Annales Geophysicae*, volume 27, pages 4023–4037. Copernicus GmbH, 2009.

[29] Mitsuo Uematsu, Akifumi Yoshikawa, Hiroaki Muraki, Kimio Arao, and Itsushi Uno. Transport of mineral and anthropogenic aerosols during a kosa event over east asia. *Journal of Geophysical Research: Atmospheres*, 107:AAC–3, 2002.

[30] Lothar W Schutz, Joseph M Prospero, Patrick Buat-Ménard, Robert Harriss, Renato AC Carvalho, Neils Z Heidam, Antonio Cruzado, and Ruprecht Jaenicke. The long-range transport of mineral aerosols: group report. In *The long-range atmospheric transport of natural and contaminant substances*, pages 197–229. Springer, 1990.

[31] Irina N Sokolik and Owen B Toon. Direct radiative forcing by anthropogenic airborne mineral aerosols. *Nature*, 381(6584):681–683, 1996.

[32] Peter Knippertz and Martin C Todd. Mineral dust aerosols over the sahara: Meteorological controls on emission and transport and implications for modeling. *Reviews of Geophysics*, 50, 2012.

[33] Natalie Mahowald, Samuel Albani, Jasper F. Kok, Sebastian Engelstaeder, Rachel Scanza, Daniel S. Ward, and Mark G. Flanner. The size distribution of desert dust aerosols and its impact on the earth system. *Aeolian Research*, 15:53–71, 2014.

[34] Minghou Xu, Dunxi Yu, Hong Yao, Xiaowei Liu, and Yu Qiao. Coal combustion-generated aerosols: Formation and properties. *Proceedings of the Combustion Institute*, 33:1681–1697, 2011.

[35] DE Walton. The morphology of spray-dried particles a qualitative view. *Drying Technology*, 18:1943–1986, 2000.

[36] Lei Li, Zhengxu Huang, Junguo Dong, Mei Li, Wei Gao, Huiqing Nian, Zhong Fu, Guohua Zhang, Xinhui Bi, Ping Cheng, et al. Real time bipolar time-of-flight mass spectrometer for analyzing single aerosol particles. *International Journal of Mass Spectrometry*, 303:118–124, 2011.

[37] Aimable Kalume, Chuji Wang, and Yong-Le Pan. Optical-trapping laser techniques for characterizing airborne aerosol particles and its application in chemical aerosol study. *Micromachines*, 12:466, 2021.

[38] Alison Bain, Aidan Rafferty, and Thomas C Preston. Determining the size and refractive index of single aerosol particles using angular light scattering and mie resonances. *Journal of Quantitative Spectroscopy and Radiative Transfer*, 221:61–70, 2018.

[39] J Wang, P Guo, Xiaopeng Li, Jinying Zhu, T Reinert, J Heitmann, D Spemann, J Vogt, R-H Flagmeyer, and T Butz. Source identification of lead pollution in the atmosphere of shanghai city by analyzing single aerosol particles (sap). *Environmental science & technology*, 34:1900–1905, 2000.

[40] S Weber, P Hoffmann, J Ensling, AN Dedik, S Weinbruch, G Miehe, P Gütlich, and HM Ortner. Characterization of iron compounds from urban and rural aerosol sources. *Journal of Aerosol Science*, 31:987–997, 2000.

[41] AL Dye, MM Rhead, and CJ Trier. The quantitative morphology of roadside and background urban aerosol in plymouth, uk. *Atmospheric Environment*, 34:3139–3148, 2000.

[42] Anubha Agrawal, Vinay K Upadhyay, and Kamna Sachdeva. Study of aerosol behavior on the basis of morphological characteristics during festival events in india. *Atmospheric Environment*, 45:3640–3644, 2011.

[43] TL Barone, Evelyn Hesse, CE Seaman, AJ Baran, TW Beck, ML Harris, PA Jaques, T Lee, and SE Mischler. Calibration of the cloud and aerosol spectrometer for coal dust composition and morphology. *Advanced Powder Technology*, 30:1805–1814, 2019.

[44] RT Nishida, TJ Johnson, AM Boies, and Simone Hochgreb. Measuring aerosol active surface area by direct ultraviolet photoionization and charge capture in continuous flow. *Aerosol Science and Technology*, 53(12):1429–1440, 2019.

[45] Renyi Zhang, Alexei F Khalizov, Joakim Pagels, Dan Zhang, Huaxin Xue, and Peter H McMurry. Variability in morphology, hygroscopicity, and optical properties of soot aerosols during atmospheric processing. *Proceedings of the National Academy of Sciences*, 105:10291–10296, 2008.

[46] S.K. Sze, N. Siddique, J.J. Sloan, and R. Escribano. Raman spectroscopic characterization of carbonaceous aerosols. *Atmospheric Environment*, 35:561–568, 2001.

[47] Qi Jianhua, Li Xianguo, Feng Lijuan, and Zhang Manping. Characterization of dust and non-dust aerosols with sem/edx. *Journal of Ocean University of China*, 5:85–90, 2006.

[48] Charity Coury and Ann M. Dillner. ATR-FTIR characterization of organic functional groups and inorganic ions in ambient aerosols at a rural site. *Atmospheric Environment*, 43:940–948, 2009.

[49] E. Bontempi, A. Zacco, D. Benedetti, L. Borgese, P. Colombi, H. Stosnach, G. Finzi, P. Apostoli, P. Buttini, and L.E. Depero. Total reflection x-ray fluorescence (TXRF) for direct analysis of aerosol particle samples. *Environmental Technology*, 31:467–477, 2010.

[50] Maohua Pan, Tania S. Bonny, Julia Loeb, Xiao Jiang, John A. Lednicky, Arantzazu Eiguren-Fernandez, Susanne Hering, Z. Hugh Fan, and Chang-Yu Wu. Collection of viable aerosolized influenza virus and other respiratory viruses in a student health care center through water-based condensation growth. *mSphere*, 2:e00251–17, 2017.

[51] E.K. Bigg, A. Ono, and Judith A. Williams. Chemical tests for individual submicron aerosol particles. *Atmospheric Environment*, 8:1–13, 1974.

[52] Prakash Gautam, Justin B. Maughan, Jan Ilavsky, and Christopher M. Sorensen. Light scattering study of highly absorptive, non-fractal, hematite aggregates. *Journal of Quantitative Spectroscopy and Radiative Transfer*, 246:106919, 2020.

[53] Matthew J. Berg and Stephen Holler. Simultaneous holographic imaging and light-scattering pattern measurement of individual microparticles. *Opt. Lett.*, 41:3363–3366, 2016.

[54] Stephen Holler, Matthew J. Berg, Osku Kemppinen, and Yuli W. Heinson. Two-dimensional scattering and digital holography from isolated aerosol particles. In Abhijit Mahalanobis, Amit Ashok, Lei Tian, and Jonathan C. Petruccelli, editors, *Computational Imaging III*, volume 10669, pages 46 – 53. International Society for Optics and Photonics, SPIE, 2018.

[55] Prakash Gautam and Christopher M. Sorensen. A light-scattering study of highly refractive, irregularly shaped MoS_2 particles. *Journal of Quantitative Spectroscopy and Radiative Transfer*, 242:106757, 2020.

[56] C.F. Bohren and D.R. Huffman. *Absorption and Scattering of Light by Small Particles*. Wiley Science Series. Wiley, 2008.

[57] Dennis Gabor. Holography, 1948-1971. *Science*, 177:299–313, 1972.

[58] Emmett N. Leith and Juris Upatnieks. Reconstructed wavefronts and communication theory. *J. Opt. Soc. Am.*, 52(10):1123–1130, 1962.

[59] Emmett N. Leith and Juris Upatnieks. Wavefront reconstruction with continuous-tone objects. *J. Opt. Soc. Am.*, 53(12):1377–1381, 1963.

[60] D. Gabor and W. P. Goss. Interference microscope with total wavefront reconstruction. *J. Opt. Soc. Am.*, 56:849–858, 1966.

[61] D. Gabor. A new microscopic principle. *Nature*, 161:777–778, May 1948.

[62] Pierre Alexandre Blanche. *Inline Transmission Hologram (Gabor)*, pages 42–43. Society of Photo-Optical Instrumentation Engineers, 2014.

[63] Thomas Kreis. *Handbook of Holographic Interferometry: Optical and Digital Methods*. Wiley – VCH, 2006.

[64] Cameron Knox. Holographic microscopy as a technique for recording dynamic microscopic subjects. *Science*, 153:989–990, 1966.

[65] George E. Smith. The invention and early history of the ccd. *Nuclear Instruments and Methods in Physics Research Section A: Accelerators, Spectrometers, Detectors and Associated Equipment*, 607:1–6, 2009.

[66] George E. Smith. Nobel lecture: The invention and early history of the ccd. *Rev. Mod. Phys.*, 82:2307–2312, 2010.

[67] Noboru Shiono, Yoshimitsu Sakagawa, Masayuki Sekiguchi, Kenji Sato, Isao Sugai, Toshiyuki Hattori, and Yasuo Hirao. Single event effects in high density CMOS SRAMs. *IEEE Transactions on Nuclear Science*, 33:1632–1636, 1986.

[68] Karl A. Stetson. The discovery of holographic interferometry, its development and applications. *Light: Advanced Manufacturing*, 3:1–9, 2022.

[69] G.K. Ackermann and J. Eichler. *Holography: A Practical Approach*. Physics textbook. Wiley, 2008.

[70] J. Fujimoto and W. Drexler. *Introduction to Optical Coherence Tomography*, pages 1–45. Springer Berlin Heidelberg, Berlin, Heidelberg, 2008.

[71] Ceyhun Akcay, Pascale Parrein, and Jannick P. Rolland. Estimation of longitudinal resolution in optical coherence imaging. *Appl. Opt.*, 41:5256–5262, 2002.

[72] Enrico Hilpert, Johannes Hartung, Henrik von Lukowicz, Tobias Herffurth, and Nils Heidler. Design, additive manufacturing, processing, and characterization of metal mirror made of aluminum silicon alloy for space applications. *Optical Engineering*, 58: 092613, 2019.

[73] Haig A. Atikian, Neil Sinclair, Pawel Latawiec, Xiao Xiong, Srujan Meesala, Scarlett Gauthier, Daniel Wintz, Joseph Randi, David Bernot, Sage DeFrances, Jeffrey Thomas, Michael Roman, Sean Durrant, Federico Capasso, and Marko Lončar. Diamond mirrors for high-power continuous-wave lasers. *Nature Communications*, 13: 2610, 2022.

[74] Luca Palmieri and Reinhard Koch. Optimizing the lens selection process for multi-focus plenoptic cameras and numerical evaluation. In *Proceedings of the IEEE Conference on Computer Vision and Pattern Recognition (CVPR) Workshops*, 2017.

[75] Joseph A. Ruff and A. E. Siegman. Measurement of beam quality degradation due to spherical aberration in a simple lens. *Optical and Quantum Electronics*, 26:629–632, 1994.

[76] Joe Geary and Phillip Peterson. Spherical Aberration And Diffraction Derived Via Fourier Optics. *Optical Engineering*, 23:230152, 1984.

[77] Stuart A Taylor et al. Ccd and cmos imaging array technologies: technology review. *UK: Xerox Research Centre Europe*, pages 1–14, 1998.

[78] James Janesick and Gloria Putnam. Developments and applications of high-performance ccd and cmos imaging arrays. *Annual Review of Nuclear and Particle Science*, 53:263–300, 2003.

[79] H.P Garnir and P.H Lefèbvre. Quantum efficiency of back-illuminated ccd detectors in the vuv region (30–200nm). *Nuclear Instruments and Methods in Physics Research Section B: Beam Interactions with Materials and Atoms*, 235:530–534, 2005. The Physics of Highly Charged Ions.

[80] FLIR BFS-U3-32S4-BD. Blackfly S BFS-U3-32S4C-BD spectral response curve, 2015.

[81] E.R. Fossum. Cmos image sensors: electronic camera-on-a-chip. *IEEE Transactions on Electron Devices*, 44(10):1689–1698, 1997.

[82] Sanket Mehta, Arpita Patel, and Jagrat Mehta. Ccd or cmos image sensor for photography. In *2015 International Conference on Communications and Signal Processing (ICCSP)*, pages 0291–0294, 2015.

[83] Ramesh Giri and Matthew J. Berg. Backscatter multiple wavelength digital holography for color micro-particle imaging. *Appl. Opt.*, 61:B83–B95, 2022.

[84] Azeem Ahmad, Anand Kumar, Vishesh Dubey, Ankit Butola, Balpreet Singh Ahluwalia, and Dalip Singh Mehta. Characterization of color cross-talk of ccd detectors and its influence in multispectral quantitative phase imaging. *Opt. Express*, 27: 4572–4589, 2019.

[85] Xingbo Dong, Wanyan Xu, Zhihui Miao, Lan Ma, Chao Zhang, Jiewen Yang, Zhe Jin, Andrew Beng Jin Teoh, and Jiajun Shen. Abandoning the bayer-filter to see in the dark. In *Proceedings of the IEEE/CVF Conference on Computer Vision and Pattern Recognition (CVPR)*, pages 17431–17440, 2022.

[86] Russell J. Palum. Image sampling with the bayer color filter array. In *PICS*, 2001.

[87] Mark Richard Shortis, James W. Seager, Euan S. Harvey, and Stuart Robson. Influence of Bayer filters on the quality of photogrammetric measurement. In J.-Angelo Beraldin, Sabry F. El-Hakim, Armin Gruen, and James S. Walton, editors, *Videometrics VIII*, volume 5665, page 56650H. International Society for Optics and Photonics, SPIE, 2005.

[88] John David Jackson. *Classical electrodynamics*. Wiley, New York, NY, 3rd ed. edition, 1999.

[89] Julian Schwinger, Lester L DeRaad Jr, Kimball Milton, and Wu-yang Tsai. *Classical electrodynamics*. Westview Press, 1998.

[90] Walter Greiner. *Classical electrodynamics*. Springer Science & Business Media, 2012.

[91] Michael I Mishchenko, Larry D Travis, and Andrew A Lacis. *Scattering, absorption, and emission of light by small particles*. Cambridge university press, 2002.

[92] Hendrik Christoffel Hulst and Hendrik C van de Hulst. *Light scattering by small particles*. Courier Corporation, 1981.

[93] Winston E. Kock. *Microwave Holography*, pages 179–223. Springer US, Boston, MA, 1975.

[94] Wolfgang K. Fischer and Mauro Zambuto. Optical holographic detection of ultrasonic waves. In A. F. Metherell, editor, *Acoustical Holography*, pages 349–362, Boston, MA, 1971. Springer US.

[95] Rafal E. Dunin-Borkowski, András Kovács, Takeshi Kasama, Martha R. McCartney, and David J. Smith. *Electron Holography*, pages 767–818. Springer International Publishing, Cham, 2019.

[96] Md Sadman Sakib Rahman and Aydogan Ozcan. Computer-free, all-optical reconstruction of holograms using diffractive networks. *ACS Photonics*, 8:3375–3384, 2021.

[97] Ulf Schnars and Werner PO Jüptner. Digital recording and numerical reconstruction of holograms. *Measurement science and technology*, 13:R85, 2002.

[98] Lizhi Chen, Songzhi Tian, Hao Zhang, Liangcai Cao, and Guofan Jin. Phase hologram optimization with bandwidth constraint strategy for speckle-free optical reconstruction. *Opt. Express*, 29:11645–11663, 2021.

[99] R. K. Mueller and N. K. Sheridon. Sound holograms and optical reconstruction. *Applied Physics Letters*, 9:328–329, 1966.

[100] Thomas M. Kreis, Petra Aswendt, and Roland Hoefling. Hologram reconstruction using a digital micromirror device. *Optical Engineering*, 40:926–933, 2001.

[101] C Huygens. Traité de la lumière. leyden. *English version, London*, 1912.

[102] Bevan B Baker and Edward Thomas Copson. *The mathematical theory of Huygens' principle*, volume 329. American Mathematical Soc., 2003.

[103] A. Fresnel and Ann. Chem. *Phys. 1*, 1(239), 1816.

[104] Ulf Schnars and Werner Jüptner. Direct recording of holograms by a ccd target and numerical reconstruction. *Applied optics*, 33:179–181, 1994.

[105] Winston E Kock. *Lasers and Holography: An Introduction to Coherent Optics*. Courier Corporation, 1981.

[106] Soenke Seebacher, Wolfgang Osten, and Werner PO Jueptner. Measuring shape and deformation of small objects using digital holography. In *Laser Interferometry IX: Applications*, volume 3479, pages 104–115. SPIE, 1998.

[107] PA Fryer. Vibration analysis by holography. *Reports on Progress in Physics*, 33:489, 1970.

[108] Ting-Chung Poon. Recent progress in optical scanning holography. *Journal of Holography and Speckle*, 1:6–25, 2004.

[109] Partha P Banerjee. A simple derivation of the fresnel diffraction formula. *Proceedings of the IEEE*, 73:1859–1860, 1985.

[110] E. Sauvageat, Y. Zeder, K. Auderset, B. Calpini, B. Clot, B. Crouzy, T. Konzelmann, G. Lieberherr, F. Tummon, and K. Vasilatou. Real-time pollen monitoring using digital holography. *Atmospheric Measurement Techniques*, 13:1539–1550, 2020.

[111] Osku Kemppinen, Jesse C Laning, Ryan D Mersmann, Gorden Videen, and Matthew J Berg. Imaging atmospheric aerosol particles from a UAV with digital holography. *Scientific Reports*, 10:16085, 2020.

[112] Yi Luo, Yichen Wu, Liqiao Li, Yuening Guo, Ege Çetintaş, Yifang Zhu, and Aydogan Ozcan. Dynamic imaging and characterization of volatile aerosols using deep learning-based holographic microscopy. In *Frontiers in Optics + Laser Science 2021*, page FM2D.4. Optica Publishing Group, 2021.

[113] Joe L. Mauderly and Judith C. Chow. Health effects of organic aerosols. *Inhalation Toxicology*, 20:257–288, 2008.

[114] Ulrich Pöschl. Atmospheric aerosols: Composition, transformation, climate and health effects. *Angewandte Chemie International Edition*, 44:7520–7540, 2005.

[115] Ronald E. Wyzga and Lawrence J. Folinsbee. Health effects of acid aerosols. *Water, Air, and Soil Pollution*, 85:177–188, 1995.

[116] William P. Linak, Jong-Ik Yoo, Shirley J. Wasson, Weiyan Zhu, Jost O.L. Wendt, Frank E. Huggins, Yuanzhi Chen, Naresh Shah, Gerald P. Huffman, and M. Ian Gilmour. Ultrafine ash aerosols from coal combustion: Characterization and health effects. *Proceedings of the Combustion Institute*, 31:1929–1937, 2007.

[117] L. Williams, P. P. Banerjee, G. Nehmetallah, and S. Praharaj. Holographic volume displacement calculations via multiwavelength digital holography. *Appl. Opt.*, 53:1597–1603, 2014.

[118] J. Gass, A. Dakoff, and M. K. Kim. Phase imaging without 2π ambiguity by multiwavelength digital holography. *Opt. Lett.*, 28:1141–1143, 2003.

[119] Annelie Schiller, Tobias Beckmann, Markus Fratz, Alexander Bertz, Daniel Carl, and Karsten Buse. Multiwavelength digital holography: height measurements on linearly moving and rotating objects. In Malgorzata KujawiĹ„ska and Leszek R. Jaroszewicz,

editors, *Speckle 2018: VII International Conference on Speckle Metrology*, volume 10834, pages 626–632. International Society for Optics and Photonics, SPIE, 2018.

[120] Christopher M. Sorensen, Richard C. Flagan, Urs Baltensperger, and David Y. H. Pui. Grand challenges for aerosol science and technology. *Aerosol Sci. Technol.*, 53, 2019.

[121] Dong Zhiwen and Li Zhongqin. Characteristics of atmospheric dust deposition in snow on glacier no. 72, mount tuomuer, china. *Arctic, Antarctic, and Alpine Research*, 43: 517–526, 2011.

[122] H. Maring, D. L. Savoie, M. A. Izaguirre, L. Custals, and J. S. Reid. Mineral dust aerosol size distribution change during atmospheric transport. *Journal of Geophysical Research: Atmospheres*, 108, 2003.

[123] Pramod Kulkarni, Paul A. Baron, and Klaus Willeke. *Aerosol Measurement: Principles, Techniques, and Applications*. John Wiley & Sons, Inc., 2011.

[124] Matthew Berg and Gorden Videen. Digital holographic imaging of aerosol particles in flight. *Journal of Quantitative Spectroscopy & Radiative Transfer - J QUANT SPECTROSC RADIAT*, 112:1776–1783, 07 2011.

[125] Ramesh Giri, Claudia Morello, Yuli W. Heinson, Osku Kemppinen, Gorden Videen, and Matthew J. Berg. Generation of aerosol-particle light-scattering patterns from digital holograms. *Opt. Lett.*, 44:819–822, 2019.

[126] Matthew J. Berg, Yuli W. Heinson, Osku Kemppinen, and Stephen Holler. Solving the inverse problem for coarse-mode aerosol particle morphology with digital holography. *Scientific Reports*, 7:9400, 2017.

[127] S. Santosh Kumar, Cheng Li, Chase E. Christen, Christopher J. Hogan Jr., Steven A. Fredericks, and Jiarong Hong. Automated droplet size distribution measurements using digital inline holography. *J. Aerosol Sci.*, 137, 2019.

[128] Jacob P. Fugal, Raymond A. Shaw, Ewe Wei Saw, and Aleksandr V. Sergeyev. Airborne digital holographic system for cloud particle measurements. *Appl. Opt.*, 43, 2004.

[129] Jorge Garcia-Sucerquia, Wenbo Xu, Stephan K. Jericho, Peter Klages, Manfred H. Jericho, and H. Jürgen Kreuzer. Digital in-line holographic microscopy. *Appl. Opt.*, 45, 2006.

[130] Jorge Garcia-Sucerquia. Multispectral digital lensless holographic microscopy: from femtosecond laser to white light led. In *Imaging and Applied Optics 2014*, page DM3B.2. Optical Society of America, 2014.

[131] Jorge Garcia-Sucerquia. Color lensless digital holographic microscopy with micrometer resolution. *Opt. Lett.*, 37, 2012.

[132] Pierre-Alexander Blanche. *Optical Holography: Materials, Theory and Applications*. Elsevier, 2020.

[133] Yasunori Ito, Yuki Shimozato, Peng Xia, Tatsuki Tahara, Takashi Kakue, Yasuhiro Awatsuji, Kenzo Nishio, Shogo Ura, Toshihiro Kubota, and Osamu Matoba. Four-wavelength color digital holography. *J. Display Technol.*, 8:570–576, 2012.

[134] Zoltán Göröcs, László Orzó, Márton Kiss, Veronika Tóth, and Szabolcs Tőkés. In-line color digital holographic microscope for water quality measurements. In *Laser Applications in Life Sciences*, volume 7376, pages 310–319. SPIE, 2010.

[135] Zoltán Göröcs, Márton Kiss, Veronika Tóth, László Orzó, and Szabolcs Tokés. Multicolor digital holographic microscope (DHM) for biological purposes. In *Imaging, Manipulation, and Analysis of Biomolecules, Cells, and Tissues VIII*, volume 7568, pages 361–370. SPIE, 2010.

[136] Xiaoli Mo, Björn Kemper, Patrik Langehanenberg, Angelika Vollmer, Jinghui Xie, and Gert von Bally. Application of color digital holographic microscopy for analysis of stained tissue sections. In *Advanced Microscopy Techniques*, pages 7367–18. Optical Society of America, 2009.

[137] Nava R Subedi, Matthew J Berg, and Gorden Videen. Simultaneous forward and backward digital holography of microparticles. *Journal of Optics*, 19:115601, 2017.

[138] Nava R. Subedi, Nicholas B. Fowler, and Matthew J. Berg. Backscatter digital holography of microparticles. *Opt. Express*, 21:12611–12616, 2013.

[139] Matthew J. Berg and Christopher M. Sorensen. A review and reassessment of diffraction, scattering, and shadows in electrodynamics. *J. Quant. Spectrosc. Radiat. Transfer*, 210, 2018.

[140] Takaaki Shiratori, Keisuke Kasai, and Nobukazu Yoshikawa. Color-image reconstruction for two-wavelength digital holography using a generalized phase-shifting approach. *Appl. Opt.*, 56:6554–6563, 2017.

[141] Jorge Garcia-Sucerquia. Color digital lensless holographic microscopy: laser versus led illumination. *Appl. Opt.*, 55:6649–6655, 2016.

[142] Alexander Machikhin, Olga Polschikova, Alina Vlasova, Alexander Lyashenko, Ivan Dmitriev, Vladislav Batshev, Marat Bulatov, and Vitold Pozhar. Rgb laser based on an optical parametric oscillator for single-shot color digital holographic microscopy. *Opt. Lett.*, 44:5025–5028, 2019.

[143] A Lyashenko, O Polshchikova, A. Machikhin, A Vlasova, Vitold Pozhar, and A Kozlov. Three-color digital holographic microscopy based on a mach - zehnder interferometer and a solid-state rgb laser. *Quantum Electronics*, 50:662–666, 2020.

[144] Joseph W. Goodman. *Introduction to Fourier Optics*. Roberts and Company, 2005.

[145] Meriç Özcan and Muharrem Bayraktar. Digital holography image reconstruction methods. In *Practical Holography XXIII: Materials and Applications*, volume 7233, pages 88–97. International Society for Optics and Photonics, SPIE, 2009.

[146] Vittorio Bianco, Pasquale Memmolo, Marco Leo, Silvio Montresor, Cosimo Distante,

Melania Paturzo, Pascal Picart, Bahram Javidi, and Pietro Ferraro. Strategies for reducing speckle noise in digital holography. *Light: Sci. and Applications*, 7, 2018.

[147] T.C. Poon. *Digital Holography and Three-Dimensional Display: Principles and Applications*. Springer US, 2006.

[148] Chenggen Quan, Xin Kang, and Cho-Jui Tay. Speckle noise reduction in digital holography by multiple holograms. *Optical Engineering*, 46:1–6, 2007.

[149] Lu Rong, Wen Xiao, Feng Pan, Shuo Liu, and Rui Li. Speckle noise reduction in digital holography by use of multiple polarization holograms. *Chin. Opt. Lett.*, 8: 653–655, 2010.

[150] Weitao Lin, Li Chen, Yonghao Chen, Wenyang Cai, Yihua Hu, and Kunhua Wen. Single-shot speckle reduction by elimination of redundant speckle patterns in digital holography. *Appl. Opt.*, 59, 2019.

[151] Jonathan Maycock, John B. McDonald, and Bryan M. Hennelly. Speckle reduction of reconstructions of digital holograms using three dimensional filtering. *Opt. Commun.*, 300, 2013.

[152] M. Haouat, J. Garcia-Sucerquia, A. Kellou, and P. Picart. Reduction of speckle noise in holographic images using spatial jittering in numerical reconstructions. *Opt. Lett.*, 42, 2017.

[153] V. Bianco, M. Paturzo, P. Memmolo, A. Finizio, P. Ferraro, and B. Javidi. Random resampling masks: a non-bayesian one-shot strategy for noise reduction in digital holography. *Opt. Lett.*, 38, 2013.

[154] Jung Young Son, Valentin G. Dmitriev, Viktor Nikolaevic Mikhailov, and Hyung-Wook Jeon. Solid state lasers for color holography. *Proc. SPIE, Practical Holography X*, 2652, 1996.

[155] Mathieu Leclercq and Pascal Picart. Method for chromatic error compensation in digital color holographic imaging. *Opt. Ex.*, 21, 2013.

[156] Matthew J. Berg, Christopher M. Sorensen, and Amit Chakrabarti. Patterns in mie scattering: evolution when normalized by the rayleigh cross section. *Appl. Opt.*, 44, 2005.

[157] Peng Xia, Yuki Shimozato, Yasunori Ito, Tatsuki Tahara, Takashi Kakue, Yasuhiro Awatsuji, Kenzo Nishio, Shogo Ura, Toshihiro Kubota, and Osamu Matoba. Improvement of color reproduction in color digital holography by using spectral estimation technique. *Appl. Opt.*, 50, 2011.

[158] Hideki Funamizu, Yuta Tokuno, and Yoshihisa Aizu. Estimation of spectral transmittance curves from rgb images in color digital holographic microscopy using speckle illuminations. *Opt. Rev.*, 23, 2016.

[159] Asim Kumar Roy Choudhury. *Principles of Colour and Appearance Measurement*. Woodhead Publishing, 2014.

[160] Valentín Viqueira Pérez, Dolores de Fez Saiz, Francisco Martínez-Verdú, A.K.Roy Choudhury, V.C. Gupte, Robert Hirschler, M. Senthilkumar, Francisco Martínez-Verdú, Elisabet Chorro, Esther Perales, Meritxell Vilaseca, Jaume Pujol, M.L. Gulrajani, Jack A. Ladson, Martin Bide, N.S. Gangakhedkar, B. Xu, N.S. Gangakhedkar, D.B. MacDougall, Andrew Joiner, and D.J. Tobin. Contributor contact details. In *Colour Measurement*, Woodhead Publishing Series in Textiles, pages xi–xiii. Woodhead Publishing, 2010.

[161] Riyadh M. Al saleem, Baraa M. Al-Hilali, and Izz K. Abboud. Mathematical representation of color spaces and its role in communication systems. *Journal of Applied Mathematics*, 2020:4640175, 2020.

[162] J. Guild. The colorimetric properties of the spectrum. *Philosophical Transactions of the Royal Society of London*, 230:149–187, 1931.

[163] J Müller, V Kebbel, and W Jüptner. Characterization of spatial particle distributions in a spray-forming process using digital holography. *Measurement Science and Technology*, 15:706–710, 2004.

[164] Siddharth Talapatra, Jiarong Hong, Malcolm McFarland, Aditya R. Nayak, Cao Zhang, Joseph Katz, James Sullivan, Michael Twardowski, Jan Rines, and Percy Donaghay. Characterization of biophysical interactions in the water column using in situ digital holography. *Marine Ecology Progress Series*, 473:29–51, 2013.

[165] Lei Tian, Nick Loomis, José A. Domínguez-Caballero, and George Barbastathis. Quantitative measurement of size and three-dimensional position of fast-moving bubbles in air-water mixture flows using digital holography. *Appl. Opt.*, 49:1549–1554, 2010.

[166] Jeffrey S. Reid, Barbara Brooks, Katie K. Crahan, Dean A. Hegg, Thomas F. Eck, Norm O'Neill, Gerrit de Leeuw, Elizabeth A. Reid, and Kenneth D. Anderson. Reconciliation of coarse mode sea-salt aerosol particle size measurements and parameterizations at a subtropical ocean receptor site. *Journal of Geophysical Research: Atmospheres*, 111, 2006.

[167] W. L. Chameides, H. Yu, S. C. Liu, M. Bergin, X. Zhou, L. Mearns, G. Wang, C. S. Kiang, R. D. Saylor, C. Luo, Y. Huang, A. Steiner, and F. Giorgi. Case study of the effects of atmospheric aerosols and regional haze on agriculture: An opportunity to enhance crop yields in china through emission controls. *Proceedings of the National Academy of Sciences*, 96:13626–13633, 1999.

[168] Miriam A. Freedman, Kelly J. Baustian, Matthew E. Wise, and Margaret A. Tolbert. Characterizing the morphology of organic aerosols at ambient temperature and pressure. *Analytical Chemistry*, 82:7965–7972, 2010.

[169] Shawn Zhang, Paul A. Stroud, Aiden Zhu, Michael J. Johnson, Joshua Lomeo, Christopher L. Burcham, Jeremy Hinds, Kyle Allen-Francis Blakely, and Matthew J. Walworth. Characterizing the impact of spray dried particle morphology on tablet dis-

solution using quantitative x-ray microscopy. *European Journal of Pharmaceutical Sciences*, 165:105921, 2021.

[170] Anthony T Zimmer and Pratim Biswas. Characterization of the aerosols resulting from arc welding processes. *Journal of Aerosol Science*, 32:993–1008, 2001.

[171] A.R. Jones. Light scattering for particle characterization. *Progress in Energy and Combustion Science*, 25:1–53, 1999.

[172] Yuli W. Heinson, Justin B. Maughan, William R. Heinson, Amitabha Chakrabarti, and Christopher M. Sorensen. Light scattering q-space analysis of irregularly shaped particles. *Journal of Geophysical Research: Atmospheres*, 121:682–691, 2016.

[173] Prakash Gautam and Christopher M. Sorensen. A wide range (0.32°–177.6°), multi-angle light scattering setup and concomitant analysis method. *Review of Scientific Instruments*, 92:113105, 2021.

[174] Matthew J. Berg, Yuli W. Heinson, and Osku Kemppinen. Imaging aerosols with digital holography. *Physics Today*, 71:70–71, 2018.

[175] Leonard Polizzotto and Robert A. Peura. A mathematical approach to explain subjective color perception. *Vision Research*, 15:613–616, 1975.

[176] R Beau Lotto and Dale Purves. The empirical basis of color perception. *Consciousness and Cognition*, 11:609–629, 2002.

[177] Gunter Wyszecki and Walter Stanley Stiles. *Color science*, volume 8. Wiley New York, 1982.

[178] Alex R Wade and Alex V Benjamin. How do we see color? *Front. Young Minds*, 1, 2013.

[179] John Hutchings, Ronnier Luo, and Wei Ji. Calibrated colour imaging analysis of food. In *Colour in food*, pages 352–366. Elsevier, 2002.

[180] Sandra Segnini, Petr Dejmek, and Rickard Öste. A low cost video technique for colour measurement of potato chips. *LWT-Food Science and Technology*, 32:216–222, 1999.

[181] IEC. Multimedia systems and equipment-colour measurement and management-part 2-1: Colour management-default rgb colour space-srgb. *CIE: Vienna, Austria*, 1999.

[182] Sabine Süsstrunk, Robert R. Buckley, and Steve Swen. Standard rgb color spaces. In *Color Imaging Conference*, 1999.

[183] Matthew Anderson, Ricardo Motta, Srinivasan Chandrasekar, and Michael Stokes. Proposal for a standard default color space for the internet—srgb. In *Color and imaging conference*, volume 1996, pages 238–245. Society for Imaging Science and Technology, 1996.

[184] R. Ramanath, W.E. Snyder, Y. Yoo, and M.S. Drew. Color image processing pipeline. *IEEE Signal Processing Magazine*, 22:34–43, 2005.

[185] Christopher M Sorensen, Yuli W Heinson, William R Heinson, Justin B Maughan, and Amit Chakrabarti. Q-space analysis of the light scattering phase function of particles with any shape. *Atmosphere*, 8:68, 2017.

Appendix A

Image Reconstruction Algorithm : Mathematica

The holograms acquired from the color sensor are reconstructed using the Mathematica code below. The hologram and reference image files are first loaded from the computer directory. Then, after separating the RGB color images into red, green, and blue channels, they are transformed into grayscale images. After that, the individual channels are cropped to make them square in size. Finally, a contrast hologram is generated by subtracting the reference from the hologram. Furthermore, the contrast hologram is reconstructed for each wavelength using the Fresnel diffraction integral according to equation 2.35. Finally, a basic Speckle Reduction technique (Gaussian filtering) is used on the three monochromatic images. We now have three monochromes combined using the additive approach, with the monochromes being red, green, and blue.

```
(*Specify the directory and import holograms:*)
ClearAll["Global‘*"]
SetDirectory[NotebookDirectory[]]
refDat = Image[Import["ref.bmp"]];
rawDat = Image[Import["raw.bmp"]];

(* Set global parameters*)
round = 0.001; (*pixel byte depth *)
pix = 3.45; (*sensor pixel size in um*)
lamR = 0.656; (* wavelength of the red laser in um*)
lamG = 0.527; (* wavelength of the green laser in um*)
lamB = 0.440;  (* wavelength of the blue laser in um*)
kred = (2*[pi])/lamR;
kgreen = (2*[pi])/lamG;
kblue = (2*[pi])/lamB;
fontSize = 18;
imageSize = 800;
fontColor = Black;
fontFamily = "Arial";
rotateX[x_] := y
rotateY[y_] := x
abs[array_] := Abs[array];

(*Image Crop*)
crop[img_] := ImageCrop[img, {size, size}]


(* Condition Data *)
size = ImageDimensions[refDat][[2]];
halfSize = Floor[size/2.0];
refList = ColorSeparate[refDat];
rawList = ColorSeparate[rawDat];
refRed = ImageData[crop[refList[[1]]]];
refGreen = ImageData[crop[refList[[2]]]];
```

```
refBlue = ImageData[crop[refList[[3]]]];
rawRed = ImageData[crop[rawList[[1]]]];
rawGreen = ImageData[crop[rawList[[2]]]];
rawBlue = ImageData[crop[rawList[[3]]]];

(* Contrast Holograms *)
conRed = (refRed - rawRed)/refRed;
conGreen = (refGreen - rawGreen)/refGreen;
conBlue = (refBlue - rawBlue)/refBlue;

(*Fast Fresnel Transform*)
 alpha = I*\[Pi]*pix^2;
fresnel[z_,lamda_,hologram_]:=
Exp[2*\[Pie]*I*z/l]/(I*\l*z)*pix^2*
Take[
RotateRight[
InverseFourier[
Fourier[ArrayPad[hologram,halfSize],FourierParameters->{1,1}]*Fourier[Outer[
   Times,Exp[alpha/(lamda*z)*(Range[1,2*size]-size)^2],Exp[alpha/(lamda*z)*(
   Range[1,2*size]-size)^2]],FourierParameters->{1,1}],
FourierParameters->{1,1}],
{size,size}],
{halfSize,halfSize+size-1},{halfSize,halfSize+size-1}]

(*Simple Speckle Reduction & White Balance*)
Eta_r = (dRed*  lr  )/(size*pix);
Eta_g = (dGreen*   lg   )/(size*pix);
Eta_b = (dBlue*   lb  )/(size*pix);
Zeta_r =   lr  *(dRed/(size*pix))^2;
Zeta_g =   lg   *(dGreen/(size*pix))^2;
Zeta_b =   lb  *(dBlue/(size*pix))^2;
speckMultiplier = 0.75;
arrayRed = Abs[fresnel[dRed,lamR,conRed]];
```

```
arrayGreen = Abs[fresnel[dGreen,lamG,conGreen]];
arrayBlue = Abs[fresnel[dBlue,lamB,conBlue]];
filteredArrayRed = GaussianFilter[arrayRed, speckMultiplier* Eta_r ];
filteredArrayGreen = GaussianFilter[arrayGreen, speckMultiplier* Eta_g ];
filteredArrayBlue = GaussianFilter[arrayBlue, speckMultiplier* Eta_b ;

(*White Balance *)
maxRedFilter = Max[filteredArrayRed];
maxGreenFilter = Max[filteredArrayGreen];
maxBlueFilter = Max[filteredArrayBlue];
WB ={ maxRedFilter, maxGreenFilter, maxBlueFilter}
layerRed = Image[ArrayPlot[filteredArrayRed/WB[[1]],
    PlotRange -> plotRangeZoom,
    PlotRangePadding -> 0,
    ImageSize -> Medium,
    Frame -> False,
    FrameTicks -> None,
    ColorFunction -> ({Opacity[1], RGBColor[#, 0 , 0]} &),
    DataReversed -> False,
    ColorFunctionScaling -> False]];

plotRed = Image[ArrayPlot[filteredArrayRed/WB[[1]],
    PlotRange -> plotRangeZoom,
    PlotRangePadding -> 0,
    ImageSize -> Medium,
    Frame -> False,
    FrameTicks -> None,
    ColorFunction -> ({Opacity[1], RGBColor[#, 0 , 0]} &),
    DataReversed -> False,
    ColorFunctionScaling -> False,
    Epilog -> {White, Thickness[0.02], Line[{{70, 15}, {84.5, 15}}]}]];
layerGreen = Image[ArrayPlot[filteredArrayGreen/WB[[2]],
    PlotRange -> plotRangeZoom,
```

```
    PlotRangePadding -> 0,
    ImageSize -> Medium,
    Frame -> False,
    FrameTicks -> None,
    ColorFunction -> ({Opacity[1], RGBColor[0, #, 0]} &),
    DataReversed -> False,
    ColorFunctionScaling -> False]];
plotGreen = Image[ArrayPlot[filteredArrayGreen/WB[[2]],
    PlotRange -> plotRangeZoom,
    PlotRangePadding -> 0,
    ImageSize -> Medium,
    Frame -> False,
    FrameTicks -> None,
    ColorFunction -> ({Opacity[1], RGBColor[0, # , 0]} &),
    DataReversed -> False,
    ColorFunctionScaling -> False,
    Epilog -> {White, Thickness[0.02], Line[{{70, 15}, {84.5, 15}}]}]];
layerBlue = Image[ArrayPlot[filteredArrayBlue/WB[[3]],
    PlotRange -> plotRangeZoom,
    PlotRangePadding -> 0,
    ImageSize -> Medium,
    Frame -> False,
    FrameTicks -> None,
    ColorFunction -> ({Opacity[1], RGBColor[0, 0, #]} &),
    DataReversed -> False,
    ColorFunctionScaling -> False]];
plotBlue = Image[ArrayPlot[filteredArrayBlue/WB[[3]],
    PlotRange -> plotRangeZoom,
    PlotRangePadding -> 0,
    ImageSize -> Medium,
    Frame -> False,
    FrameTicks -> None,
    ColorFunction -> ({Opacity[1], RGBColor[0, 0, #]} &),
```

```
    DataReversed -> False,
    ColorFunctionScaling -> False,
    Epilog -> {White, Thickness[0.02], Line[{{70, 15}, {84.5, 15}}]}]];
deSpeckleImage = ImageAdd[layerRed, layerGreen, layerBlue]
plotImage = ImageAdd[plotRed, plotGreen, plotBlue]
p1 = RemoveAlphaChannel[deSpeckleImage];
trimmedImage = RemoveBackground[p1]

(* Chromaticity of the DH image*)
(*First, look at the distribution of RGB values to determine where the noise
   floor is. Estimate this from the peak of the grayscale distribution.*)
ImageHistogram[trimmedImage, PlotRange -> Automatic]
threshold = 0.25; (*level to define the noise floor*)
removeNoise[chanel_] := If[Norm[chanel] < threshold, Null, chanel]
deNoisedWBimageChanels =
  Map[RGBColor,
  DeleteCases[
  Map[removeNoise, Flatten[ImageData[RemoveAlphaChannel[trimmedImage]], 1]],
  Null]];
chromePlot =
  ChromaticityPlot[{deNoisedWBimageChanels, "RGB"},
  PlotStyle -> {Black, PointSize[pointSize]},
  MaxPlotPoints ->(*50000*)Infinity,
  Frame -> {{True, False}, {True, False}},
  BoundaryStyle ->
  Directive[Dashing[{0.015, 0.015}], Thickness[frameThickness],
  Darker[Gray], Opacity[0.5]],
  FrameLabel -> {"\!\(\*SubscriptBox[\(x\), \(c\)]\)",
  "\!\(\*SubscriptBox[\(y\), \(c\)]\)"},
  FrameStyle ->
  Directive[Thickness[0.66*frameThickness], {Darker[Gray]}],
  BaseStyle ->
  Directive[Darker[Gray], FontFamily -> "Arial",
```

```
  FontSize -> fontSize],
  RotateLabel -> False,
  FrameTicks -> {{{{0, " "}, {0.2, "0.2"}, {0.4, "0.4"}, {0.6,
   "0.6"}, {0.8, "0.8"}},
  None}, {{{0, "0.0"}, {0.2, "0.2"}, {0.4, "0.4"}, {0.6,
   "0.6"}, {0.8, "0.8"}}, None}},
  PlotRangePadding -> 0,
  ImageSize -> 700, Epilog -> {
  {Inset[Threshold[ImageCrop[trimmedImage], 0.], {0.55, 0.75},
  Automatic, 0.07]}}]

(*Export*)
Export["trimmedImage.tif", trimmedImage, ImageSize -> 1500]
Export["plotImage.tif", plotImage, ImageSize -> 1500]
Export["chroma.tif", chromePlot, ImageSize -> 1500]
Export["whiteBalance.m", WB]
```